University of Antwerp
Faculty of Science

Phase Transitions & Soliton Formation in a Dissipative Atomic Josephson Array

Proefschrift voorgelegd tot het behalen van de graad van *Doctor in de Wetenschappen* aan de Universiteit Antwerpen te verdedigen door

Robbe Ceulemans

Supervisors:
Prof. Dr. Michiel Wouters
Prof. Dr. Jacques Tempere

Antwerpen, 2025

Members of the jury

Chair:

Prof. Dr. Sofie Cambré	–	Universiteit Antwerpen

Supervisors:

Prof. Dr. Michiel Wouters	–	Universiteit Antwerpen
Prof. Dr. Jacques Tempere	–	Universiteit Antwerpen

Members:

Prof. Dr. Herwig Ott	–	Technische Universität Kaiserslautern
Prof. Dr. Nikolaos Proukakis	–	Newcastle University
Prof. Dr. Paul Scheunders	–	Universiteit Antwerpen

Public defence:

09/05/2025

The research reported in this thesis was performed at the research group *Theory of Quantum systems and Complex systems (TQC)*, affiliated with the Department of Physics at the University of Antwerp. It was supported by the Research Foundation - Flanders (FWO) through the research project: "Bose-Einstein condensation of ultracold atoms out of equilibrium", project number 39532.

The PhD researcher and supervisors declare that the PhD research was conducted according to the principles of scientific integrity, as mentioned in the general PhD regulations and charter for PhD researchers of UAntwerp and the integrity charter for PhD researchers and supervisors affiliated with the University of Antwerp.

Acknowledgments

This thesis marks the end of four years of research and collaboration. While it brings together the results and insights gained along the way, it cannot fully reflect the many great experiences that helped shape it. Above all, what truly made this journey unique were the people I met and worked with—and it is my pleasure to thank them here.

First and foremost, I would like to thank my supervisor Michiel for his valuable insights and unwavering mentorship throughout these four years. Without him, I would not have had the opportunity to start this project, let alone finish it successfully. The results presented here are as much his achievement as they are mine. I am grateful for the many insightful discussions on research topics as well as the countless coffee breaks, lunches and table tennis matches that helped us clear our minds. I deeply appreciate Michiel's way of doing research and I can only hope to have internalized some of his wisdoms along the way. I also need to thank Jacques, co-supervisor of this thesis and head of the research group. The many courses he teaches with extreme passion made a lasting impression on me. His guidance during my master thesis is what convinced me to pursue a position as PhD student in his group, a choice that has defined these last four years.

This brings me to the wonderful group of colleagues at TQC, who each left their mark on my development as a researcher: Timour, Matthew, Lennart, Filippo, Wouter, Ingvar, Lucas, Jago, Laura, Laurent, Denise, Michiel (junior), Sergei, Ellie, Manon and Jeroen. A heartfelt thank you to all of them for the stimulating conversations, shared challenges and good humour along the way. Working alongside such talented and supportive individuals made this experience all the more rewarding. Among them, a special thank you goes to Timour and Matthew for their help and guidance when I first joined the group. The same goes for Lennart, who was always eager to discuss shared interests or to join me in a quest for good coffee.

This research took me to many wonderful places, with the absolute highlight being my research stay in Brisbane. I am especially grateful to Matthew Davis for welcoming me into his group. It was a truly unique experience not only due to the exciting research in a magnificent setting, but also because of the incredible people I met there. I owe thanks to my colleagues from down under, Guillaume, Maarten, Andrew, Matthew and Ray, for the warm camaraderie during and after working hours. A special thank you also to Samuel for the inspiring teamwork and many intense writing sessions, from which I learned a great deal. But most importantly I want to thank my housemates, Lewis and Harry, for making me feel at home far away from my own. Thanks for all the beautiful yet challenging hikes, the fun climbing sessions and the many shared dinners. A special thanks also to Caroline, David, and Alexandre. They were the first to welcome me and truly helped me find my way.

Equally important are my family, who have been rooting for me since long before I started my PhD. Words fall short when it comes to thanking my parents for their never-ending encouragement and support in everything that I undertake, my sisters for a listening ear, a kind word or a necessary distraction all in due time, and my grandparents for their gentle presence growing up. Of course, I cannot forget my friends who always kept me grounded and reminded me that life exists outside of research. Among them, I am especially grateful to Maxim, whose positivity and joy have enriched my life for almost fifteen years now.

Naturally, this journey came with its moments of struggle and doubt−moments that would have been far more difficult to face without the love and support of my girlfriend, Eveline. Thank you for your patience and understanding in this process, but most importantly, thank you for the many moments of fun, laughter and adventure.

Finally, I would like to thank all the members of the jury for taking the time to read and meticulously evaluate this thesis.

Robbe Ceulemans
April 2025

Nederlandstalige samenvatting

De fundamentele natuurwetten bieden een elegante en nauwkeurige beschrijving van de beweging van individuele deeltjes en hun onderlinge interacties. Tweedeeltjesproblemen kunnen hiermee exact worden opgelost, wat diepgaand inzicht oplevert in de structuur van het universum op zowel microscopische als macroscopische schaal, gaande van de beweging van een enkel elektron in een waterstofatoom tot de banen van planeten rond hun ster. De complexiteit neemt echter snel toe naarmate het aantal interagerende deeltjes groter wordt. Zelfs het beschrijven van een bescheiden veeldeeltjessysteem vereist het oplossen van een stelsel vergelijkingen met een onoverkomelijk aantal vrijheidsgraden. Om het collectieve gedrag van zulke systemen te kunnen begrijpen, ontwikkelden pioniers als Boltzmann, Maxwell en Gibbs in de tweede helft van de 19e eeuw het kader voor de statistische mechanica. Hun werk maakte het mogelijk om de sprong te maken van wetmatigheden op microscopisch niveau naar macroscopische eigenschappen zoals temperatuur, druk en entropie.

Hoewel de klassieke statistische mechanica bijzonder succesvol was in het beschrijven van gassen, warmtemachines en faseovergangen, faalde ze bij bepaalde experimentele waarnemingen aan het begin van de 20e eeuw. Een opvallend voorbeeld was de zogenoemde ultravioletcatastrofe: de voorspelling door de klassieke theorie dat een zwarte straler bij thermisch evenwicht een oneindige hoeveelheid energie zou uitstralen bij hoge frequenties. Deze paradox werd opgelost door Max Plancks veronderstelling dat licht bestaat uit kleine, gediscretiseerde pakketjes energie, of *fotonen*, en vormde het begin van een fundamenteel nieuwe theorie: de kwantummechanica. Belangrijk in de ontwikkeling van deze theorie waren de waarnemingen van de golf-deeltje-dualiteit, waarbij uiterst kleine objecten zowel golf- als deeltjesgedrag kunnen vertonen. De kwantummechanica verving het klassieke deeltjesbeeld door golffuncties en introduceerde een probabilistische interpretatie

van fysische grootheden. Samen met het concept van ononderscheidbare deeltjes maakte dit een radicaal nieuw denkbeeld van collectief gedrag mogelijk. Zo werd de kwantumstatistische mechanica de natuurlijke opvolger van de klassieke versie, en ontsloot ze de wereld van de kwantum-veeldeeltjesfysica.

In de afgelopen decennia hebben technologische ontwikkelingen het mogelijk gemaakt om een breed scala aan interessante kwantumsystemen te creëren en te beheersen, wat heeft geleid tot de observatie van opmerkelijke fenomenen zoals superfluïditeit en superconductiviteit. In dit proefschrift richten we ons op een bijzonder rijk platform, dat van ultrakoude atomaire gassen. Een ijl atoomgas ondergaat een faseovergang naar een *Bose-Einstein condensaat* wanneer het onder een kritische temperatuur wordt gekoeld. Deze unieke fase van materie ontstaat uit een coherente wisselwerking tussen een macroscopisch aantal deeltjes en vertoont kwantumeffecten−die normaal gesproken beperkt blijven tot het niveau van individuele atomen−over de gehele wolk. De eerste realisatie van een Bose-Einstein condensaat in 1995 betekende een belangrijke mijlpaal, en sindsdien vormen kwantumfluïda een veelzijdig testplatform voor kwantummechanica. In tegenstelling tot andere systemen, zoals kwantumfluïda van licht, zijn configuraties van ultrakoude atomen zeer controleerbaar en uitzonderlijk goed geïsoleerd van hun omgeving.

Systemen die onderhevig zijn aan significante interacties met hun omgeving worden *open kwantumsystemen* genoemd. Traditioneel werden zulke interacties beschouwd als bronnen van decoherentie die leiden tot het verlies van interessante kwantumeffecten en dus als ongewenst gezien. Recente ontwikkelingen hebben echter een genuanceerder beeld geschetst: door interacties met de omgeving op een gecontroleerde manier te ontwerpen, kan dissipatie zelf een krachtig hulpmiddel worden. Zorgvuldig ontworpen verliesmechanismen kunnen niet-evenwichtstoestanden stabiliseren, dissipatieve faseovergangen aandrijven en algemeen leiden tot dynamische fenomenen die ontoegankelijk zijn in gesloten systemen. In dit opzicht bieden ultrakoude atomaire gassen een unieke mogelijkheid om de wisselwerking tussen coherentie, interactie en dissipatie te bestuderen in een gecontroleerde en goed begrepen omgeving.

In dit proefschrift onderzoeken we een specifieke opstelling van een ultrakoud atoomgas: de dissipatieve Josephson keten. Ons doel is om meer inzicht te krijgen in de mechanismen die aan de basis liggen van een reeks interessante experimentele waarnemingen. Hiervoor lossen we verschillende wiskundige modellen op, zowel theoretisch als numeriek, op verschillende niveaus van benadering en complexiteit.

Door de expliciet geïntroduceerde dissipatie, waarbij atomen geïoniseerd worden om ze uit de val te extraheren, is het vertrekpunt voor deze berekeningen steevast de Lindblad mastervergelijking voor open kwantumsystemen.

Eerst introduceren we de Kerr resonator, een paradigmatisch systeem dat gekenmerkt wordt door een dissipatieve eerste-orde-faseovergang. Analytische oplossingen voor het beschrijvende model, dat slechts een complexe variable bevat, zijn beschikbaar in de literatuur, zowel binnen de *mean-field*-benadering als in een exacte kwantumbeschrijving, en bieden kwalitatief inzicht in de waargenomen fenomenen. Vervolgens bespreken we het dissipatieve Bose-Hubbard-model, een benadering van de experimentele opstelling die zich richt op de longitudinale dynamica. Een initiële studie van de niet-evenwichtstoestanden in de mean-field-benadering bevestigt een kwalitatieve gelijkenis met het Kerr-model, maar wijst ook op belangrijke kwantitatieve verschillen. Hieruit blijkt ook al dat een extra regio in het fasediagram relevant kan zijn, namelijk het donkere soliton. Op basis van de mean-field-resultaten stellen we een effectief model voor dat de superfluïde stromen in het rooster beschrijft via een incoherente aandrijving, en dat een accurate weergave biedt van de niet-evenwichtstoestanden. Daarna verkrijgen we een meer geavanceerd beeld via de getrunceerde Wigner-benadering die kwantumfluctuaties tot op zekere hoogte incorporeert. In dit formalisme reconstrueren we de dichtheidsmatrix van het dissipatieve systeem en maken opnieuw de vergelijking met het voorgestelde effectieve model. We stellen vast dat het model met incoherente aandrijving de fluctuaties in het systeem licht onderschat.

Hoewel het Bose-Hubbard-model waardevol inzicht biedt, blijft een kwantitatieve vergelijking met de experimentele resultaten moeilijk. Een meer geavanceerde beschrijving van het experiment, waarin alle relevante vrijheidsgraden worden meegenomen, wordt verkregen aan de hand van het *projected c-field*-formalisme. Dit model gebruiken we om de rol van coherentie in de verlieslocatie van de Josephson keten bij lage dichtheden te onderzoeken, d.w.z. op de onderste tak van de hysteresislus. Het geïdealiseerde geval wordt weergegeven door het multimodale analoge model van de Kerr-resonator: een 2D harmonische val met een perfect coherente aandrijving. Hier identificeren we verschillende eigenschappen die wijzen op niet-evenwichtcondensatie in een geëxciteerde toestand van de val. Een soortgelijk gedrag wordt ook in de Josephson keten waargenomen, waarbij de aandrijving via interne reservoirs als een imperfecte laser kan worden beschouwd. Interessant is dat de specifieke structuur van het systeem haaks op de richting van het optisch rooster een cruciale rol speelt, wat duidelijk wordt bij variatie van de verhouding

tussen de val frequenties.

Tot slot onderzoeken we uitvoerig het deel van het fasediagram dat niet eerder geïdentificeerd werd: het stationaire donkere soliton. We tonen het belang aan van fasefluctuaties in de Josephson keten en hoe dit leidt tot de vorming van een soliton. Met behulp van het uitgebreide 3D-model reconstrueren we het fasediagram en maken we een directe vergelijking met experimentele gegevens, wat sterk wijst op de aanwezigheid van het donkere soliton in experimenten. Berekeningen voor dit complexe 3D-systeem zijn echter zeer veeleisend. Daarom keren we nog terug naar het kwalitatief goede Bose-Hubbard-model. Binnen dit model bestuderen we deze nieuwe vorm van bistabiliteit en de bijbehorende eerste-orde-faseovergang. We sluiten af met een studie van de dynamische instabiliteit van het soliton − een eendimensionale niet-lineaire excitatie − in een hoger-dimensionale omgeving, waarbij we het effect van een optisch rooster op deze instabiliteit bespreken.

Abstract

Over the past decades ultracold atomic gases have emerged as a highly controllable platform for probing quantum many-body phenomena, including Bose-Einstein condensation and superfluidity. These systems are particularly suited to exploring the physics of open quantum systems where interactions with the environment, traditionally considered a source of decoherence, can be engineered to reveal new types of non-equilibrium behaviour. This thesis focuses on the dissipative Josephson array, a setup of ultracold atoms subjected to a controlled loss mechanism.

The primary goal is to better understand a series of intriguing experimental observations by analysing a range of theoretical models. As such, the focus is put on the dissipative Bose-Hubbard model, which isolates the lattice dynamics and provides insight into the system's steady-state properties. Our analysis reveals qualitative similarities to the rather simple picture of a Kerr resonator, but also points to significant differences. To refine our understanding, we develop an effective model for the internal reservoirs based on incoherent driving, which accurately captures the observed non-equilibrium steady states. Additionally, signs of a previously unexplored region in phase space are observed. The work culminates in the identification of this phase: the standing dark soliton. Using a detailed 3D model, we reconstruct the system's full phase diagram and perform a direct comparison with experimental data, demonstrating the relevance of the dark soliton to the observed phenomena.

"The aim of science is to seek the simplest explanations of complex facts. We are apt to fall into the error of thinking that the facts are simple because simplicity is the goal of our quest.
The guiding motto in the life of every natural philosopher should be, 'Seek simplicity and distrust it'."

– Alfred North Whitehead, *The Concept of Nature*

Contents

CHAPTER 1

Overview

This thesis investigates the rich physics of open many-body quantum systems, a class of systems where internal dynamics competes environment-induced effects. Of particular interest is a configuration consisting of a cloud of ultracold atoms loaded into a lattice potential and subject to a highly localised, externally induced loss process. The setup features phenomena typically observed in quantum optical systems, but displays an even richer many-body phase diagram due to its coherent, atomic nature. In this work we study the non-trivial out-of-equilibrium physics that results from a balance between losses, tunnelling and interactions.

Part I sets the stage for the research that follows. First off, in **Chapter 2**, we introduce the concept of Bose-Einstein condensation in ultracold atomic gases. After an overview of some fundamental notions, we discuss a number of ways in which the medium can be manipulated and how this affects the observed properties. **Chapter 3** provides a brief review on how to treat a quantum system coupled to a Markovian environment in terms of the Liouvillian superoperator. After passing over the main steps in the derivation of the Lindblad master equation, we continue to discuss the spectral theory of the Liouvillian. The latter is our key to understanding the emergence of a dissipative first-order phase transition. In **Chapter 4**, we outline different methods that can be leveraged to treat many-body (open) quantum systems approximately. Just like many great textbooks, this begins with an introduction to the renowned Gross-Pitaevskii equation, followed by a discussion of the Bogoliubov formalism. Next, we introduce the notion

of a quantum mechanical phase space and how many-body states can equivalently be represented by quasi-probability functions. Here, emphasis is put on the Wigner representation and the corresponding Wigner function. An approximate method that utilizes a description in phase space is the truncated Wigner approximation. Lastly, the projected c-field formalism is introduced. The underlying reasoning and assumptions are reviewed and we discuss the necessity of this class of methods with regards to our work.

Having discussed the background in the first part, we delve into the primary content on dissipative first-order phase transitions in Part II. As a frame of reference, the paradigmatic example of a driven-dissipative phase transition in a single, optical Kerr resonator is reviewed in **Chapter 5**. Both the mean-field analysis and the exact quantum mechanical solutions are discussed. In **Chapter 6**, a detailed study is performed of the dissipative Bose-Hubbard model. Despite representing an atomic configuration it interestingly displays many of the signature properties of the optical resonator. The equivalent of optical bistability is first examined in the mean-field limit, revealing both similarities and discrepancies. Based on these results, an effective description is proposed and evaluated with the goal of furthering our understanding of the underlying physics. A more complete picture is obtained in the truncated Wigner approximation that incorporates quantum fluctuations up to a certain degree. In this formalism we reconstruct the lossy system's density matrix and again make the comparison to our proposed effective model. Finally, some preliminary results are shown on multistability in the case of a similar configuration for a binary mixture. This mostly highlights the potential for future scientific endeavours, both experimental and theoretical.

Although the Bose-Hubbard model provides valuable insights, quantitative predictions remain out of reach. In **Chapter 7**, the projected c-field formalism is applied to include all degrees of freedom of the experimental configuration. The question posed in this chapter is whether coherence persists in the lossy site of the Josephson array even at low densities, i.e. on the lower branch of the hysteresis loop. The idealised case is again represented by the analogue of the Kerr resonator: a 2D harmonic well with a perfectly coherent drive. Here, we identify a number of properties that indicate non-equilibrium condensation in an excited state of the harmonic trap. A similar trend can be observed in the Josephson array where the driving of the lossy well from internal reservoirs can be deemed an imperfect laser. Interestingly, the precise structure of the system perpendicular to the optical lattice plays a crucial role. This becomes clear by varying the ratio

of trapping frequencies.

In the final chapter of this part, **Chapter 8**, we explore in great detail a region of the system's phase diagram that has not been identified before: the standing dark soliton. We start off with a brief summary of the dark soliton's signature properties, which substantiate the conclusions of the next section. Here, the importance of phase fluctuations is evidenced in simulations that take into account all experimentally relevant degrees of freedom. A central result of this chapter, and of the thesis in general, is the reconstruction of the phase diagram from first principles. It strongly indicates the relevance of the soliton in experiments. Calculations for this intricate three-dimensional system are, however, very demanding. Therefore, we continue with the qualitatively good dissipative Bose-Hubbard model. Here, we take a closer look at this novel type of bistability and the underlying first-order phase transition. This chapter concludes with a study of the dynamical instability of the soliton − a one-dimensional non-linear excitation − in a higher-dimensional setting, discussing the impact of an optical lattice on this instability.

Lastly, in **Chapter 9** in the third part, we conclude this thesis with a summary of the results and a brief overview of possibilities for the continuation of the research.

Part I

Background

CHAPTER 2

Ultracold gases in optical lattices

The concept of Bose-Einstein condensation has turned one hundred years old around the same time as when writing of this thesis was completed. In the year 1924, Indian physicist Satyendra N. Bose put forward a statistical description for identical and indistinguishable particles of light, now known as photons [1]. It built on the notion set forth by Planck that light is only emitted in small discrete packets of energy, called *quanta*. It was however Albert Einstein who in that same year, in the first of three consecutive papers, extended the concept to an ideal gas of massive particles [2]. In the subsequent paper, he showed that as a consequence of the underlying statistics the gas should transition to a novel phase at sufficiently low temperatures [3], a fifth state of matter. This phase appears when a macroscopic fraction of the atoms in the gas *condense* in the lowest energy state, hence the name that was given to it later. Historically, the first observations of macroscopic quantum coherence occurred in liquid ^{4}He and superconducting metals, before the underlying mechanisms were even theorized. For a long time, the superfluid and superconducting properties were understood only at a phenomenological level. The third medium, ultracold dilute atomic vapours, became experimentally within reach many decades later, in 1995.

The uncovering of physics at low temperatures was accompanied by the emergence of quantum mechanics. Bose-Einstein condensates (BECs) no longer behave classically, but provide the opportunity to study quantum mechanics on a macroscopic scale. This chapter introduces the basic features of the quantum theory of bosonic,

ultracold gases, reprising solely those concepts most essential for the understanding of this thesis. There exists however an abundance of excellent textbooks [4–7] and review articles [8–12] available for the interested reader to further delve into.

2.1 From theory to reality: Bose-Einstein condensation

2.1.1 Wave functions

Imagine a small, point-like object with a certain mass m moving for simplicity in one dimension. Given that we know its position x and velocity v at some point in time, we can predict its future path exactly by applying Newton's second law, $F = ma$. For a long time, the particles that build up the world around us were viewed in this classical picture, but in 1924 Louis de Broglie proposed in his doctoral thesis [13] a different view on the matter. Particles − electrons and atoms, but also even molecules − should be regarded as little wave packets of a certain frequency ω and with a wavelength that scales with the temperature T,

$$\lambda_{dB} = \sqrt{\frac{2\pi\hbar^2}{mk_BT}}, \tag{2.1}$$

the thermal de Broglie wavelength, much in analogy with Planck's theory on quanta of light. The main implication here is that particles are spatially extended, i.e. their position is subject to uncertainty. Fundamentally, all matter has both particle and wave properties, the famous particle-wave duality. So what does that mean for our atom moving in one dimension? Can we still predict its future path, given its uncertainty now? Let us consider a dilute gas of atoms at high temperatures, relevant in our day to day lives. Typically, the average distance between particles in a gas of density n is much larger than the uncertainty on their position, $n^{-1/3} \gg \lambda_{dB}$. As a result, classical laws will hold up, allowing us to treat the gas as a group of microscopic marbles bouncing around. An ideal gas of particles at thermal equilibrium follows the Maxwell-Boltzmann distribution. With decreasing temperature, the uncertainty on the position of each particle grows as $T^{-1/2}$ and eventually catches up with the inter-particle distance. When this happens, the classical picture is no longer sufficient and we have to resort to a fundamentally different theory−quantum mechanics. Generally, the threshold where classical becomes quantum is taken at $n\lambda_{dB}^3 \gtrsim 1$, where $n\lambda_{dB}^3$ is called the gas parameter.

In quantum mechanics a particle is described by its *wave function* $\psi(x, t_1)$, a complex mathematical object containing all the properties of the quantum state at a given point in time. What this wave function would then look like in the future can be determined by means of the Schrödinger wave equation [14]

$$i\hbar\frac{\partial\psi}{\partial t} = -\frac{\hbar^2\nabla^2}{2m}\psi + V\psi. \tag{2.2}$$

The question still remains, what exactly is this wave function? The most intuitive explanation is given by Born's rule [15], which comes down to saying that the probability of finding (read measuring) the particle at a specific position x at some time t is given by the amplitude of its wave function at that point in space and time $|\psi(x,t)|^2$.

In our macroscopic world, all objects can be labelled, like for example two identical billiard balls. Despite their similar appearance, they occupy different places in space and one can identify and track their paths individually, they are *distinguishable*. For fundamental particles there is, however, no meaningful way to track or label them, they are truly identical. Quantum mechanics does not allow to distinguish their individual identities. Taking two identical particles with their respective positions labelled by x_1 and x_2, then quantum mechanics imposes indistinguishability through:

$$|\psi(x_1, x_2)|^2 = |\psi(x_2, x_1)|^2. \tag{2.3}$$

The total wave function for a pair of identical particles should remain unchanged up to a global phase factor when the particles are interchanged. At this level, there are only two types of fundamental particles: bosons and fermions. Bosons, which have integer spin, follow symmetric wave functions such that $\psi(x_1, x_2) = \psi(x_2, x_1)$. Fermions, on the other hand, have half-integer spin and follow antisymmetric wave functions, meaning $\psi(x_1, x_2) = -\psi(x_2, x_1)$.

2.1.2 The fifth state of matter

The symmetry requirement for fermions leads to *Pauli's exclusion principle* [16], which states that no two identical fermions can occupy the same quantum state simultaneously. From this follows the Fermi-Dirac distribution for many identical fermions. Bosons, however, do not suffer this restriction. On the contrary, they have a propensity to occupy the same quantum state. Identical bosons are distributed over the single-particle energy levels according to the Bose-Einstein dis-

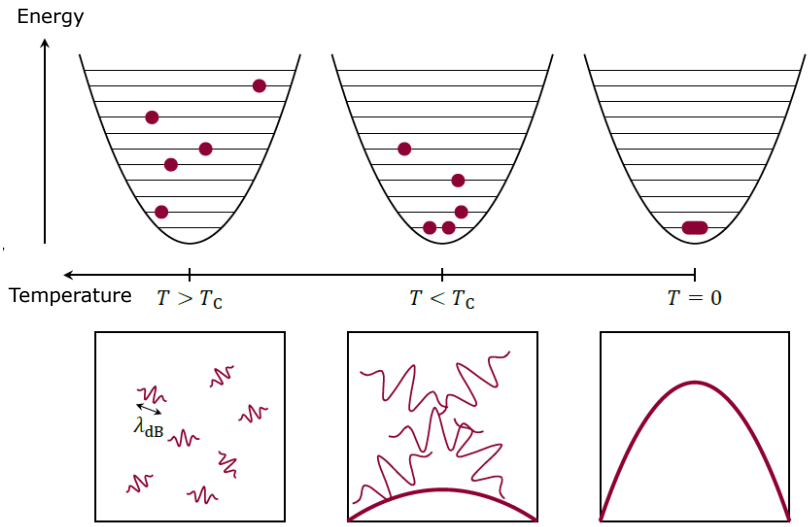

Figure 2.1 – Schematic representation of the condensation process for bosons in a harmonic trap. The top row represents the distribution of particles in the energy landscape above and below the critical temperature, and at exactly $T = 0$. As the temperature decreases, particles occupy lower energy levels. At the same time the occupation of the ground state grows. The same instances are shown on the bottom row in a wave function picture. With dropping temperature, the de Broglie wavelength increases, causing wave functions to overlap. Particles in the same state start to form the condensate. Figure reproduced with permission from Ref.[17].

tribution:

$$\overline{n}_i = \frac{1}{e^{(\epsilon_i - \mu)/k_B T} - 1} \tag{2.4}$$

where $\overline{n}_i$ is the expected occupation of energy level ϵ_i at a temperature T and for a certain chemical potential μ. It follows from this distribution that the upper bounds for the total number of particles in excited states decreases with temperature. As the temperature is lowered, particles therefore pile into the lowest energy state, the only state whose occupation can be arbitrarily large. When cooled enough, a macroscopic number of particles occupies the same ground state and forms the Bose-Einstein condensate. The temperature at which this happens is referred to as the critical temperature T_c.

A schematic map of the road to Bose-Einstein condensation might provide more insight than a list of equations. The panels in Fig. 2.1 indicate, from left to right, the different steps in the cooling down of a dilute gas of bosonic particles. At high temperatures, uncertainty on a particle's location is sufficiently low such

that the classical laws accurately predict the physics at hand. An example is air at room temperature, which has a gas parameter $n\lambda_{dB}^3 \approx 10^{-7}$, well away from the regime where quantum effects play any significant role. The particles are sparsely distributed over the higher energy levels. Cooling down the atomic gas increases the spread of the wave packets, while also increasing the density $n \sim T^{-1}$, bringing us closer to the threshold $n\lambda_{dB}^3 \approx 1$. At this tipping point, individual properties are lost and the only valid description is in terms of quantum mechanical wave functions. The thermal wavelength has grown to the same size as the inter-particle distance, making the particles no longer distinguishable. As more particles are forced to occupy the lowest-energy state, overlap of the wave packets of the same quantum state result in the formation of a single, composite wave function. Roughly speaking, the particles merge to form one macroscopic *super atom*, the condensate. At $T = 0K$, all atoms have gathered in the condensate. The condition represented in this last panel is, however, a theoretical ideal, since absolute zero temperature is physically impossible to reach.

While liquid Helium has been fabricated more than a century ago, with Bose-Einstein condensation underlying its phenomenology of superfluidity, strong interactions cause large differences from the ideal Bose gas and make *ab initio* theory quite hard. It took until 1995 for the first experimental realisations of weakly interacting Bose-Einstein condensates from atomic vapours, due to very low critical temperatures of dilute gases. Concurrently at JILA [18] and at MIT [19], the existence of this new phase was evidenced[1]. For this achievement the lead scientists, Eric Cornell and Carl Wieman, and Wolfgang Ketterle, were awarded the 2001 Nobel prize in physics. Temperatures reached in experiments with ultracold gases are typically of the order of nanoKelvin (10^{-9}K), with a recent record coldest temperature as little as 38pK (10^{-12}K)[20]. Pictures from an early experiment performed at MIT (Ketterle Lab), shown in Fig. 2.2, clearly depict the grouping of atoms in the condensate as the critical temperature is transgressed. Originally, proof was provided through equivalent maps of the velocity distribution of particles [18, 19], demonstrating the accumulation in the zero momentum state.

In addition to all particles occupying the same single-particle state, a condensate features phase coherence. Compare this if you will to a large group of people: a thermal gas is like a crowd at a festival, all excited and moving disorderly and bumping into each other; a BEC would be a group of well-trained soldiers marching

[1] While the group in Colorado utilised a vapour of rubidium-87 atoms, Ketterle's team at MIT condensed a dilute gas of sodium-23 atoms.

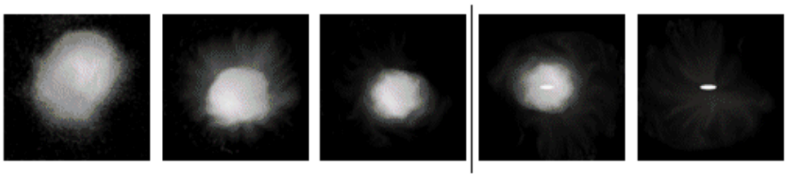

Figure 2.2 – Snapshots of the particle density in real space at different cooling stages of a trapped gas of ^{87}Rb atoms. Panels left of the vertical line, representing the critical temperature T_c, show a thermal gas shrinking as it is cooled down. Below the critical temperature a condensate is formed, seen from the bright speck in the centre of the trap. At first, there is still a significant thermal cloud, but as the temperature lowers further more atoms drop to the condensate. Figure reproduced from Ref. [21].

in a parade, moving in perfect synchronization. The soldiers are said to be moving in phase. Phase coherence of the atoms in a BEC allows the description of the cloud by a single macroscopic wave function:

$$\Psi(\mathbf{r}) = |\Psi(\mathbf{r})|e^{iS(\mathbf{r})}. \tag{2.5}$$

The absolute value of this complex, classical field determines the density of particles, $n(\mathbf{r}) = |\Psi(\mathbf{r})|^2$, while the phase $S(\mathbf{r})$ establishes properties like superfluidity. A consequence of the phase uniformity and a testament to the quantum-mechanical nature of the condensate is the observation of interference patterns. When mixing two separate BECs their amplitudes will interfere, creating the typical patterns in the density as shown in Fig. 2.3.

2.1.3 Microscopic theory

Of fundamental importance in the theory of quantum mechanics is the Hamiltonian, the operator that represents the system's energy. When treating many-body systems, the Hamiltonian is generally expressed in second quantization. This framework treats the single-particle wave functions themselves as operators. In terms of the bosonic field operators $\hat{\Psi}^\dagger(\mathbf{r})$ and $\hat{\Psi}(\mathbf{r})$, the Hamiltonian for a Bose gas is given by

$$\begin{aligned}\hat{H} = &\int \mathrm{d}\mathbf{r}\ \hat{\Psi}^\dagger(\mathbf{r}) \left[-\frac{\hbar^2\nabla^2}{2m} + V(\mathbf{r})\right] \hat{\Psi}(\mathbf{r}) \\ &+ \frac{1}{2}\int \mathrm{d}\mathbf{r} \int \mathrm{d}\mathbf{r}'\ \hat{\Psi}^\dagger(\mathbf{r})\hat{\Psi}^\dagger(\mathbf{r}')U(\mathbf{r}-\mathbf{r}')\hat{\Psi}(\mathbf{r}')\hat{\Psi}(\mathbf{r}).\end{aligned} \tag{2.6}$$

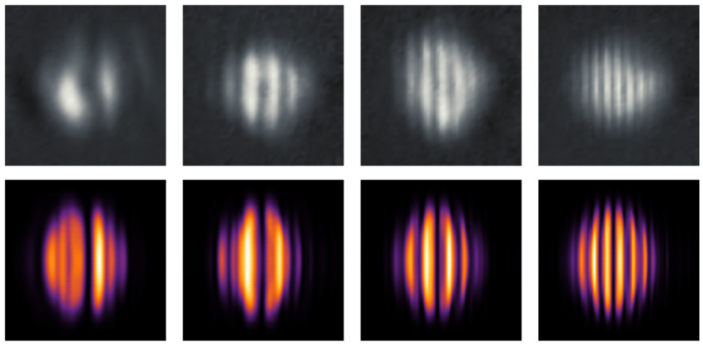

Figure 2.3 – Two atomic condensates, created spatially separated and with opposing momenta, overlap and generate interference patterns, a purely quantum-mechanical effect. The top row shows experimental measurements, while the bottom row presents numerical results. Figure reproduced from Ref. [22].

Different from the classical fields is that these field operators satisfy the commutation relations

$$\left[\hat{\Psi}(\mathbf{r}), \hat{\Psi}(\mathbf{r}')\right] = 0, \qquad \left[\hat{\Psi}(\mathbf{r}), \hat{\Psi}^\dagger(\mathbf{r}')\right] = \delta(\mathbf{r} - \mathbf{r}'). \tag{2.7}$$

In the expression for the Hamiltonian, $V(\mathbf{r})$ denotes the external trap holding the gas in place. The two-body potential $U(\mathbf{r}-\mathbf{r}')$ represents the interaction potential, depending on the separation between two interacting atoms. Because interatomic interactions are large at the scale of the kinetic energy of the atoms at ultracold temperatures, this hamiltonian is hard to deal with in mean-field or perturbation theory. Fortunately, at low temperatures where the relevant length scales are much larger than the range of the potential, it is only the scattering length that characterises the atomic interaction properties. The true potential can therefore be replaced by the effective contact interaction

$$U_{\text{eff}}(\mathbf{r} - \mathbf{r}') = g\delta(\mathbf{r} - \mathbf{r}'), \tag{2.8}$$

where $g = 4\pi\hbar^2 a_{\text{scatt}}/m$ and a_{scatt} is the s-wave scattering length. In order to describe the properties of the macroscopic wave function, the actual shape of the potential is unimportant. This effective potential allows for a mean-field and perturbative description in the weakly interacting regime $na_{\text{scatt}}^3 \ll 1$. As a consequence of neglecting short-range physics by taking this effective potential, one cannot evaluate the condensate wave function on a scale smaller than the scatter-

ing length. Substituting (2.8) in the Hamiltonian results in

$$\hat{H} = \int \mathrm{d}\mathbf{r}\ \hat{\Psi}^\dagger(\mathbf{r}) \left[-\frac{\hbar^2\nabla^2}{2m} + V(\mathbf{r}) + \frac{g}{2}\hat{\Psi}^\dagger(\mathbf{r})\hat{\Psi}(\mathbf{r}) \right] \hat{\Psi}(\mathbf{r}), \tag{2.9}$$

the starting point of all calculations in this work. A system's Hamiltonian not only describes its equilibrium properties, but also drives the dynamics. The latter can be tracked through the change of the field operators, given by the *Heisenberg equation*, $i\hbar\partial_t\hat{\Psi} = [\hat{\Psi}, \hat{H}]$. Making use of the commutation relations above, this leads to an equation of motion (EOM) for the field operators:

$$i\hbar\frac{\partial}{\partial t}\hat{\Psi}(\mathbf{r},t) = \left[-\frac{\hbar^2\nabla^2}{2m} + V(\mathbf{r}) + g\hat{\Psi}^\dagger(\mathbf{r},t)\hat{\Psi}(\mathbf{r},t) \right] \hat{\Psi}(\mathbf{r},t). \tag{2.10}$$

2.2 Sculpting with BECs

Bose-Einstein condensates are a popular platform to study quantum many-body physics for many reasons. First of all, they bring the microscopic world of quantum mechanics to a macroscopic level, allowing direct optical observation of phenomena like superfluidity and interference. Additionally, these systems are highly controllable. They can be held stable for relatively long times[2] and many system parameters are tunable using external fields. Furthermore, experiments are readily translated to theory thanks to a detailed understanding of the microscopic Hamiltonian of the systems as they are realised in the laboratory. These properties make them ideal for studying fundamental quantum effects in a more tangible way and to corroborate theoretical predictions.

Particularly interesting is the versatility of the traps that can be applied to hold the atomic cloud in place. Complexity of these traps has come a long way since the first experimental realisations. Currently, the magneto-optical traps used in the pioneering experiments are still standard practice, but many other possibilities exist. In this context, lasers are widely applied for manipulating ultracold atoms. Electric dipole interaction between the neutral atom's induced dipole moment and the electric field can attract or repel particles from regions of high intensity, depending on the detuning of the laser frequency compared to the atomic resonance

[2] Depending on the quality of the trap, typical experiments with ultracold atoms can last from hundreds of milliseconds to several seconds. This sharply contrasts quantum optics experiments, were characteristic times are set by photon lifetime in the cavity and are generally in the range of nanoseconds (10^{-9}s).

[10]. For example, a single laser suffices to introduce simple obstacles in superfluid flows [23–25]. Combining several lasers, most commonly blue-detuned (repulsive), enable the construction of box potentials used to create homogeneous samples [26]. These provide a more direct connection to elementary theoretical models. Alternatively, a periodic lattice potential can be created with two identical, counter propagating beams [27]. Here, we go into a bit more detail on those configurations relevant to this body of work.

2.2.1 Reduced dimensionalities

The ability to independently alter the force constants of trapping potentials along different directions opened the possibility to study Bose-Einstein condensation in lower dimensions. Freezing out motion in one or two dimensions through highly anisotropic confinement, results in pancake shaped or cigar-shaped configurations [28]. This can be achieved by increasing the energy-level spacing in a given direction, such that it exceeds the thermal and interaction energies. In this case, the first excited state in that direction becomes unreachable. In a harmonically trapped cloud, for example, the ν-th dimension is frozen out when $\hbar\omega_\nu \gg k_B T, \mu$.

Physics in these low-dimensional quantum systems is vastly different from their 3D counterpart, particularly long-range order associated with Bose-Einstein condensation, which is suppressed due to an increase in quantum fluctuations. True long-range order is absent in one or two-dimensional configurations [29], leading to the notion of a *quasi-condensate*. This refers to the density matrix tending to zero algebraically (2D) or exponentially (1D), but with a decay length still much longer than the thermal de Broglie wavelength, instead of converging to a constant for true Bose-Einstein condensation [4]. In a quasi-condensate, phase correlations are small compared to system sizes, while still being large compared to microscopic length scales. Interestingly, topological structures are more stable in lower dimensional systems, like solitons in 1D or vortices in 2D, as we will see later on in Chapter 8.

2.2.2 Optical lattice potential

Another tool that can be leveraged to sculpt ultracold gases is the optical lattice potential. Two counter-propagating laser beams with the same wavelength λ that overlap form a standing wave of period $d = \lambda/2$ [27]. Depending on blue or red detuning of the laser, atoms gather at the nodes or anti-nodes of this wave.

Combining three of these identical standing waves, oriented perpendicular to each other, imposes an isotropic 3D trapping potential:

$$V(\mathbf{r}) = -V_0 \left[\cos^2(kx) + \cos^2(ky) + \cos^2(kz)\right], \tag{2.11}$$

with the wave number $k = 2\pi/\lambda$ and the lattice depth V_0 related to the frequency and power of the lasers. This potential, known as an optical lattice, effectively discretize the physical space for the atom cloud when V_0 is sufficiently large.

We consider the Hamiltonian in Eq. (2.9) and substitute the periodic potential. Because this potential is a simple sum of terms depending on one coordinate each, the Hamiltonian readily decouples into independent equations for x, y and z. Choosing to analyse the x-direction, we start from the non-interacting case ($g = 0$):

$$\hat{H} = \int \mathrm{d}x\ \hat{\Psi}^\dagger(x) \left[-\frac{\hbar^2\nabla^2}{2m} - V_0 \cos^2(kx)\right] \hat{\Psi}(x). \tag{2.12}$$

Bloch's theorem states that the exact single-particle eigenstates are given by Bloch functions,

$$\phi_{n,q}(x) = e^{iqx} \cdot u_{n,q}(x), \tag{2.13}$$

plane waves modulated by a periodic function u that has the same periodicity as the lattice. These functions, known from solid state physics, are characterized by a discrete band index n and a quasi-momentum q in the first Brillouin zone, and are highly delocalized, meaning they extend over the whole lattice.

The field operators, that create and annihilate particles, can be expanded in any arbitrary, complete basis $\{f_j\}$,

$$\hat{\Psi}(x) = \sum_j f_j(x)\hat{a}_j, \tag{2.14}$$

with Bloch functions being one possibility, but not the ideal one in our case. An alternative, especially convenient basis is provided by the Wannier functions $w_n(x - x_j)$, connected to the Bloch functions through a Fourier transformation:

$$\phi_{n,q}(x) = \sum_j w_n(x - x_j)e^{iqx_j}. \tag{2.15}$$

These functions also form a complete basis, given that a convenient normalization is chosen [10]. The gaps between consecutive energy bands n grow rapidly with increasing lattice depth. For a dilute gas of cold, weakly interacting atoms the gap

between the first and second Bloch band quickly surpasses all other relevant energy scales [27], i.e. occupations of the higher energy bands are vanishingly small. As such, an expansion in terms of the lowest-band Wannier functions,

$$\hat{\Psi}(x) = \sum_j w_0(x - x_j)\hat{a}_j, \tag{2.16}$$

suffices and results in the discrete Hamiltonian

$$\hat{H} = -J \sum_{\langle i,j \rangle} \left(\hat{a}_i^\dagger \hat{a}_j + \hat{a}_j^\dagger \hat{a}_i \right). \tag{2.17}$$

It represents a grid where single particles can hop between sites at a given tunnelling rate J, defined as

$$J = -\int \mathrm{d}x \; w_0^*(x - x_j) \left[-\frac{\hbar^2 \nabla^2}{2m} - V_0 \cos^2(kx) \right] w_0(x - x_{j+1}). \tag{2.18}$$

The Wannier functions depend solely on the relative distance $|x - x_j|$ and are well-centred around the minima of the periodic potential x_j, at least for the lower bands. This means that atoms are therefore tightly confined around the lattice sites $x_j = d \cdot j$ with only limited tunnelling between sites. The summation in (2.17) therefore only goes over all nearest-neighbours pairs, meaning particles only jump one site in the grid at a time. Contributions to the kinetic energy from particles tunnelling between next-to-nearest neighbours and further is neglected in what is called the *tight-binding approximation*.

Considering now the interacting case ($g \neq= 0$), described by the Hamiltonian in Eq. (2.9), application of the substitution results in the derivation of the famous and celebrated Bose-Hubbard model (BHM):

$$\hat{H} = -J \sum_{\langle i,j \rangle} \hat{a}_i^\dagger \hat{a}_j + \frac{U}{2} \sum_j \hat{a}_j^\dagger \hat{a}_j^\dagger \hat{a}_j \hat{a}_j + \sum_j V_j \hat{a}_j^\dagger \hat{a}_j. \tag{2.19}$$

The dominant contribution to the interaction energy comes from collisions between particles on the same site. This stems again from the vanishingly small overlap of the lowest-band Wannier functions in sufficiently deep lattices. In this case, the on-site interaction strength is given by

$$U = g \int \mathrm{d}x \; |w_0(x)|^4. \tag{2.20}$$

Shifting the Wannier function from the choice $x_j = 0$ does not change the result, because their shape is independent of the lattice site. Lastly, the potential V_j originates from any other external trapping, $V_t(x)$, possibly applied to the system and can be defined as

$$V_j = \int \mathrm{d}x \; w_0^*(x - x_j) V_t(x) w_0(x - x_j) \approx V_t(x_j). \tag{2.21}$$

Here, $V_t(x)$ is assumed to be varying slowly over x in comparison to the lattice potential, so that we can still approximate the Wannier functions to be orthonormal and neglect non-local contributions of this term. Given the lattice depth V_0 in a certain experimental setup, it is in principle possible to calculate all Bose-Hubbard parameters in good approximation. We discuss this in more detail in Appendix A.

2.2.3 Many-body phase diagram

Despite its elegance, the BHM is not exactly soluble, even in 1D. This contrasts its continuous counterpart, the Lieb-Liniger model, which is exactly solvable [30, 31]. Nevertheless, a lot of its key properties are well understood. The Hilbert space dimension $\mathcal{D}$ is finite, but rapidly grows with increasing number of sites L and total particle number N as

$$\mathcal{D} = \frac{(N + L - 1)!}{N!(L - 1)!}. \tag{2.22}$$

The Bose-Hubbard Hamiltonian models the competition between the kinetic term, that attempts to have all atoms delocalized over the lattice in an extended Bloch state, and the interaction term, which for $U > 0$ aims to minimize the number fluctuations of the atoms on each site, counteracting phase coherence due to the noncommutativity of the number and phase operators. When the tunnelling term is dominant, in the limit $U/J \to 0$, energy is minimized by having the N particles delocalized over the L lattice sites. In this *superfluid* (SF) phase, the state of the system is well described by a macroscopic wave function, with long-range phase coherence over the lattice sites. For a homogeneous system, in the absence of additional trapping potentials $V_j = 0$, the many-body ground state is then given by [32]

$$|\Psi\rangle \propto \left(\sum_j^L \hat{a}_j^\dagger \right)^N |0\rangle \,. \tag{2.23}$$

This state is excellently approximated by a product of coherent states at each lattice site. In the opposing limit, $J/U \to 0$, when interactions are dominant, one recovers the *Mott-insulator* (MI) phase, with a fixed, integer number of particles per site $\overline{n}$. The ground state is then given by a product of Fock states

$$|\Psi_{MI}\rangle = \prod_{j}^{L} \left(\hat{a}_j^\dagger\right)^{\overline{n}} |0\rangle \,. \tag{2.24}$$

The most intuitive case is the one with unit-filling $\overline{n} = 1$ on each site. For any finite value $J \neq 0$, the ground state is no longer a simple product state, like in (2.24). However, as long as the gain in kinetic energy J is smaller than the interaction energy U, atoms remain predominantly localized. As soon as $J \gtrsim U$, gain in kinetic energy can outweigh the repulsion due to double occupancy of a well. The systems undergoes a sharp phase transition from a Mott-insulator to a superfluid. Fig. 2.4(a) shows a sketch of the zero-temperature phase diagram as a function of the parameter J/U and varying density set by the chemical potential μ. A key signature are the Mott-insulator lobes at small values of J/U that become smaller with increasing density. At large values of J/U the system always becomes superfluid. Experimentally the ratio J/U can be tuned by changing the depth V_0 of the lattice potential, which has led to the observation of this quantum phase transition [32].

2.2.4 Bose-Hubbard dimer: Josephson oscillations and self-trapping

In the limit $\overline{n} \gg 1$, the BHM is equivalent to an array of Josephson junctions with coupling energy $E_J = 2\overline{n}J$ [10]. When $E_J \gg U$, the ground state is characterized by a uniform order parameter, meaning equal density at each site and a vanishing phase difference between the sites. The smallest possible unit, a single Josephson junction, consists of two weakly coupled BECs, which can be described by two connected order parameters. A bosonic Josephson junction exhibits interesting dynamics when brought out of balance [33], as shown in Fig. 2.4(b) through a series of density snapshots. A relatively small difference induces an alternating current leading to the peak in density switching between the two wells, referred to as *Josephson oscillations*. These oscillations grow as the onset differences becomes larger. However, when the initial difference exceeds a threshold, the population imbalance remains fixed over time, apart from small oscillations. This is a manifestation of macroscopic *self-trapping*, which occurs when the interaction energy is much larger than the kinetic tunnelling energy and superfluid currents become

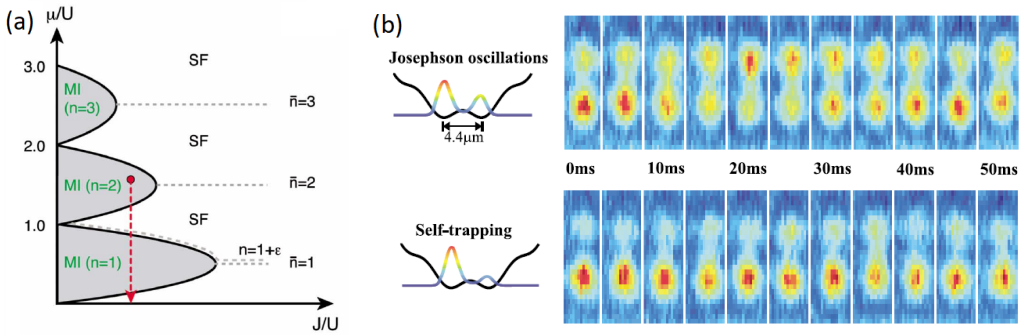

Figure 2.4 – (a) Schematic of the zero-temperature phase diagram of the Bose-Hubbard model. Dashed lines indicate integer filling fractions N/L. Figure reproduced from Ref. [10]. (b) Dynamics of a BEC in a double-well potential following an imposed population imbalance. The top row shows a Josephson oscillation due to an alternating current, while the bottom row displays quantum self-trapping. The latter comes about when the initial imbalance exceeds a critical value. Figure adapted from Ref. [33].

suppressed. Josephson physics is commonly observed in systems that describe two macroscopic coherent wave functions separated by a thin barrier. The most common implementation of a Josephson junction consists of two superconductors connected by an insulator or non-superconducting material.

2.3 Atomtronic applications

Due to the advancement of experimental techniques for handling ultracold atoms, a new research field has emerged, the field of *atomtronics* [34, 35]. The primary objective of this domain is to design analogues of electronic components, based on coherent currents of ultracold neutral atoms instead of electron flows. Studies in this field aim to leverage quantum-mechanical properties in matter-wave circuits, both for fundamental research as well as for technological applications. Through the use of magnetic and light potentials, networks of functional units connected through atomic waveguides are designed to coherently control and manipulate matter waves. On the one hand, the field focuses on exploiting the similarity with the flow of electrons in an electric circuit, but it is not restricted to merely creating analogues of existing components. The hope is to leverage the quantum mechanical nature of ultracold atoms to create useful devices that have no direct electronic analogue.

The importance of optical (lattice) potentials in this emerging field can not be

underestimated. With the effective 1D dynamics that they bring about, these are ideal traps to create waveguides directing atomic currents, mimicking electron flows in solid-state crystalline materials. Lattice based devices, like diodes or transistors, have been theorized by leveraging the Mott-insulator phase and superimposing additional potentials that modify the lattice at individual sites [36–39]. Circuit dynamics is always driven by a battery, an applied voltage that in an atomtronic setting corresponds to an effective difference in chemical potential [38, 40, 41]. Furthermore, ring-shaped lattice potentials deep in the superfluid regime can serve as the atomic counterpart of a SQUID, a superconducting quantum interference device[3] [42, 43]. Such Josephson junction necklaces, containing one or two links, have a clear potential of being used as rotational or magnetic field sensors [44–46]. The aim of this section is not to propose the direct relevance of this body of work to one or the other atomtronic device, but rather to convince the reader of the general interest in this domain. Besides the search for new and possibly better circuit components, atomtronic systems have proven useful for probing a diverse range of many-body quantum regimes.

In this thesis, focus lies on a particular setup that has been investigated in a number of experimental studies [47–51]. It is realized by loading a gas of rubidium-87 atoms into a highly anisotropic, harmonic trap and cooling it down till below the critical temperature, resulting in a so-called *cigar-shaped* BEC. While this puts the focus on the physics in the elongated direction, the cloud still retains a significant radial size. Additionally, a 1D lattice potential is applied in the longitudinal direction, effectively breaking up the system into an array of small quasi-2D condensates linked in sequence. A schematic representation is given in Fig. 2.5. Each link in the array represents a Josephson junction between two BEC of roughly 700 atoms harmonically trapped in the transverse directions. Atoms can move in the z-direction, through the lattice, by hopping between adjacent sites at a tunnelling rate J. The final ingredient is a very precise external loss mechanism. With a focused electron beam, atoms at one specific site in the centre of the array are ionized and this way extracted from the setup [52]. The rate γ at which particles are lost from the trap can conveniently be tuned by the intensity of the electron beam.

This setup, that tends towards an equal distribution of its atoms over all sites [4], is

[3] These tiny devices are extremely sensitive magnetometers, capable of measuring magnetic fields of the order 10^{-18}T.

[4] The kinetic energy in the lattice dominates over the interaction energy. This corresponds to the superfluid phase in the Bose-Hubbard model.

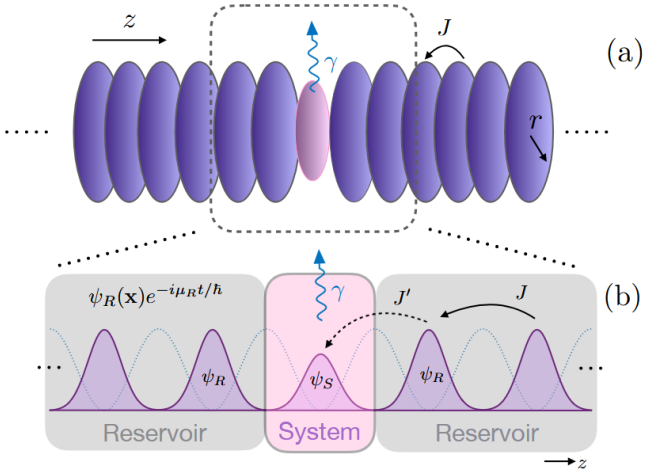

Figure 2.5 – Schematic representation of the (dissipative) quasi-1D Josephson array. The configuration is realised by superimposing a lattice potential in the z-direction and harmonic trapping in the transverse directions. A focused electron beam can kick atoms out of the system with single site precision. Focus lies on the centre, where the beam is focused. The large sequences of wells on the left and right act as reservoirs. Figure reproduced with permission from Ref. [53].

driven far from equilibrium by this engineered dissipation. In the first experiment of the series, losses are turned on temporarily to create a local density dip, after which the relaxation dynamics in the closed system was tracked. This led in Ref. [47] to the observation of *negative differential conductivity* (NDC) in the atomic currents towards the centre. More precisely, this means that in the regime of large voltages, i.e. large chemical potential difference, the current is inversely related to the voltage, contrasting the regular Ohmic relation at small voltages. Interestingly, the AC Josephson effect characteristic of a two-mode Josephson junction is absent here, marked by the lack of oscillations on top of the DC current into the initially emptied well.

It stands to reason that this observation sparked even more interest in this specific configuration, given that NDC is not uncommon in semiconductors[5]. Follow-up experiments [48, 50, 51] considered the setup under continued losses, prohibiting the system from relaxing. In this case, the central site is drained relentlessly, while superfluid currents from the left and right internal reservoirs try to counter these

[5] In the context of semiconductor physics, NDC is sometimes referred to as negative resistance.

losses. It is exactly this competition between driving and dissipation that gives rise to interesting non-equilibrium steady states, drive dissipative phase transitions, and generally give rise to rich dynamical phenomena inaccessible in closed systems. The aforementioned experimental works have instigated a number of theoretical studies [53–56], including the work that we are about to present here. Before we do so, however, it is important to briefly discuss the framework of open quantum systems, serving as the foundation for our understanding of the physics at hand.

CHAPTER 3

Open quantum systems

The idealistic representation of a quantum system like an ultracold gas as completely decoupled from its environment is practical, because it allows a description of the dynamics in terms of a unitary time evolution. Nevertheless, any physical setup is in reality part of a bigger system and as such constantly subject to decoherence, particle losses, heat transfer, etc. due to interactions with their surroundings. Furthermore, an additional coupling is introduced every time one performs a measurement of the system of interest. This can induce non-unitary dynamics and might even lead to the destruction of the exact quantum mechanical effects one aims to observe. It is therefore crucial to develop a framework that includes the effect of the environment on the regular Hamiltonian dynamics at least up to some degree of accuracy.

The study of open quantum systems is interesting also from a fundamental point of view, as they feature a wide range of out-of-equilibrium phenomena that are generally out of reach in isolated systems. Studies in recent years have shown that for some systems a well-chosen coupling to their environment can be beneficial and drive them to desired highly entangled states [57–60]. Combining such engineered dissipation with internal or external driving has led in a variety of systems to exotic nonequilibrium steady states (NESSs) that otherwise cannot be reached in closed systems [48, 61–65]. Properties of these NESSs often greatly differ from the thermal equilibrium states of the Hamiltonian. Increasing control over open quantum systems is also of key importance for the application in a number of

quantum technologies.

3.1 Dynamics of open quantum system

Our system of interest S is thus a subsystem of a larger whole that includes the environment E, where the combined system can generally be assumed closed. The Hilbert space of all states of the entire system is then simply the tensor product of the two subspaces,

$$\mathcal{H} = \mathcal{H}_S \otimes \mathcal{H}_E, \tag{3.1}$$

with the properties determined by the full Hamiltonian

$$\hat{H}(t) = \hat{H}_S \otimes \mathbb{I}_E + \mathbb{I}_S \otimes \hat{H}_E + \hat{H}_I(t). \tag{3.2}$$

One can distinguish the system and environment Hamiltonians together with the interaction term describing the coupling. In principle, evolution of the complete setup $S+E$ can be tracked by means of the Liouville-von Neumann equation,

$$i\hbar \frac{\mathrm{d}}{\mathrm{d}t}\hat{\rho} = \left[\hat{H}(t), \hat{\rho}\right]. \tag{3.3}$$

The reason we make a distinction of the sub-system S from the whole stems from the fact that all our observations will refer solely to this subsystem, i.e. all observables of interest to us are of the form $\hat{A} = \hat{A}_S \otimes \mathbb{I}_E$. Here, operator $\hat{A}_S$ acts on the Hilbert space $\mathcal{H}_S$, whereas $\mathbb{I}_E$ is the identity operator for the space of all environment states. As a result, when the state of the combined system is described by a density matrix $\hat{\rho}$, the expectation value for any observable acting on the subsystem S is determined by

$$\langle \hat{A} \rangle = \mathrm{Tr}_S \left\{ \hat{A}\hat{\rho}_S \right\}, \tag{3.4}$$

where $\hat{\rho}_S = \mathrm{Tr}_E\{\hat{\rho}\}$ is the *reduced density matrix*, obtained by integrating out the degrees of freedom of the environment. For the purpose of monitoring the open system, we're not interested in the enormous amount of possible states of the environment, but merely in its effect on the dynamics of the system. The equation of motion for the density matrix $\hat{\rho}_S$ is found similarly by taking the trace on both sides of the von Neumann equation for the entire system:

$$i\hbar \frac{\mathrm{d}}{\mathrm{d}t}\hat{\rho}_S = \mathrm{Tr}_E \left[\hat{H}(t), \hat{\rho}_S\right]. \tag{3.5}$$

The above equation is exact and remains too elaborate to solve. Luckily, in many practical settings the system is only weakly coupled to a *markovian* environment. A number of convenient properties can then be leveraged to derive a viable framework for determining $\hat{\rho}_S(t)$.

3.1.1 A Markovian environment: the Lindblad master equation

The dynamics of the reduced system, represented by Eq. (3.5), can be reformulated when it weakly couples to a very large environment. The effect of weak interactions from a much smaller system on the environment quickly becomes negligible with increasing number of environmental degrees of freedom. Additionally, for such a large system correlations generally decay over a time τ_E that is much smaller than τ_R, the typical time over which interesting dynamics occurs in the system. In other words, memory of the environment is lost much faster compared to the resolution at which we resolve $\hat{\rho}_S(t)$. Applying these assumptions, referred to as the *Born-Markov approximation*, leads to a more convenient, simplified representation in terms of a linear differential equation

$$\frac{\mathrm{d}}{\mathrm{d}t}\hat{\rho}_S(t) = -\frac{i}{\hbar}\left[\hat{H}_S, \hat{\rho}_S\right] + \mathcal{D}(\hat{\rho}_S), \tag{3.6}$$

called the Lindblad master equation[1] [66, 67]. The second term, referred to as the dissipator or damping operator, is given by

$$\mathcal{D}(\hat{\rho}_S) = \frac{1}{2}\sum_j \left(2\hat{\Gamma}_j\hat{\rho}_S\hat{\Gamma}_j^\dagger - \hat{\Gamma}_j^\dagger\hat{\Gamma}_j\hat{\rho}_S - \hat{\rho}_S\hat{\Gamma}_j^\dagger\hat{\Gamma}_j\right). \tag{3.7}$$

The Lindblad or jump operators $\hat{\Gamma}_j^\dagger$ and $\hat{\Gamma}_j$ capture the effect of the environment on the system. Their exact form will depend on the type of interactions. If we omit the interaction with the environment Eq. (3.6) reduces again to the regular von Neumann equation, representing the system's unitary dynamics.

Because the differential equation is linear in $\hat{\rho}_S$, it can be written in terms of the Liouvillian $\mathcal{L}$ [67]:

$$\frac{\mathrm{d}}{\mathrm{d}t}\hat{\rho}_S = \mathcal{L}\hat{\rho}_S. \tag{3.8}$$

Formally, this equation is readily solved for any initial density matrix, i.e. $\hat{\rho}(t) = \exp(\mathcal{L}t)\hat{\rho}(0)$. The Liouvillian is a *superoperator*, acting on operators to produce

[1] Credit where credit is due, the equation is also known under its full name, the Gorini–Kossakowski–Sudarshan–Lindblad equation.

different ones. It is a trace preserving and completely positive map, ensuring that the requirements on the density matrix remain satisfied [68]. In analogy with the Hamiltonian for a closed system, all properties of the open system can be determined through diagonalization of the Liouvillian [69, 70]. From here on we will drop the subscript S and simply refer to the reduced density matrix as the open system's density matrix $\hat{\rho}$.

3.2 Dissipative phase transitions

It is clear from the master equation in Lindblad form, Eq. (3.6), that the evolution of the density matrix is governed by a competition between unitary Hamiltonian dynamics and the effect of the dissipator $\mathcal{D}(\hat{\rho})$. This interplay can lead to novel phenomena, inaccessible in closed systems. Particularly interesting is a new type of phase transition that is brought about, a dissipative phase transition. We provide a short summary of the general framework of dissipative phase transitions in terms of the spectral properties as it was reported in Refs. [63, 69], with the goal of providing insight in the results presented in the second part of the thesis.

3.2.1 Thermal and quantum phase transitions

One can generally differentiate phases of matter based on just a few macroscopic observables. States of the system are uniform in these macroscopic properties within the same phase. A phase transition takes place when a drastic change occurs in a certain property as a consequence of some external parameter ζ crossing a critical point ζ_c. A general classification exists for the *order* of a transition based on the manner in which the parameter(s) change. A *first-order phase transition* features a discontinuous jump in some observable, while a *second-order phase transition* is characterized by a continuous change in some quantity that is not continuously differentiable. Common examples of the former are the freezing or evaporation of water. The density of (pure) water makes a discontinuous jump at 0°C as well as 100°C, relating to the exchange of latent heat. An example of a second-order or continuous phase transition is the ferromagnetic transition across the Curie temperature.

An insightful phenomenological theory of phase transitions was introduced by Lev Landau, originally to better understand second-order transitions [71]. It describes the free energy of a system in terms of an *order parameter* σ, an extensive and experimentally accessible parameter that should be zero in one phase ($\zeta > \zeta_c$)

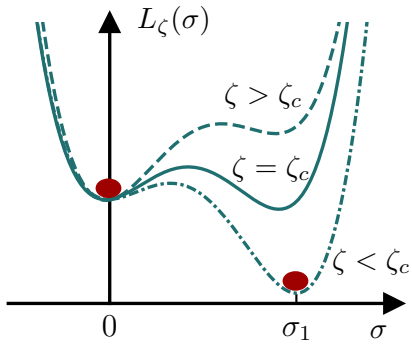

Figure 3.1 – Landau theory of a first-order phase transition. As the parameter ζ crosses the critical point ζ_c, the global minimum switches from $\sigma = 0$ to $\sigma = \sigma_1$.

and non-zero in the other ($\zeta < \zeta_c$). The Landau free energy functional $L_\zeta(\sigma)$, parametrised by the relevant parameter ζ, presents an effective potential whose minimum the system seeks to reside in. Including the lowest orders in an expansion of the free energy suffices to accurately describe phase transitions. Fig. 3.1 schematically shows how the Landau free energy changes for a first order transition as the criticality ζ_c is crossed. The local minimum at a finite value for σ suddenly becomes the new global minimum, resulting in a discontinuous change of σ from zero to σ_1. Here, one can also notice the local maximum in the centre of the potential. When the system resides in the elevated local minimum, it has to overcome this barrier in order to relax to the state of least energy. This makes the higher-energy phase a *metastable* state, a state with finite lifetime. A metastable state can be long-lived, but never eternal, since thermal or quantum fluctuations will generally be sufficient to overcome the barrier in the long run. The presence of metastable states naturally leads to the display of *hysteresis*, an effect that is of key importance in this work.

Different types of phase transitions can occur, depending on which quantity takes up the role of Landau free energy. A classical, *thermal phase transition* (TPT) occurs for thermodynamic systems at equilibrium, whose phase is determined by minimizing the Helmholtz free energy $\mathcal{F} = E - TS$ [71]. Competition between the system's internal energy E and its entropy S due to thermal fluctuations can drive a phase transition, with temperature T as a control parameter. In contrast, a quantum system at $T = 0$ has no entropy and occupies the ground state, minimizing its energy. A *quantum phase transition* (QPT) can still take

place, as a result of competing noncommuting terms in the Hamiltonian [72]. A QPT is generally related to an avoided level crossing in the Hamiltonian's energy spectrum, i.e. the ground state and an excited energy level approach as function of a Hamiltonian parameter. The system's ground state is changed from one configuration to a qualitatively different one when going through such a level crossing at the critical point.

An open quantum system interacting with a Markovian environment is, as we have seen above, governed by the time-independent master equation $\mathrm{d}\hat{\rho}/\mathrm{d}t = \mathcal{L}(\zeta)\hat{\rho}$. The unique steady-state should satisfy $\mathcal{L}(\zeta)\hat{\rho}(\zeta) = 0$. In analogy to the considerations above, we can say that this state minimizes the norm[2] $\|\mathcal{L}\rho\|_{\mathrm{Tr}}$, implying that the Liouvillian plays somewhat the role of free energy. Changing parameters in the Liouvillian, e.g. the strength of the unitary part relative to the dissipative processes, can induce a *dissipative phase transition* (DPT).

3.2.2 Spectral theory of the Liouvillian

Although there are significant differences, the analogy between the quantum and dissipative phase transition follows through quite far. More specifically, the concept of an (avoided) level crossing has a counterpart in the spectral theory of the Liouvillian. Similar to the properties of a closed system being determined by the eigenvectors/values of the Hamiltonian, the dynamics of the open system is fully determined by the spectral decomposition of the Liouvillian. A convenient basis is given by the *eigenmatrices* of the Liouvillian, defined as

$$\mathcal{L}\hat{\rho}_i = \lambda_i \hat{\rho}_i, \tag{3.9}$$

where a typical Liouvillian spectrum is shown schematically in Fig. 3.2(a) [66, 70]. The existence and uniqueness of a steady-state density matrix $\hat{\rho}_{ss} \propto \hat{\rho}_0$, corresponding to the eigenvalue $\lambda_0 = 0$, can be proven under quite general conditions [74–76]. When $\mathcal{L}$ is diagonalizable, its set of eigenstates provides a convenient basis for any density matrix at $t = 0$,

$$\hat{\rho}(0) = \hat{\rho}_{ss} + \sum_{i \geq 1} c_i \hat{\rho}_i, \tag{3.10}$$

[2] The tracenorm is defined as $\|A\|_{\mathrm{Tr}} \equiv \mathrm{Tr}\left[\sqrt{A^\dagger A}.\right]$ [73]

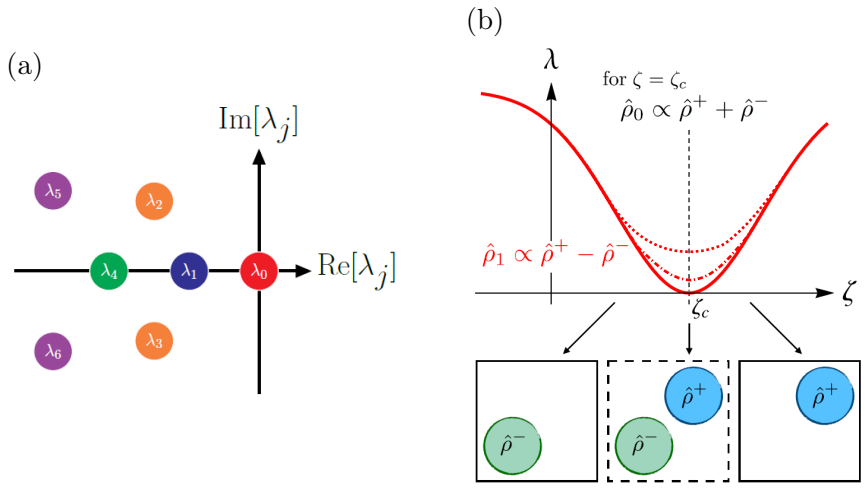

Figure 3.2 – (a) Schematic representation of the Liouvillian spectrum. Apart from the generally unique steady-state, corresponding to $\lambda_0 = 0$, all eigenvalues have a negative real part. Figure reproduced from Ref. [70]. (b) Mechanism of a dissipative first-order phase transition. In the thermodynamic limit the Liouvillian gap $\lambda = |\mathrm{Re}[\lambda_1]|$ closes at the critical point ζ_c. At this point the steady-state is a bimodal mixture of the system's physical state before ($\hat{\rho}^-$) and after ($\hat{\rho}^+$) the criticality. The interrupted lines represent the behaviour of λ around the critical point for finite systems. Figure adapted from Ref. [69].

and consequently at any ensuing time t under evolution by the Liouvillian:

$$\hat{\rho}(t) = e^{\mathcal{L}t}\hat{\rho}(0) = \hat{\rho}_{ss} + \sum_{i\geq 1} c_i e^{\lambda_i t}\hat{\rho}_i. \tag{3.11}$$

Because generally $|\mathrm{Re}\,(\lambda_{i\geq 1})| < 0$ [66], it is easy to see that the eigenstates $\hat{\rho}_i$ are probed over finite times in the transient dynamics, except for $\hat{\rho}_0$. Contributions in the density matrix decomposition decay exponentially, with the longest relaxation time determined by λ_1. The slowest relaxation dynamics occurs on a characteristic time scale that is the inverse of the *Liouvillian gap*, $\lambda = |\mathrm{Re}(\lambda_1)|$. It is important to highlight that the eigenstates $\hat{\rho}_i$ are not physical density matrices, i.e. $\mathrm{Tr}[\hat{\rho}_i] = 0$ if $\mathrm{Re}[\lambda_i] \neq 0$. Due to the trace preserving property of the Liouvillian and the requirement that the limit $\lim_{t\to\infty} e^{\mathcal{L}t}\hat{\rho}(0) = \hat{\rho}_{ss}$ is satisfied for any initial density matrix, the steady state must be given by $\hat{\rho}_{ss} = \hat{\rho}_0/\,\mathrm{Tr}[\hat{\rho}_0]$.

3.2.3 Dissipative first-order phase transition and metastability

A first-order phase transition in an open quantum system is characterized by a discontinuous change in the expectation value of an observable in the steady-state, $\langle\hat{O}\rangle = \mathrm{Tr}\left[\hat{\rho}_{ss}\hat{O}\right]$, when some parameter ζ passes a criticality ζ_c. A formal definition is given by [69]

$$\lim_{\zeta\to\zeta_c}\left|\frac{\partial}{\partial\zeta}\,\mathrm{Tr}\left[\hat{\rho}_{ss}(\zeta)\hat{O}\right]\right| = \infty, \tag{3.12}$$

for the system in its thermodynamic limit. Because of the observable's independence of ζ, the non-analytic behaviour is due to a discontinuity in the non-equilibrium steady-state. In close vicinity of the critical point, two distinct steady-states can be identified

$$\lim_{\zeta\to\zeta_c^-}\hat{\rho}_{ss}(\zeta) \equiv \hat{\rho}^- \neq \hat{\rho}^+ \equiv \lim_{\zeta\to\zeta_c+}\hat{\rho}_{ss}(\zeta). \tag{3.13}$$

It can be inferred from this that at the critical point the steady-state has a double degeneracy, $\mathcal{L}(\zeta_c)\hat{\rho}^{\pm} = 0$, implying that $\lim_{\zeta\to\zeta_c}\lambda_1(\zeta) = \lambda_0 = 0$. Consequently, both $\hat{\rho}_0(\zeta_c)$ and $\hat{\rho}_1(\zeta_c)$ belong to the linear span of $\{\hat{\rho}^{\pm}\}$, more specifically $\hat{\rho}_0(\zeta_c) \propto \hat{\rho}^+ + \hat{\rho}^-$ and $\hat{\rho}_1(\zeta_c) \propto \hat{\rho}^+ - \hat{\rho}^-$ [69]. Note that this satisfies the respective trace conditions for both eigenmatrices. From this we can conclude that the steady state at the critical point is bimodal; an equiprobable statistical mixture of the states before and after this point. A schematic of the gap closing is depicted in Fig. 3.2(b), from which the analogy with a level crossing in the spectrum of the Hamiltonian, related to a QTP in a closed system, becomes clear.

Metastability can occur when a number of low-lying modes in the Liouvillian spectrum become separated, i.e. when for the m-th mode holds that $|\mathrm{Re}[\lambda_m]| \ll |\mathrm{Re}[\lambda_{m+1}]|$. This leads to a natural separation of timescales in the relaxation dynamics [73]. In close vicinity of the first-order critical point, where the Liouvillian gap closes, this is the case for the lowest eigenvalues λ_1 and λ_0, so for $m = 1$. Time evolution of the density matrix from an arbitrary initial state $\hat{\rho}(0) = \sum c_i\hat{\rho}_i$ can then be written as

$$\hat{\rho}(t) = \hat{\rho}_{ss} + e^{\lambda_1 t}c_1\hat{\rho}_1 + \sum_{i=2} e^{\lambda_i t}c_i\hat{\rho}_i. \tag{3.14}$$

Evidently, all contributions in the summation become negligibly small at times $t \gg \tau' = 1/|\mathrm{Re}[\lambda_2]|$, assuming that the coefficients $c_{i\geq 2}$ of the initial state decomposition are not too large. The timescale τ' characterizes a short relaxation

transient. Concurrently, given that λ_1 is real in a finite region around ζ_c[3] and for times $t \ll \tau = 1/\lambda$, the exponential in the second term can be expanded to give

$$\hat{\rho}(t) \approx [\hat{\rho}_{ss} + c_1\hat{\rho}_1] + t\lambda_1 c_1\hat{\rho}_1 + \sum_{i=2} e^{\lambda_i t} c_i\hat{\rho}_i. \tag{3.15}$$

The separation of two different levels of relaxation become clear from this notation and more peculiarly a window of metastability appears. After an initial transient, where the system relaxes into the *metastable manifold* [73], dynamics remains seemingly stationary when $\tau' \ll t \ll \tau$ and the last two terms in Eq. (3.15) are negligible. The state is approximately described by $\hat{\rho}_{ms} = \hat{\rho}_{ss} + c_1\hat{\rho}_1$, determined in full by the initial density matrix. In a final stage the dynamics exhibits a further relaxation towards the unique stationary state, at times $t \gtrsim \tau$.

This result also relates back to a system in the vicinity of a first-order phase transition. Indeed, from the requirement of continuity we can deduce that

$$\hat{\rho}_1(\zeta) \simeq \hat{\rho}^+ - \hat{\rho}^- \tag{3.16}$$

not only at the critical point, but also in close proximity to it. In this region we find for the spectral decomposition of any initial density matrix that $c_1 \in [-1, 1]$ [69, 73]. Consequently, any metastable state is a statistical mixture of the two *extreme metastable states* $\hat{\rho}^+_{ems}$ and $\hat{\rho}^-_{ems}$, which we can readily identify as

$$\hat{\rho}^\pm_{ems} = \hat{\rho}^\mp \pm \left(\hat{\rho}^+ - \hat{\rho}^-\right) = \hat{\rho}^\pm. \tag{3.17}$$

To put it differently, if we were to initialize the system below (above) the critical point in the physical state $\hat{\rho}^+$ ($\hat{\rho}^-$), it would remain stationary for a time $\mathcal{O}(1/\lambda)$ before relaxing further, resulting in the typical hysterical behaviour at finite times.

Phase transitions are strictly speaking only defined in a system's thermodynamic limit. Systems with a finite number of degrees of freedom will never know any true non-analyticity in their properties. For a finite system the phase will still change when crossing ζ_c, but with rounding of the discontinuity. For a dissipative first-order phase transition this means that the Liouvillian gap will become small, yet never truly zero. This is represented by the interrupted lines in Fig. 3.2(b), again

[3] Because complex eigenvalues λ_i appear as conjugate pairs, λ_1 can only approach zero over the real axis. If $\mathrm{Im}[\lambda_1] \neq 0$ for $\zeta \simeq \zeta_c$, then also $\lambda_2 = \lambda_1^*$ would go to zero in the critical point, resulting in a triple degeneracy [69].

resembling an avoided crossing for a QPT. The steady state will then be a bimodal statistical mixture in a region around ζ_c, with the weight gradually moving from one solution to the other. For a large enough system, $\lambda(\zeta)$ will generally come close enough to zero at the critical point that the argument on separating timescales still holds. The transition often becomes visibly steeper as the thermodynamic limit is approached.

CHAPTER 4

Theoretical methods for simulating many-body quantum systems

Treating any many-body system, open or closed, is a challenging undertaking. Due to the exponential scaling of the Hilbert space with particle number/system size, exact analytic solving of the von Neumann or Lindblad master equations is limited to only a hand-full of small systems. More often than not, one requires methods of approximation to gain more insight in dynamics or ground state properties. In this chapter we elaborate on those methods relevant to the research covered in this thesis.

4.1 Mean-field approximation

A macroscopic number of particles populating the same single-particle state $\Phi(\mathbf{r})$ and behaving collectively justifies the introduction of the order parameter or condensate wave function $\Psi_0(\mathbf{r}) = N_0^{1/2}\Phi(\mathbf{r})$. In the mean-field approximation the field operator $\hat{\Psi}(\mathbf{r}, t)$ is replaced by this classical field Ψ_0, equivalent to disregarding fluctuations on top of the mean value $\Psi_0(\mathbf{r}, t) = \langle\hat{\Psi}(\mathbf{r}, t)\rangle$. Here, the noncommutativity of the operators is neglected and one describes fields with purely classical functions. Remembering that the field operators fulfil the Heisenberg equation (2.10), taking the expectation value results in the generalized, time-dependent

Gross-Pitaevskii equation (GPE)

$$i\hbar\frac{\partial\Psi_0}{\partial t} = \left(-\frac{\hbar^2\nabla^2}{2m} + V(\mathbf{r}) + g|\Psi_0(\mathbf{r},t)|^2\right)\Psi_0(\mathbf{r},t). \tag{4.1}$$

For stationary wavefunctions the right hand side equals $\mu\Psi_0$, with the chemical potential $\mu = \partial E/\partial N$, resulting in the time-independent GPE. To retain consistency, the time evolution in the case of a stationary solution takes the simple form

$$\Psi_0(\mathbf{r},t) = \Psi_0(\mathbf{r})\exp\left(-\frac{i\mu t}{\hbar}\right). \tag{4.2}$$

The ground state is found as the lowest energy solution to the time-independent GPE and is often real-valued, whereas excited states like a solitonic state are usually complex. Formally, the GPE describes a (non-uniform) dilute Bose gas at zero temperature. However, the mean-field approach generates quantitatively accurate results even at low temperatures when the interactions are sufficiently weak. A general condition is a negligible occupation of modes other than the condensate mode, the thermal occupation, relative to condensate occupation N_0. Throughout this work, the GPE will be employed consistently to obtain a first estimate of the ground state properties or dynamical behaviour of a systems of interest.

4.2 Bogoliubov-de-Gennes formalism

The mean-field approach can be regarded as the zeroth-order approximation in an expansion of the field operator in a mean part and quantum fluctuations around this mean:

$$\hat{\Psi}(\mathbf{r},t) = e^{-i\mu t/\hbar}\left[\Psi_0(\mathbf{r},t) + \delta\hat{\Psi}(\mathbf{r},t)\right], \tag{4.3}$$

where the fluctuation operator can be expanded in terms of elementary excitations, represented by the bosonic particle operators $\hat{b}_i, \hat{b}_i^\dagger$, as

$$\delta\hat{\Psi}(\mathbf{r},t) = \sum_i\left[u_i(\mathbf{r})\hat{b}_i e^{-i\omega_i t} + v_i^*(\mathbf{r})\hat{b}_i^\dagger e^{i\omega_i^* t}\right]. \tag{4.4}$$

When the complex amplitudes satisfy the orthonormalization conditions

$$\int \mathrm{d}^3\mathbf{r}\ \left[u_i(\mathbf{r})u_j^*(\mathbf{r}) - v_i(\mathbf{r})v_j^*(\mathbf{r})\right] = \delta_{i,j}, \tag{4.5}$$

substitution of (4.3) into the Hamiltonian for a uniform Bose gas ($V(\mathbf{r}) = 0$) results in a diagonalized Hamiltonian[1]

$$H^{(2)} = \sum_i \hbar\omega_i \hat{b}_i^\dagger \hat{b}_i. \tag{4.6}$$

This procedure, known as the *Bogoliubov approximation*, treats a weakly interacting Bose gas as a gas of non-interacting quasi-particles, fundamental excitations. The elementary quantum fluctuations can also be interpreted as classical, small-amplitude oscillations, which means that solutions of the eigenfrequencies ω_i, and amplitudes u_i and v_i, are equivalently obtained in the Gross-Pitaevskii picture. In analogy with the fluctuation operator, the classical fluctuation field is

$$\delta\Psi(\mathbf{r}, t) = \sum_i \left[u_i(\mathbf{r}) e^{-i\omega_i t} + v_i^*(\mathbf{r}) e^{i\omega_i^* t} \right]. \tag{4.7}$$

Functions $u_i(\mathbf{r})$ and $v_i(\mathbf{r})$ are obtained by solving the time-dependent GPE in the linear limit. One obtains a coupled set of equations,

$$\hbar\omega_i \begin{pmatrix} u_i(\mathbf{r}) \\ v_i(\mathbf{r}) \end{pmatrix} = B \begin{pmatrix} u_i(\mathbf{r}) \\ v_i(\mathbf{r}) \end{pmatrix} \tag{4.8}$$

with the Bogoliubov matrix

$$B = \begin{bmatrix} -(\hbar^2/2m)\nabla^2 + V - \mu + 2g|\Psi_0|^2 & g\Psi_0^2 \\ -g(\Psi_0^*)^2 & (\hbar^2/2m)\nabla^2 - V + \mu - 2g|\Psi_0|^2 \end{bmatrix}. \tag{4.9}$$

Solutions of the Bogoliubov equations are thus found as eigenfunctions $(u_i,\ v_i)^T$ of the Bogoliubov matrix B with eigenvalues $\epsilon_i = \hbar\omega_i$.

One can see that for each solution with eigenvalue ϵ_i, a corresponding eigenvalue $\epsilon_j = -\epsilon_i^*$ exists with eigenfunction $(u_j,\ v_j)^T = (-v_i^*,\ -u_i^*)^T$. From Eq. (4.8) it also follows that [4]

$$(\epsilon_i - \epsilon_j^*) \int \mathrm{d}^3\mathbf{r}\ (u_i u_j^* - v_i v_j^*) = 0 \tag{4.10}$$

should hold. This tells us that if an oscillation mode has a complex eigenvalue the norm, defined as

$$\int \mathrm{d}^3\mathbf{r}\ (|u_i|^2 - |v_i|^2), \tag{4.11}$$

[1] Here we have left out the constant terms corresponding to the ground state energy.

vanishes. A mode with complex eigenvalue will grow exponentially and therefore indicates a dynamic instability of the stationary solution $\psi_0(\mathbf{r})$. If, on the other hand, all eigenfrequencies for a given solution are real, but there exists a mode with negative norm, the solution is energetically unstable. This implies that the stationary solution is not the ground state, but does not necessarily mean that the state is unstable [77]. Because the (real-valued) condensate wavefunction ψ_0 satisfies the GPE, the presence of a zero eigenvalue mode $(u_1,\ v_1)^T = (\psi_0, -\psi_0)^T$ is evident. This mode, with a norm equal to zero, is consistent with a global phase rotation of the condensate wavefunction and is inseparably linked to the spontaneous breaking of the continuous $U(1)$ phase symmetry that occurs over the transition to a condensate. This zero-mode is referred to as the *Goldstone mode*. Throughout this work, the above mentioned formalism is leveraged to determine corrections to mean-field solutions as well as determine their stability under small perturbations. These solutions can be obtained through real or imaginary time evolution of the GPE.

4.3 Phase space methods

Essential in the treatment of a system in classical mechanics is the notion of the phase space. This collection of points, each corresponding to a unique state of the system, spans all possible states, with each axis representing a degree of freedom. For quantum systems, described by a density matrix, an analogous concept exists, where states can be defined in the space of coherent phases. Unlike in classical mechanics, quantum states are prevented from being portrayed by a single point in phase space due to the Heisenberg uncertainty principle. Consequently, even a pure quantum state corresponds to a *quasi-probability function* with a finite spread. Different phase-space descriptions have been developed over the years, each with their own merits and drawbacks. Initially applied in quantum optics [67, 78, 79], these methods are now effectively adapted to atomic systems [53, 60, 80–82]. They are particularly of great use due to their compatibility with classical noise theory, enabling more intuitive analyses.

4.3.1 Coherent states

In second quantization, each bosonic mode is treated as a harmonic oscillator, acted on by the creation and annihilation operators analogous to the ladder operators of the harmonic oscillator introduced in first quantization. For a single mode,

one can introduce in a similar way the hermitian amplitude operators [78]

$$\begin{aligned} \hat{X} &= \frac{\hat{\psi} + \hat{\psi}^\dagger}{2}, \\ \hat{P} &= \frac{\hat{\psi} - \hat{\psi}^\dagger}{2i}, \end{aligned} \tag{4.12}$$

that serve as dimensionless position and momentum operators. These operators satisfy the commutation relation

$$\left[\hat{X}, \hat{P}\right] = \frac{i}{2}, \tag{4.13}$$

implying a minimum uncertainty product:

$$\Delta\hat{X}\Delta\hat{P} \geq \frac{1}{4}, \tag{4.14}$$

where the variance of an operator $\hat{O}$ is defined as $\Delta\hat{O} = \left\langle (\hat{O} - \langle\hat{O}\rangle)^2 \right\rangle$. Coherent states not only have minimal uncertainty, but also have equal uncertainties in both quadrants ($\Delta\hat{X} = \Delta\hat{P} = 1/2$) and are therefore the quantum mechanical state closest to a classical state. Coherent states, denoted as $|\lambda\rangle$, are generated from the vacuum by application of the displacement operator [78, 79]:

$$|\lambda\rangle = D(\lambda)\,|0\rangle = \exp\left(\lambda\hat{\psi}^\dagger - \lambda^*\hat{\psi}\right)|0\rangle\,, \tag{4.15}$$

where λ is any complex number. Coherent states can contain an indefinite number of particles, but possess a well-defined phase. Despite their non-orthogonality, coherent states form an overcomplete set and can therefore be used as a basis for expanding more complex quantum states.

4.3.2 P- and Q-representations

Two representations widely used in quantum optics are the *Glauber* P- and *Husimi* Q-representations, which are both obtained by expanding the density matrix in the basis of coherent states. Moments of the P- and Q-function correspond respectively to expectation values of normally and anti-normally ordered operator products [67, 79]. These ordering conventions are crucial to account for the loss of noncommutativity when transitioning from quantum operators $\hat{\psi}$ to classical variables ψ. Both representations have their particular strengths and limitations. For certain states the P-function approximates a classical probability, though for some

quantum states no valid P-representation exists [79]. In contrast, the Q-function is always non-negative and exists for those states lacking a P-distribution. Both representations are mathematically connected [67], and while both are central to phase space analysis, a detailed description of these representations would bring us too far from the core of the matter. We kindly refer the interested reader to the references mentioned at the beginning of this section for more details on these and other phase space representations.

4.3.3 Wigner function

The Wigner W-function, originally designed by Wigner in 1932 [83], was historically the first distribution. It was initially formulated as a quasi-probability in position and momentum space for a single particle and is most conveniently defined through the characteristic function,

$$\chi_W(\lambda, \lambda^*) = \mathrm{Tr}\left\{\hat{\rho}\exp\left(\lambda\hat{\psi}^\dagger - \lambda^*\hat{\psi}\right)\right\}, \tag{4.16}$$

the expectation value of the displacement operator. Similar to classical probability distributions, the Wigner function is computed as the Fourier transform of the characteristic function:

$$W(\psi, \psi^*) = \frac{1}{\pi^2}\int \mathrm{d}^2\lambda\ \exp(\lambda^*\psi - \lambda\psi^*)\chi_W(\lambda, \lambda^*), \tag{4.17}$$

where $\mathrm{d}^2\lambda = \mathrm{dRe}[\lambda]\mathrm{dIm}[\lambda]$. Moments of this phase space density function correspond to expectation values of symmetrically ordered operator products,

$$\left\langle \left\{\hat{\psi}^r(\hat{\psi}^\dagger)^s\right\}_{sym}\right\rangle = \int \mathrm{d}^2\psi\ \psi^r\,(\psi^*)^s\,W(\psi, \psi^*). \tag{4.18}$$

One can show that a W-function exists for any density matrix [67]. Using the definition of the characteristic function it is possible to relate this function to the other representations like for example the P-function [84]:

$$W(\psi, \psi^*) = \frac{2}{\pi}e^{-2|\psi|^2}\int \mathrm{d}\beta\mathrm{d}\beta^\dagger\ P(\beta, \beta^\dagger)\exp\left(2\psi^*\beta + 2\psi\beta^\dagger - 2\beta\beta^\dagger\right). \tag{4.19}$$

A few examples of W-functions of important states are considered in Fig. 4.1.

- From the density operator for a pure coherent state $\hat{\rho} = |\lambda\rangle\langle\lambda|$ it follows that

$$W_c(\psi, \psi^*) = \frac{2}{\pi}\exp\left(-2|\psi - \lambda|^2\right). \tag{4.20}$$

The shape of a coherent state in phase space does not change from the vacuum $|0\rangle$, but is simply a displacement to a new complex mean value λ. Coherent states are fully isotropic in phase space, i.e. they have the same uncertainty in X and P.

- A thermal state, $\hat{\rho}_T = \left(1 - e^{-\beta\hbar\omega}\right) \sum_n |n\rangle \langle n| e^{-n\beta\hbar\omega}$, corresponds to a similar Wigner function ($\beta = 1/kT$) [67]

$$W_T(\psi, \psi^*) = \frac{2}{\pi} \tanh(\beta\hbar\omega/2) \exp\left[-2|\psi|^2 \tanh(\beta\hbar\omega/2)\right]. \tag{4.21}$$

  Although it retains the phase symmetry, the function is more spread out due to the addition of thermal fluctuations on top of the vacuum fluctuations. The limit $T \to 0$ recovers (4.20) for $\lambda = 0$, the vacuum.

- From the thermal state Wigner function an expression can be derived for the Fock number state $|n\rangle$. An example for $|n = 3\rangle$ is plotted in Fig. 4.1(c) showing the highly non-classical nature of these states. Although this distribution is still circularly symmetric, it oscillates radially and has regions of negative probability.

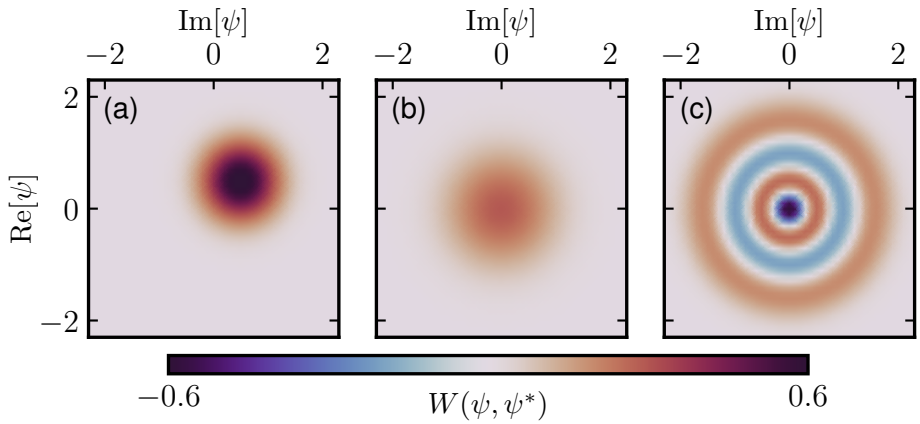

Figure 4.1 – Wigner representations of common quantum states like a coherent state $|\lambda = 1/2 + i/2\rangle$ (a), a thermal state at temperature $\beta\omega = 1$ (b) and the Fock state $|n = 3\rangle$ (c).

4.3.4 Truncated Wigner approximation

A straightforward proof demonstrates that a Wigner function exists for any density operator [67]. In addition, it is possible to express the evolution of the Wigner

function in time under the effect of the system Hamiltonian in the same way that the master equation quantifies this for the density matrix. An equivalent differential equation governing the W-function can be derived from a master equation by applying a set of *operator correspondences*. These relations are given by [67, 81]

$$\begin{aligned}
\hat{\psi}_j\hat{\rho} &\leftrightarrow \left(\psi_j + \frac{1}{2}\frac{\partial}{\partial\psi_j^*}\right) W(\Psi,\Psi^*), \quad \hat{\psi}_j^\dagger\hat{\rho} \leftrightarrow \left(\psi_j^* - \frac{1}{2}\frac{\partial}{\partial\psi_j}\right) W(\Psi,\Psi^*), \\
\hat{\rho}\hat{\psi}_j &\leftrightarrow \left(\psi_j - \frac{1}{2}\frac{\partial}{\partial\psi_j^*}\right) W(\Psi,\Psi^*), \quad \hat{\rho}\hat{\psi}_j^\dagger \leftrightarrow \left(\psi_j^* + \frac{1}{2}\frac{\partial}{\partial\psi_j}\right) W(\Psi,\Psi^*),
\end{aligned} \tag{4.22}$$

for a multimode bosonic system where $\Psi = (\psi_1, \ldots, \psi_L)^T$ is the vector of complex phase space variables. The Wigner function is then defined as

$$W(\Psi,\Psi^*) = \int \frac{\mathrm{d}^{2L}\boldsymbol{\lambda}}{\pi^{2L}} \exp\left(\boldsymbol{\lambda}^\dagger\Psi - \boldsymbol{\lambda}\Psi^\dagger\right) \chi_W(\boldsymbol{\lambda},\boldsymbol{\lambda}^*). \tag{4.23}$$

Taking the Bose-Hubbard model (2.19) as an example, from the von Neumann master equation then follows the PDE

$$\begin{aligned}
\hbar\frac{\partial W(\Psi,\Psi^*,t)}{\partial t} = &-\sum_j^L \left[\frac{\partial}{\partial\psi_j}\mathcal{F}_j + \frac{\partial}{\partial\psi_j^*}\mathcal{F}_j^*\right] W(\Psi,\Psi^*,t) \\
&+ \frac{iU}{4}\sum_j^L \frac{\partial^2}{\partial\psi_j\partial\psi_j^*}\left[\frac{\partial}{\partial\psi_j^*}\psi^* - \frac{\partial}{\partial\psi_j}\psi_j\right] W(\Psi,\Psi^*,t).
\end{aligned} \tag{4.24}$$

for the Wigner quasi-probability function. The drift term

$$\mathcal{F}_j = i\left[J(\psi_{j+1} + \psi_{j-1}) - V_j - U(|\psi_j|^2 - 1)\psi_j\right] \tag{4.25}$$

is associated with the deterministic *mean-field* time evolution. This is where a powerful tool central to this approach emerges. Equation (4.24) in its current condition is quite difficult to solve. Things can be simplified when the terms containing third order derivatives are left out of the equation. Fortunately, these terms scale as $\propto UN^{-1}$ and can at first be neglected in the weakly-interacting, large mode occupation limit. This is exactly the *Truncated Wigner Approximation* (TWA). In this case, (4.24) reduces to a multivariate Fokker-Planck equation, here without diffusion term. Crucial here is that if the initial distribution is strictly positive valued and can be described by a Fokker-Planck equation, it can equivalently be

described by a set of differential equations [85]

$$\hbar \mathrm{d}\psi_j = \mathcal{F}_j \mathrm{d}t. \tag{4.26}$$

Quantum fluctuations are contained in this approach in the sampling of the phase-space variables from the initial Wigner distribution. Moments of the W-function, which can now be interpreted as a true probability function, correspond to averages over the deterministically time evolved phase space variables, denoted by the subscript W. Taking into account the symmetrization we find for example for the density

$$\langle |\psi_j|^2 \rangle_W \equiv \langle \{\hat{\psi}_j^\dagger \hat{\psi}_j\}_{sym} \rangle = \langle \hat{n} \rangle + \frac{1}{2}. \tag{4.27}$$

One can see here that even in the vacuum, where $\langle \hat{n} \rangle = 0$, each mode of the system has a half particle occupation, the vacuum noise, due to the finite variance on complex phase space variables.

We conclude this section with a couple of important remarks. The TWA is extremely useful in that one can rely upon concepts of classical noise theory to access quantum mechanical time evolution. Nevertheless, it remains an approximation and as a consequence excludes negative Wigner functions, like superpositions of Fock states or cat states[2], that arise for certain processes. We cannot easily sample an initial W-function with regions of negative probability and due to the absence of third order derivatives in Eq. (4.24) any positive function will never become negative. It should be noted that these phenomena are very rare in the case of weakly interacting BECs. Lastly, the interpretation of TWA results deserves a small remark. Technically, only large ensemble averages of stochastic quantities can be compared with the corresponding correlation functions obtained through experimental measurements. It is however not surprising that single noisy trajectories bear great resemblance to single experimental realisations. In the same way that the GPE is a good predictor of the classical limit of a quantum evolution, each Wigner trajectory seems to correspond to one plausible outcome of the given experiment at least for highly occupied fields.

[2]Cat states are superpositions of macroscopically different coherent states [79]. A modest example is the linear superposition of two coherent states with opposing phases, $|cat\rangle \sim |\lambda\rangle + |-\lambda\rangle$.

4.4 Projected c-field methods

In Chapters 7 and 8 of this thesis we will consider two- and three-dimensional BEC configurations. With rapidly growing system sizes the limiting factor for numerical simulations of these systems will be the computational cost. Unraveling the time evolution, even at the lowest order, can become demanding in higher-dimensional settings. In the most obvious approach, one can consider a discrete spatial grid of equidistant points on which to evaluate Eq. (4.1). The box, with sizes L_ν in the dimensions $\nu = x, y, z$ and a total volume $V = \prod_\nu L_\nu$, contains $\mathcal{N} = \prod_\nu N_\nu$ grid points. For this discrete grid to be a good representation of reality, some requirements should be fulfilled. Naturally, the step size in each direction should be smaller than the physical scales, i.e. the healing length ξ or the de Broglie wavelength λ_T. The lower bound, on the other hand, is set by the s-wave scattering length a_s, leaving room for a wide range of grid spacings. Naturally, we want to minimise the number of grid points, to reduce computational cost, without compromising the accuracy of our calculations. The projected c-field methods provide a framework that further relaxes the requirement put on the energy cut-off E_{max}, directly related to the smallest length scale included in simulations.

4.4.1 Projected Gross-Pitaevskii equation

Central to these approaches is the subdivision of low-energy subspace, set by assuming an effective contact interaction (2.8), into two more regions. A distinction is made between a delimited coherent or c-field region, containing not only the condensate, but all highly degenerate modes, and the incoherent region consisting of the remaining, sparsely occupied modes. This is made clear in the schematic view in Fig. 4.2, for a harmonically trapped system. While all individual modes in the incoherent region are sparsely occupied, the overall occupation of this region can still be significant, depending on the temperature. Nevertheless, their influence on the coherent dynamics remains small so that their exact evolution can often be disregarded. The idea of introducing a cut-off to the coherent region represented by the GPE was first coined in 2001 by Davis *et al.* [86] and clearly reviewed in Ref. [81]. We use these and other references [87–90] to summarize the projected c-field methods in this section.

The split between coherent and incoherent region is implemented by means of the

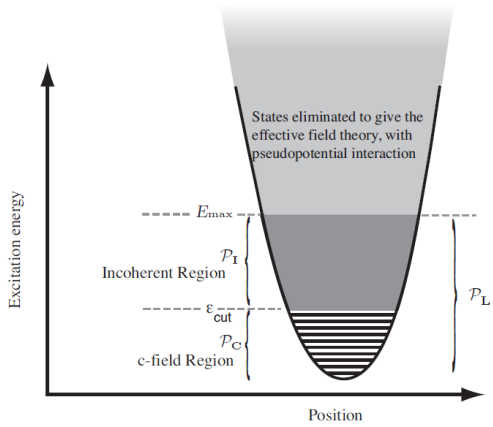

Figure 4.2 – Delimitation of the low-energy subspace $\mathbf{L}$ in a harmonic trap energy landscape, and further subdivision into an incoherent region $\mathcal{I}$, and a coherent region $\mathcal{C}$. Generally, only the latter requires a microscopic description using classical fields. Figure reproduced from Ref. [81].

projection operators $\mathcal{P}_\mathcal{C}$ and $\mathcal{P}_\mathcal{I}$, which are defined as

$$\mathcal{P}_\mathcal{C}\left[F(\mathbf{r})\right] = \sum_{n\in\mathcal{C}} \phi_n(\mathbf{r}) \int \mathrm{d}^3\mathbf{r}'\ \phi_n^*(\mathbf{r}')F(\mathbf{r}'), \tag{4.28}$$

$$\mathcal{P}_\mathcal{I}\left[F(\mathbf{r})\right] = \hat{\mathbb{I}} - \mathcal{P}_\mathcal{C} = \sum_{n\notin\mathcal{C}} \phi_n(\mathbf{r}) \int \mathrm{d}^3\mathbf{r}'\ \phi_n^*(\mathbf{r}')F(\mathbf{r}'). \tag{4.29}$$

The coherent region $\mathcal{C}$ is the collection of all low-lying energy modes below a certain energy cut-off ϵ_{cut} and the set $\{\phi_n\}$ denotes the basis in which the single-particle Hamiltonian diagonalizes. We define respectively the coherent- and incoherent field operators

$$\hat{\psi}(\mathbf{r}) = \mathcal{P}_\mathcal{C}\left[\hat{\Psi}(\mathbf{r})\right] = \sum_{n\in C} \hat{a}_n\phi_n(\mathbf{r}) \quad \text{and} \quad \hat{\eta}(\mathbf{r}) = \mathcal{P}_\mathcal{I}\left[\hat{\Psi}(\mathbf{r})\right], \tag{4.30}$$

that together make up the original field operator

$$\hat{\Psi}(\mathbf{r}) = \left(\mathcal{P}_\mathcal{C} + \mathcal{P}_\mathcal{I}\right)\hat{\Psi}(\mathbf{r}) = \hat{\psi}(\mathbf{r}) + \hat{\eta}(\mathbf{r}). \tag{4.31}$$

The cut-off for the coherent region is determined by the requirement[3] that $\langle \hat{a}_n^\dagger \hat{a}_n \rangle \gg 1$, meaning that the matter field for these modes will behave rather classically al-

[3]The coherent region may also contain modes of low occupation that are still crucial to the dynamics, as we will see later on.

lowing us to drop the operator character and write

$$\hat{\psi}(\mathbf{r}) \to \psi(\mathbf{r}) = \sum_{n \in C} c_n \phi_n. \tag{4.32}$$

The commutator of the coherent field operators is given by

$$\left[\hat{\psi}(\mathbf{r})\hat{\psi}^\dagger(\mathbf{r}')\right] = \delta_{\mathcal{C}}(\mathbf{r}, \mathbf{r}'), \tag{4.33}$$

where the kernel of the projection operator

$$\delta_{\mathcal{C}}(\mathbf{r}, \mathbf{r}') = \sum_{n \in \mathcal{C}} \phi_n(\mathbf{r}) \phi_n^*(\mathbf{r}') \tag{4.34}$$

acts as a Dirac-delta distribution for any function in the coherent region:

$$\psi(\mathbf{r}) = \int \mathrm{d}^3\mathbf{r}' \ \psi(\mathbf{r}')\delta_{\mathcal{C}}(\mathbf{r}, \mathbf{r}'). \tag{4.35}$$

Evolution in time of the coherent field is obtained by applying the projection operator $\mathcal{P}$ to the GPE (4.1). Neglecting interactions with the incoherent region entirely, the equation of motion (EOM) reduces to the so-called *projected* Gross-Pitaevskii equation (PGPE):

$$i\hbar \frac{\partial \psi(\mathbf{r}, t)}{\partial t} = \left[-\frac{\hbar^2}{2m}\nabla^2 + V(\mathbf{r}) \right] \psi(\mathbf{r}, t) + g\mathcal{P}\left\{ |\psi(\mathbf{r}, t)|^2 \psi(\mathbf{r}, t) \right\}. \tag{4.36}$$

The requirement for the inclusion of a certain mode ϕ_n in the coherent region is, as stated before, $|c_n|^2 > n_{cut}$, where the cut-off occupation is often of the order 1 to 10. However, when a system contains a large thermalized coherent region, an even larger incoherent region will be present whose effect will be significant. The PGPE cannot capture the full dynamics for an experiment with a Bose gas at some finite temperature. Yet, one can expect the equilibrium state of the microcanonical system, simulated by the PGPE, to be similar to that of the coherent region when it would still interact with $\mathcal{I}$. For sufficiently many degrees of freedom, fluctuations of energy and particle number of the grand canonical system will in fact be small [86–88].

4.4.2 Truncated Wigner formalism

In this work we will predominantly treat systems residing at temperatures well below the critical temperature, in which case even the coherent region will contain many lowly occupied modes. Although this means that the incoherent modes are more or less unoccupied and have no significant contribution, the effect of quantum fluctuations on the coherent fields is all the more important. In this case, an adaptation of the TWA to the projected c-field theory can bring salvation. The definition for the coherent Wigner function $W_{\mathcal{C}}(\boldsymbol{\psi}, \boldsymbol{\psi}^*)$ is the same as in Eq. (4.23) for a system with L modes in the coherent region and a vector of mode amplitudes $\boldsymbol{\psi} = (c_1, c_2, \ldots, c_L)^T$. Given the definition in (4.32) one can find the expectation value for the field density to be

$$\int \mathrm{d}^{2L}\boldsymbol{\psi}\ |\psi(\mathbf{r})|^2 W_{\mathcal{C}}(\boldsymbol{\psi}, \boldsymbol{\psi}^*) = \langle \hat{\psi}^\dagger(\mathbf{r})\hat{\psi}(\mathbf{r})\rangle + \frac{\delta_{\mathcal{C}}(\mathbf{r}, \mathbf{r})}{2}, \tag{4.37}$$

which immediately indicates why a cut-off had to be introduced. Half a quantum is added to each mode in $\mathcal{C}$ to mimic quantum fluctuations, but this would lead to an ultraviolet divergence if all physically possible modes would be included in the theory. Projection involves only a finite number of modes, making the second term a well-defined addition.

Similarly as before, the von Neumann equation for the density matrix of the coherent region,

$$i\hbar \frac{\partial \hat{\rho}_{\mathcal{C}}}{\partial t} = \left[\hat{H}_{\mathcal{C}}, \hat{\rho}_{\mathcal{C}}\right], \tag{4.38}$$

can be mapped onto a time evolution equation for $W_{\mathcal{C}}$. This does require a slightly different set of operator correspondences that implement projected functional derivatives [91]. To maintain the overview we do not list them here, but instead jump straight to the Langevin-type equations that follow in the truncated Wigner approximation [81]:

$$i\hbar \frac{\partial \psi(\mathbf{r}, t)}{\partial t} = H_{sp}\psi(\mathbf{r}, t) + \mathcal{P}\left\{ g\left[|\psi(\mathbf{r}, t)|^2 - \delta_{\mathcal{C}}(\mathbf{r}, \mathbf{r})\right]\psi(\mathbf{r}, t)\right\}. \tag{4.39}$$

Here, $H_{sp} = -\hbar^2\nabla^2/2m + V(\mathbf{r})$ is the single-particle part of the Hamiltonian. Treating this multimode system is intuitively not much different from the L coupled modes of the Bose-Hubbard system in the TWA (see Sec.4.3.4), apart from the interactions which couple each single-particle mode to all the others. A detailed explanation on how to evaluate the matrix elements of the non-linear

interaction term for a harmonically trapped system can be found in Appendix A.

4.4.3 Finite temperature

Eqs. (4.36) and (4.39) are approximate descriptions of the coherent field evolution. In all generality, the EOM still contains cross-terms that couple to the incoherent field [86]:

$$\begin{aligned} i\hbar\frac{\partial\psi(\mathbf{r})}{\partial t} = H_{sp}\psi + g\mathcal{P}\left\{|\psi|^2\psi\right\} + g\mathcal{P}\left\{2|\psi|^2\langle\hat{\eta}\rangle + \psi^2\langle\hat{\eta}^\dagger\rangle\right\} \\ + g\mathcal{P}\left\{\psi^*\langle\hat{\eta}\hat{\eta}\rangle + 2\psi\langle\hat{\eta}^\dagger\hat{\eta}\rangle + \langle\hat{\eta}^\dagger\hat{\eta}\hat{\eta}\rangle\right\}. \end{aligned} \tag{4.40}$$

This equation describes the exact evolution of the coherent field and is referred to as the finite temperature projected Gross-Pitaevskii equation (FTPGPE). It gives a more complete picture, but is rather complicated to implement numerically and goes beyond the scope of this work. A detailed account on the FTPGPE is found in Ref. [87]. When the region $\mathcal{C}$ is large, at temperatures $T \approx T_c$, fluctuations in total particle number and energy due to the cross-terms will be small and a description of the coherent region as a microcanonical system is justified.

4.4.4 Spectral basis

This brings us to a last important point, the choice of the single-particle basis. Care should be taken that the numerical representation of all basis modes brings about a faithful representation of the physics that one aims to describe. In practice, modelling is performed by numerically solving the time evolution of the mode amplitudes in the coherent region:

$$i\hbar\frac{\mathrm{d}c_n}{\mathrm{d}t} = \epsilon_n c_n + gF_n \tag{4.41}$$

with the eigenenergies $\epsilon_n < \epsilon_{cut}$. The difficulty now lies in the evaluation of the matrix element of the interaction, defined as

$$F_n \equiv \int \mathrm{d}^3\mathbf{r}\ \phi_n(\mathbf{r})|\psi(\mathbf{r})|^2\psi(\mathbf{r}), \tag{4.42}$$

which requires the transformation of the spectral field to a quadrature grid in real space. For a homogeneous Bose gas for example, where an expansion in plane waves is appropriate and commonly used, the cubic interaction can lead to

momenta up to three times larger than those included in the coherent field. An accurate portrayal of the coherent region therefore not only requires the explicit application of the projection operator, but also to retain sufficiently many points in the quadrature grid above the cut-off energy to insure that the non-linear elements are evaluated exactly for the states in the coherent region [81, 89, 92, 93].

Using a grid method based on plane wave basis states, that bear little resemblance to the harmonic oscillator modes, to model a trapped gas is extremely challenging. Even the optimal plane-wave representation $L_\nu = \sqrt{2\pi\hbar N_\nu/m\omega_\nu}$, which has a cut-off consistent in real and momentum space, will include inaccurate high energy modes displaying anomalous dynamics [92]. Fig. 4.3 displays the difference between the phase space covered by the optimal plane-wave and the harmonic basis. A classical particle in a 1D harmonic trap generally describes circular trajectories in momentum-position space. A circular projector is therefore deemed ideal. Although the optimal plane-wave basis covers nearly the same region, it also inaccurately incorporates high-energy modes. The point A in Fig. 4.3 should cover a clockwise trajectory, but instead seemingly iterates counter-clockwise through the points A-D due to running into the edges of the plane-wave projected region. Moving further away from the optimal plane-wave basis, even more modes will potentially suffer this anomalous evolution. Using a plane-wave basis for the PGPE is expected to result in an inconsistent representation of these corner regions, leading to effects like *Umklapp scattering*. Additionally, a plane-wave basis requires a much finer quadrature grid to determine matrix elements in (4.42) accurately. In Appendix A we provide a detailed outline of the efficient numerical scheme based on an expansion in harmonic oscillator states.

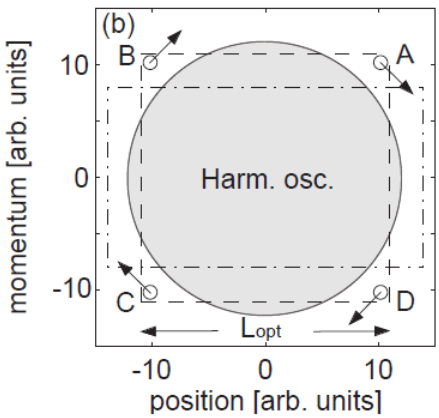

Figure 4.3 – Phase space coverage by an optimal plane wave (dashed), a sub-optimal plane-wave basis (dash-dotted) and harmonic oscillator basis (shaded). Figure adopted from Ref. [92].

4.5 Other approaches

The overview of theoretical methods in this chapter was limited to those relevant that will be of use later on in this thesis. A much larger list of exact and approximate methods to treat (open) quantum many-body systems exist in the literature. We shortly mention a few related techniques here.

Exact solution exists for several models, mostly for discrete lattice systems [61, 94–99]. Any Hamiltonian (or Liouvillian for an open system) can - in theory - be written in matrix representation and solved through numerically **exact diagonalization** by means of different software packages. This approach is limited, however, to small system sizes given the quadratic scaling d^2 of the computational costs with the already exponentially increasing Hilbert space dimensionality d.

Avoiding the need to time evolve the full density matrix of size d^2 are the **quantum trajectory** approaches in which dissipative dynamics is unravelled through the stochastic realizations of pure states - of size d only - in which the density matrix can be decomposed [100–103]. In return, large samples have to be gathered for small statistical errors. Any real gain is only obtained when this sample size is smaller than the size of the Hilbert space. It is a powerful method that mimics the continuous measurement of the system, but, despite the reduction, computational complexity remains a bottleneck for these numerically exact trajectory methods. Because the expansion of the density matrix in pure states is not unique, different

unravelings are possible relating to different measurement schemes. We emphasize the difference with the classical trajectories in the TWA, which occur in phase space rather than Hilbert space. Because phase space dimensionality increases only polynomially it has a computational advantage, which comes at the expense of getting only approximate solutions.

A long-established class of techniques in the study of closed quantum systems are the **variational methods**, both for determining ground-state properties as well as tracking the dynamics in a time-dependent variational principle. In general, the state of the system is limited to a region in Hilbert space and indicated by a set of variational parameters found through optimization. More recently, variational methods have been successfully applied to open systems where, instead of the system energy, the norm of the full master equation is minimized in search of an approximate steady state [104–106]. Approaches to study open quantum system are more often than not combinations of different approaches. Interesting works on systems somewhat related to those that form the subject of this work for example focus on variational quantum trajectories [107–109].

Part II

Dissipative first-order phase transition

CHAPTER 5

The single-mode non-linear resonator

The dynamics of a quantum many-body system significantly changes when one incorporates environmental interactions, revealing a range of novel phenomena that are typically inaccessible in closed systems. Of particular interest are properties of the steady states, which arise from the balance between an engineered drive and dissipation in open systems, as well as the relaxation towards these states. At the centre of this work are dissipative atomic systems, for which most features are highly tunable, including often also the connection to the environment. However, a lot more studies have been performed in the context of optical systems that are inherently lossy and generally require the inclusion of the environment in their theory. One particular phenomenon, initially studied in a quantum optical setting, is that of the first-order driven-dissipative phase transition. Because of its relevance to our results in the following chapters, we discuss this property here in its original setting.

There exists now a vast body of theoretical studies detailing the emergence of such phase transitions in a plethora of systems including but not limited to spin models [63, 110–112], photonic systems [94, 113–115], polariton condensates [116] and superconducting cavities [117]. Related to the physics of dissipative phase transitions are phenomena such as hysteresis [118] and critical scaling [116]. This chapter contains an overview of these concepts in an out-of-equilibrium setting based on the description of a paradigmatic model, the single-mode non-linear resonator. This minimal model for a dissipative phase transition has been studied

extensively over the past decades and is therefore a suitable benchmark for future results.

5.1 Single-mode optical cavity

Consider a single-mode, weakly interacting bosonic field, inherently lossy and subject to an external coherent drive. The Hamiltonian governing the unitary dynamics is then given by

$$\hat{H} = \hbar\omega_c \hat{a}^\dagger \hat{a} + \frac{U}{2}\hat{a}^{\dagger 2}\hat{a}^2 + \left[F e^{-i\omega_d t}\hat{a}^\dagger + h.c.\right], \tag{5.1}$$

whereas the single-particle losses can be well described in the Born-Markov approximation by means of the Lindblad master equation,

$$i\hbar\frac{\mathrm{d}}{\mathrm{d}t}\hat{\rho} = \left[\hat{H}, \hat{\rho}\right] + i\frac{\gamma}{2}\left(2\hat{a}\hat{\rho}\hat{a}^\dagger - \hat{a}^\dagger\hat{a}\hat{\rho} - \hat{\rho}\hat{a}^\dagger\hat{a}\right). \tag{5.2}$$

Here, the operator $\hat{a}^\dagger$ ($\hat{a}$) creates (annihilates) a bosonic excitation in the cavity with mode frequency ω_c, while U quantifies the interaction strength and F the intensity of the driving at a frequency ω_d. The dissipation rate, the average rate at which photons are lost from the cavity, is given by γ. A more convenient frame of reference is the one rotating with the driving frequency. Transforming to this frame removes the explicit time dependence of the driving term and introduces $\Delta\omega = \omega_d - \omega_c$, the frequency detuning between the cavity and the drive.

This generic model characterizes a class of systems that exhibit hysteresis around a critical point. It can be obtained for example for semiconductor micropillars driven by a laser [119–121] as well as in a circuit QED context [122, 123]. Analytic expressions for the out-of-equilibrium steady states in the classical limit together with a fully quantum mechanical treatment were discovered by Drummond and Walls [61]. To this end, it is convenient to introduce the scaling parameter $\tilde{N}$ so that

$$\tilde{U} = U\tilde{N}, \quad \tilde{F} = F/\sqrt{\tilde{N}}. \tag{5.3}$$

This parameter does not correspond exactly to the particle number, but is of the same order of magnitude. As such, a well-defined, *zero-dimensional* thermodynamic limit exists for $\tilde{N} \to \infty$, that keeps $\tilde{U}\tilde{F}^2$ constant. It is reflective of a system's spatial size going to infinity while keeping the chemical potential fixed. In this limit quantum fluctuations on top of the mean-field dynamics become in-

significant (see later) and the system behaves classically.

5.2 Mean-field analysis

The mean-field equation of motion for $\psi \equiv \langle \hat{a} \rangle$ is obtained from Eq. (5.2) by assuming all expectation values of operator products factorise:

$$i\hbar \frac{\mathrm{d}}{\mathrm{d}t}\tilde{\psi} = \left(-\hbar\Delta\omega + \tilde{U}|\tilde{\psi}|^2 - i\frac{\gamma}{2}\right)\tilde{\psi} + \tilde{F}, \tag{5.4}$$

where $\tilde{\psi} = \psi/\sqrt{\tilde{N}}$ is the rescaled field amplitude. Notice that this GP-like equation is invariant under scaling by $\tilde{N}$ and depends, for a given loss rate and detuning only on the value $\tilde{U}\tilde{F}^2 = UF^2$.

For the system to be in a steady state, the phase has to be locked to the driving frequency and as such the stationary solution of Eq. (5.4) should be of the form $\tilde{\psi} = \sqrt{n}e^{i\phi}$, where n and ϕ are constants in time. Substitution in the differential equation leads to equations for the rescaled steady-state density [53, 61],

$$n\left[\left(\tilde{U}n - \hbar\Delta\omega\right)^2 + \frac{\gamma^2}{4}\right] = \tilde{F}^2, \tag{5.5}$$

and the phase lag,

$$\phi = \arctan\left(\frac{\gamma/2}{\tilde{U}n - \hbar\Delta\omega}\right) + \pi\Theta\left(\hbar\Delta\omega - \tilde{U}n\right). \tag{5.6}$$

Real and positive roots of the former give the steady-state densities that together with the phase rotation frequency and the phase lag, obtained from the latter, amount to the full solution. Critical points in the cubic function for n, given by

$$n_\pm = \frac{2 \pm \sqrt{1 - 3\gamma^2/4\Delta\omega^2}}{3\tilde{U}}\Delta\omega, \tag{5.7}$$

delineate the boundaries of the region where three solutions exist. When $\gamma > 2\Delta\omega/\sqrt{3}$ these values become complex, meaning Eq. (5.5) will have only one real root. Straightforward application of the stability analysis outlined in Sec. 4.2 tells us that only two of the three solutions in the finite range $\tilde{F}_+ \equiv \tilde{F}(n_+) < \tilde{F} < \tilde{F}_- \equiv \tilde{F}(n_-)$ are stable. Steady-state filling levels can be divided in a stable upper and lower branch, indicated by the full lines in Fig. 5.1(a), and an unstable middle branch, marked by the dashed lines. As a result, the system is bistable in

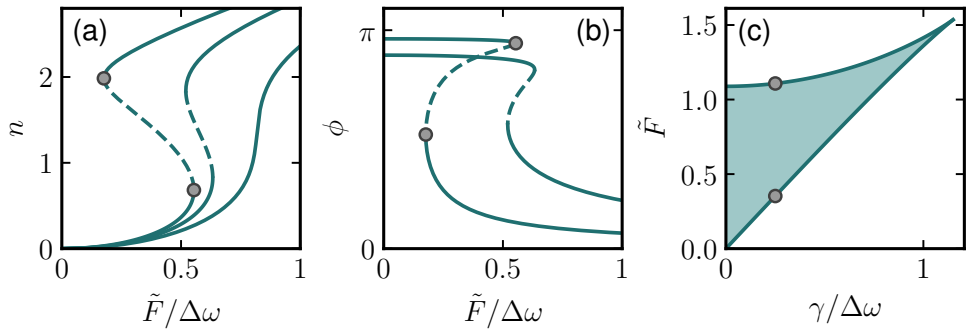

Figure 5.1 – Steady state solutions for the driven-dissipative single-mode resonator with interaction strength $\tilde{U} = 1.0$ and frequency detuning $\Delta\omega = 0.5$. (a) Rescaled photon density in function of the driving amplitude for different loss rates. The curves correspond from left to right to $\gamma/\Delta\omega = 0.25, 0.75, 1.25$. Dashed lines indicate dynamically unstable solutions. (b) Phase lag against $\tilde{F}$ for the two lowest values of γ plotted in (a) for which bistability occurs. The upper branches close to π correlate to the low density phase. (c) Phase diagram in $\tilde{F}(\gamma)$-space. The bistability region (shaded) is bounded by the turning points in the cubic equation (5.5). The dots indicate the same critical points in all three figures for the specific value of $\gamma/\Delta\omega = 0.25$.

the mean-field limit and exhibits hysteresis when varying the driving amplitude. Starting at a small driving amplitude and gradually increasing $\tilde{F}$ the filling level will remain on the lower branch until the critical point n_- is reached. A sudden jump to the upper branch, the only possible steady state, will then be observed. Subsequent decrease of the driving strength will not immediately lead to a reverse switch down, but rather a decrease of the filling level along the upper branch in Fig. 5.1(a). At the second critical point, n_+, density will suddenly drop, closing the hysteresis loop.

The full phase diagram in $\tilde{F}$-γ space is shown in Fig. 5.1(c). Interestingly, the range of values for the driving for which the system is bistable is maximal at $\gamma = 0$, with the bistable phase persisting down to $\tilde{F} = 0$. With increasing dissipation the bistability region shrinks, finally closing at the critical point $\gamma_c/\Delta\omega = 2/\sqrt{3}$. At the cusp, the two stable branches merge into one continuous solution $\tilde{\psi}(\tilde{F})$.

5.3 Exact quantum-mechanical solution

The bistability predicted in the mean-field approximation is apparently in contradiction with the uniqueness of the quantum state and all observables (like particle

number) derived from it. A full quantum mechanical treatment of the Lindblad master equation in (5.2) quickly brings clarification. In the regime of mean-field bistability the exact steady-state solution reveals a bimodal structure, i.e. the true state is a statistical mixture with probabilities of observing different densities clustered around the mean-field stable predictions. It is the lack of thermal or quantum fluctuations in the mean-field approach that made these solutions[1] come across as stable. The approach for solving Eq. (5.2), set out in Ref. [61], is based on the transformation to the equivalent complex P-representation. The ensuing Fokker-Planck equation is exactly solvable for the steady-state quasi-probability function. Alternatively, the solution for the quasi-probability distribution can be converted to a Wigner function, resulting in the relatively elegant expression [84]

$$W[\psi,\psi^*;F] = Ae^{-2|\psi|^2}\left|\frac{J_{s-1}\left(\sqrt{-16\psi^* F/U}\right)}{(\psi^*)^{(s-1)/2}}\right|, \tag{5.8}$$

where A is a normalization constant, $s = -2(\Delta\omega + i\gamma/2)/U$ and $J_\nu(z)$ is the Bessel function of the first kind. These expressions, because they are positive valued over the whole phase space, resemble actual probability functions and allow for explicit, interpretable phase space pictures. The second panel in Fig. 5.2 for example clearly illustrates the bimodal character. Outside the bimodal region the statistics becomes similar to the classical limit, i.e. a single peak around the only stable mean-field solution. The exact quantum state thus forms an interpolation between the two steady-states by gradually converting the statistical weight from one solution to the other.

This is reflected in the observable properties of the system as well. From the steady-state P-function an analytic expression for the normally ordered operator moments has been derived [61, 84]:

$$\langle \hat{a}^{\dagger m}\hat{a}^m\rangle = \left|\frac{2F}{U}\right|^{2m}\frac{\Gamma(s)\Gamma(s^*)\,{}_0F_2\left(m+s, m+s^*, 8\left|\frac{F}{U}\right|^2\right)}{\Gamma(m+s)\Gamma(m+s^*)\,{}_0F_2\left(s, s^*, 8\left|\frac{F}{U}\right|^2\right)}, \tag{5.9}$$

with ${}_0F_2$ the hypergeometric function defined as

$${}_0F_2(c,d,z) = \sum_{n=0}^{\infty}\frac{\Gamma(c)\Gamma(d)}{\Gamma(c+n)\Gamma(d+n)}\frac{z^n}{n!}. \tag{5.10}$$

[1] In the framework of the Liouvillian spectral theory discussed in Chapter 3, the mean-field solutions are the *extreme metastable states*.

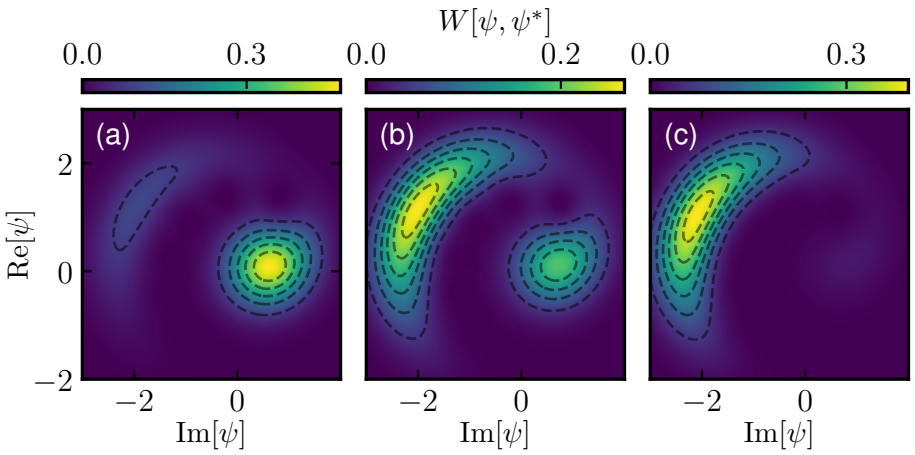

Figure 5.2 – Examples of the exact steady state solutions of the Lindblad master equation (5.2) represented in Wigner phase space. The plots show the solution at $\tilde{F}/\Delta = 0.40,\ 0.44$ and 0.50 respectively with $\gamma/\Delta\omega = 0.25$, $\tilde{U}/\Delta\omega = 0.5$ and $\tilde{N} = 2$.

The uniqueness of the stationary state is evident from the plots of the rescaled photon density $n = \langle \hat{a}^\dagger \hat{a} \rangle / \tilde{N}$ and the second order correlation function $g^{(2)} = \langle \hat{a}^{\dagger 2} \hat{a}^2 \rangle / n$ in Fig. 5.3. For small values of $\tilde{N}$ the transition from low to high photon density is smooth. In the crossover regime the system probes two regions in phase space resulting in a wide peak in $g^{(2)}$, i.e. large fluctuations. With a growing scaling parameter an increase in the sharpness of the transition can be seen, while at the same time the width of the peak in Fig. 5.3(b) decreases. The region where the Wigner function is bimodal shrinks. Consequently, in the thermodynamic limit $\tilde{N} \to \infty$ the transition is a discontinuous jump at a single point, the critical point $\tilde{F}_c$, indicative of a first-order phase transition.

Attributed to the bimodality is a typical switching of observable values between the two mean-field predictions driven by fluctuations. This can be observed in individual experiments or single numerical simulations of the time evolution that include quantum- or thermal fluctuations [120, 121, 124]. The switching rate quantifies the characteristic relaxation time, set by the Liouvillian gap, that undergoes a critical slowing down towards the transition point. Moving away from this transition point, one of the two branches becomes increasingly stable at the cost of the other becoming more unstable. It is exactly this divergence of the relaxation time around the phase transition that gives rise to hysteric behaviour. In the thermodynamic limit, equivalent to the limit of large photon numbers, the Wigner

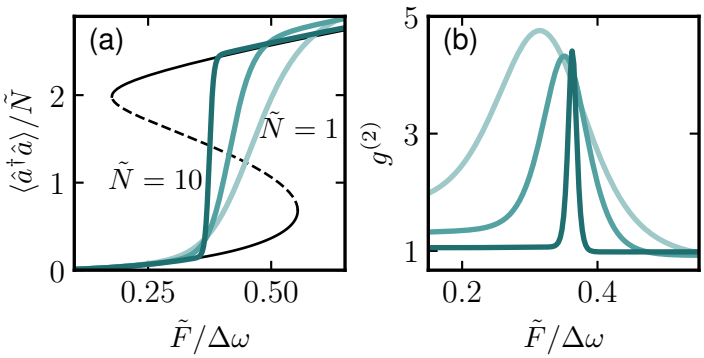

FIGURE 5.3 – Properties of the unique steady-state density matrix. Dependence of the average rescaled density (a) and the second order correlation function $g^{(2)}$ (b) on the rescaled driving amplitude are shown for $\gamma = 0.5$, $\tilde{U} = 2\gamma$ and $\Delta\omega = 4\gamma$. The rescaling parameter $\tilde{N}$ is varied. From light to dark $\tilde{N} = 1, 2, 10$. The density is compared to the mean-field prediction (black lines).

function becomes single peaked for all values of the driving amplitude, except at the critical point where it features two peaks with equal weights. In this limit the effect of fluctuations becomes negligible resulting in extremely long relaxation times compared to the natural time scales of the problem, i.e. when initialized in one of the two (meta)stable states, the other region in phase space will only be probed at very late times. The mean-field picture can thus be reconciled with the unique steady state in the sense that for large occupations and at finite times the system will exhibit *apparent* bistability.

5.4 Cavity lattices

Recent advancements have allowed also the experimental consideration of spatially extended systems in the available platforms, which in turn has driven theoretical advancements. Originally, ultracold atomic gases were the preferred candidates to experimentally validate the celebrated Bose-Hubbard model (see Sec.2.2.2), but for quite a while now this physics has also been within the reach of optical systems. Conventional platforms include semiconductor microcavities [125–129], circuit QED architectures [130–132] and photonic crystal nanocavities [133, 134]. The minimal model, the Bose-Hubbard dimer, consists of only two lossy coupled resonators, which, despite its apparent simplicity, supports a wide range of additional non-linear phenomena. Under symmetric excitation results are qualitatively

the same as for the single dissipative resonator [124, 135], but asymmetric driving in combination with the possibility for self-trapping allows for a more elaborate mean-field phase diagram [103, 114, 128]. Larger driven-dissipative lattices in one and two spatial dimensions have been widely studied as well [108, 136–140]. The Bose-Hubbard phase diagram with its typical Mott-insulator lobes is drastically altered due to the combination with the single resonator bistability. In the next chapter, we treat a hybrid version that still features Bose-Hubbard dynamics and (localized) single-particle losses, but lacking the external coherent drive typical for laser driven optical systems.

CHAPTER 6

Dissipative Bose-Hubbard array

The majority of the results presented in this chapter were peer reviewed and published as [141]:

Nonequilibrium steady states and critical slowing down in the dissipative Bose-Hubbard model
R. Ceulemans & M. Wouters, Physical Review A, 108, 013314 (2024)

Contrary to photonic systems, ultracold atom configurations are typically extremely well isolated from environmental interactions. Intrinsic losses from three-body recombination can often be neglected over experimentally relevant timescales. As a result, continuous replenishment of particles is in most cases unnecessary, and the relative importance of any externally engineered dissipation over Hamiltonian dynamics can be more finely tuned.

In the following chapters, we will explore the physics of a dissipative Josephson array, a spatially extended superfluid configuration which is treated as perfectly isolated apart from an engineered localized loss process at its centre. Interest for this particular system has grown over the past decade, following a series of experiments where it was realized using an elongated atomic BEC loaded into a

unidirectional optical lattice [47, 48, 50, 51]. In this setup, a focused electron beam introduces loss to a single site in the lattice at a rate γ, adjusted via the beam's intensity. The surrounding sites, unaffected by the beam, act as a reservoir by providing refilling particle currents. Notably, this system features only losses without compensating driving, meaning that in the true steady state as $t \to \infty$, the system becomes trivially empty. However, for sufficiently large arrays, quasi-stationary states can persist for extended periods of time [48, 50]. Signatures of a first-order dissipative phase transition have been observed experimentally and are investigated from a theory point of view in this and the following chapters.

Although the multimode nature of each site is essential for any quantitative comparison with experiments, this chapter simplifies the description to an array of coupled single-mode cavities. Having reviewed the physics of the single-mode driven-dissipative resonator in the previous chapter, we now break down the properties in the BHM with loss. We thus begin by focusing on the longitudinal dynamics before considering the effect of the system's transverse extent in Chapter 7.

6.1 Bistability in the mean-field approximation

Unitary dynamics of the closed system is governed by the Bose-Hubbard Hamiltonian, detailed in Sec. 2.2. The process of individual particles *leaking* or being kicked out is best modelled through the Lindlbad master equation (3.6) with jump operators

$$\hat{\Gamma}_j = \sqrt{\gamma_j}\hat{a}_j \tag{6.1}$$

that annihilate a single particle from the j-th site. We are specifically interested in the situation where the average loss rate is zero for all loss channels except for one, $\gamma_j = \gamma\delta_{j,0}$.

Typically, quantum fluctuations play an important role in 1D systems [82, 142–144]. An appropriate treatment of the master equation, taking into account fluctuations, is therefore given in Sec. 6.3. Nonetheless, we know from analysing the single-mode resonator that for weak interactions and large particle numbers the main features can already be understood within the classical limit. In the mean-field approach, dynamics of the dissipative BHM is represented by a set of coupled differential equations for the complex amplitudes $\psi_j \equiv \langle \hat{a}_j \rangle$. Transforming to the

frame rotating with $\mu_R/\hbar$, the initial chemical potential, results in

$$i\hbar\frac{\mathrm{d}\psi_j}{\mathrm{d}t} = -J\left(\psi_{j-1}+\psi_{j+1}\right) + \left[U|\psi_j|^2 - \mu_R - i\frac{\hbar\gamma_j}{2}\right]\psi_j. \tag{6.2}$$

Remarkably, the mode that is subject to losses ($j = 0$), satisfies Eq. (5.4) exactly, with a driving term $F(t) = -J[\psi_{-1}(t) + \psi_1(t)]$. It is effectively a driven-dissipative single-mode resonator, but with a more complex pumping mechanism that is subject to back-reaction. Amplitude and phase of the driving term are directly coupled to ψ_0 itself. Given this resemblance, one can expect similar phenomena as for the Kerr cavity. Indeed, the central mode occupation will relax to a nonequilibrium steady state (NESS), similar to the optical cavity. Large sequences of highly occupied sites will constitute a continuous flow of particles from both sides to compete with the losses at the centre, as becomes clear in Fig. 6.1(a). Starting from a fully coherent array with large particle occupation, set by the chemical potential ($n_j \equiv |\psi_j|^2 = \mu_R/U$), a density dip is quickly formed around the dissipation. While the depth remains fixed for long times, the width increases with time, indicating the loss of atoms from the reservoirs.

The rate of change in particle number of the lossy site is given by

$$\frac{\mathrm{d}n_0}{\mathrm{d}t} = I_0(t) - \gamma n_0(t) \tag{6.3}$$

with the incoming current given by

$$I_j(t) = \frac{2J}{\hbar}\left[\sqrt{n_j n_{j-1}}\sin(\Delta\theta_{j,j-1}) + \sqrt{n_j n_{j+1}}\sin(\Delta\theta_{j,j+1})\right], \tag{6.4}$$

found by applying the Madelung transformation $\psi_j = \sqrt{n_j}e^{i\theta_j}$ and taking $\Delta\theta_{i,j} \equiv \theta_i - \theta_j$. It is clear from (6.3) and (6.4) that besides the trivial empty steady state, $\psi_j = 0$, the model also supports a stationary solution with equal fillings and a fixed phase difference $\Delta\theta = |\theta_j - \theta_{j+1}|$ between neighbouring sites that satisfies

$$\sin\Delta\theta = \frac{\hbar\gamma}{4J}. \tag{6.5}$$

The predicted critical point that follows here, $J_{sf}/\hbar = \gamma/4$, indicates the breakdown of superfluid flow and is consistent with the single-mode resonator. Below this critical point, incoming currents can not account for the losses causing the relative occupation n_0/n_R to equilibrate close to zero, as shown by the dashed lines in Fig. 6.1(c). A large population imbalance between the lossy site and the

reservoirs persists indefinitely. Because the occupation in the centre is close to zero, but does not vanish completely, the total rate of particles being lost from the system is very small. Above J_{sf}, the setup can support large particle currents that drive the relative occupation in the lossy well closer to one. However, in the vicinity of this critical point $J \gtrsim J_{sf}$, a large initial population difference with the reservoirs can still be sustained due to the Josephson self-trapping effect. The prohibition of superfluid currents over a Josephson junction was described earlier in Sec. 2.2.4. Full lines in Fig. 6.1(b) and (c) depict the dependence on the initial condition in this regime.

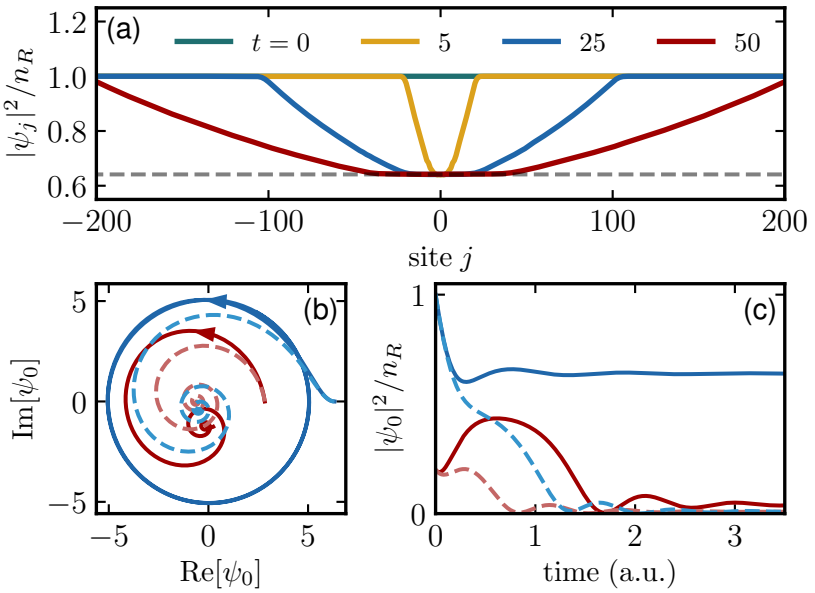

Figure 6.1 – Relaxation towards the NESS in the mean-field approximation. (a) Rescaled spatial density profile at different times after a sudden quench of the loss rate $0 \to \gamma$. Time evolution started from a completely uniform array with $J/\hbar = 0.85$. (b) Relaxation of the dissipative mode visualised in phase space for $J/\hbar = 0.85$ (full) and $J/\hbar = 0.45$ (dashed). The NESS that is reached not only depends on the value of the tunnelling amplitude, but also on the initial filling fraction $\psi_0(0) = \sqrt{f_0 n_R}$ of the lossy site. We compare for the same tunnelling strengths the evolution when $f_0 = 1.0$(blue) and $f_0 = 0.2$(red). The arrows indicate the direction of evolution in phase space in the frame rotating with frequency $\mu_R/\hbar$. (c) The same time evolution as in (b) depicted by the rescaled density of the central well. The remaining system parameters are $U/\hbar = 0.25$, $\gamma = 3.0$ and $\mu_R/\hbar = 10$.

6.1.1 Mean-field phase diagram

There clearly exists a region where the system displays bistability in its out-of-equilibrium steady states, analogous to the single-mode model [61] as well as to experimental measurements at short evolution times [48]. Ensuing hysteresis in the NESS is illustrated in Fig. 6.2(a), where we show the rescaled occupation of the lossy site for a range of values of the tunnelling strength at a fixed loss rate. For a given set of parameters the array is initialized in a fully coherent, uniform state, set by the chemical potential μ_R, except for the central well where the starting occupation is varied. The central well either has the same occupation as the reservoir sites (full) or is nearly completely depleted (empty). This is in correspondence with the experimental protocol in Refs. [48, 50, 51]. Before the start of each measurement the system is kept at a much higher lattice potential, effectively decoupling all the sites ($J \to 0$), whilst one site is depleted using the electron beam. Subsequent ramping down of the potential to the desired value for J signals the start of a measurement[1].

At zero tunnelling, all sites are decoupled and the dissipation will simply empty the central well on a timescale of the order γ^{-1}. In contrast, when the tunnelling is very large, particle currents easily compensate for losses, resulting in a high steady state occupation. At intermediate tunnelling rates, the occupation depends on the system's history. Starting from a central site with only a few atoms, the large interaction energy difference between the central site and its first neighbour inhibits large particle currents in the same way as in the self-trapping regime of the bosonic Josephson junction [33, 145–147]. Reservoirs on both sides of the dissipative system remain mostly undepleted. Conversely, starting from a central site with an occupation similar to its neighbours, driving is close to resonance, and the relative occupation remains closes to one. In this regime the reservoirs are drained more rapidly. Fig. 6.2(b) shows plots of the phase lag $\Delta\theta = |\theta_0 - \theta_{\pm 1}|$ against tunnelling, emphasizing the qualitative resemblance to the driven-dissipative single-mode resonator. Notably, the lower lines, representing the superfluid branch, align precisely with Eq. (6.5).

An overview of the steady-states in J-γ parameter space is represented in Fig. 6.2(c). The full non-equilibrium phase diagram is obtained by numerically determining

[1] It was shown in Ref. [56] that the dephasing of the individual sites relative to each other during the hold time has a significant impact on the short-time dynamics. In this chapter, we will assume for simplicity that coherence is quickly restored and does not influence the steady-state properties. We start all simulations with two fully phase coherent reservoirs. Furhter on, in Chapter 8, we will study the dependence on relative phase in more detail.

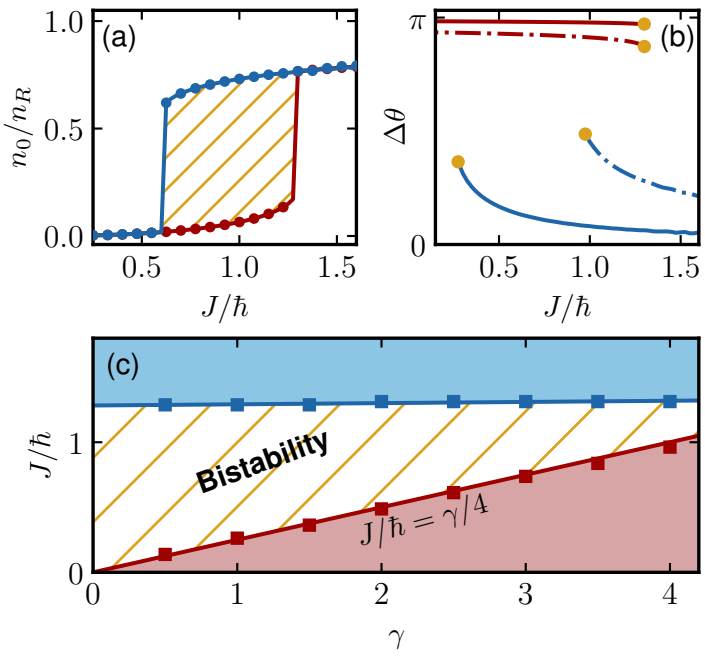

Figure 6.2 – Mean-field bistability in the open Bose-Hubbard array. (a) Steady-state filling level of the central well in function of the tunnelling for initial filling fraction 0.05 (red) or 1.0 (blue). (b) Steady-state phase difference $\Delta\theta = |\theta_0 - \theta_1|$ in function of J for $\gamma = 1$ (full lines) and $\gamma = 4$ (interrupted). The bottom curves follow relation (6.5) exactly. (c) $J - \gamma$ phase diagram indicating the parameter regions of low occupation (red), bistability (hatched) and unity filling (blue) in the steady states. It is derived by numerically determining the boundaries of the hysteresis loop for different values of γ.

the boundaries in Fig. 6.2(a). In the upper region, the central well evolves to a steady-state with relative occupation close to one, regardless of the initial state. In the bottom right region the steady-state occupation is always small. Similar to the driven-dissipative optical resonator, the region of mean-field bistability, denoted by the hatched area in the phase diagram, is maximal for $\gamma = 0$. With increasing dissipation this area shrinks and eventually closes in a bifurcation point as well. The lower threshold of the bistable region is linear with γ, in analogy with the optical system. Although an extensive quantitative comparison of the experiment with the 1D BHM is of little significance, the difference at this lower boundary is still remarkable. The linear relation was also recovered experimentally in Ref. [48], but with a much steeper slope $J/\hbar = \gamma$.

6.1.2 Instability of the lower branch

So far, driving of the dissipative system from the two reservoirs, the left and right half-chains, has been identical and the above analysis also rests on this assumption. However, this does not necessarily need to be satisfied. In addition to the two symmetric solutions with large and small occupations of the lossy site described above, a third antisymmetric state of the system can be reached. It is characterized by a π phase difference between the two reservoirs, leading to perfect destructive interference of the two tunnelling currents. As a result, density in the lossy system drops to exactly zero. Because the density in the centre vanishes, dynamics is no longer affected by the dissipative part, and it is, at least in the classical limit, a dark state of the Liouvillian. Particles are no longer lost from the system, despite a finite γ. Moreover, a formal stability analysis shows that the steady-states on the lower branch of Fig. 6.2(a) are actually unstable. A small perturbation is sufficient to destroy phase coherence between the left and right reservoirs and drive the system to the dark state, as demonstrated in Fig. 6.3. It displays the phase of each site evolving in time, while the system resides in an NESS on the lower branch. A slight perturbation is applied at time t_p in the form of a site-dependent multiplicative phase $e^{i\pi\times 0.01\xi_j}$, where ξ_j are normally distributed with unit variance. This very small excitation makes the system collapse to the dark state after some transient dynamics.

It might be clear already that the dark state described here is a stationary dark soliton, a specific instance of a family of excited states, ubiquitous in non-linear systems [148–154], including a range of cold atoms setups [155–158]. We will come back to this phase and study its properties and the effect on the phase diagram in greater detail in Chapter 8. Up until now, the instability of the lower branch towards the dark soliton state has not been observed experimentally. In the remainder of this chapter we therefore assume our system to be symmetric with respect to the dissipative site, effectively disregarding the soliton state.

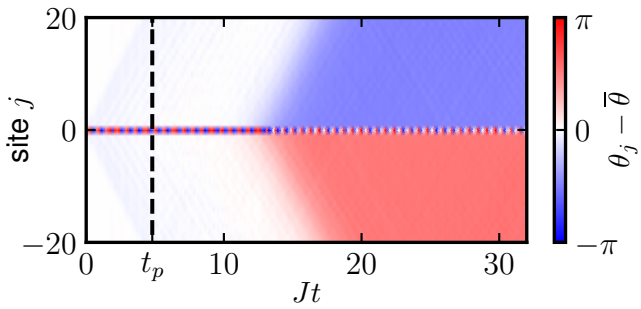

Figure 6.3 – A small perturbation of the NESS on the lower branch leads to a runaway effect. The minor excitation at t_p leads to internal dynamics that eventually cause the build-up of a π phase difference over the lossy site that extends outwards. The system leaves the metastable state and relaxes to soliton state. Here, $\bar{\theta}$ is the average phase over all sites at a given time.

6.2 Effective description

Reeves & Davis [53] pioneered the theoretical characterization of the experimental setup within a (semi-)classical field description. Because the experimentally relevant three-dimensional system is numerically quite involved, they reduced the modelling to merely a few lattice sites while keeping the full two-dimensional structure in the transverse direction, demonstrating the qualitative analogy with a resonantly driven non-linear optical cavity [61]. A detailed understanding of the validity of this reduced description is, however, lacking in their work. We aim to close this gap by considering the complementary 1D BHM. Based on the mean-field results from the previous section, we compare here the capability of the single-mode approximation, introduced in Chapter 5, to grasp the full 1D lattice physics, as well as propose our own model.

6.2.1 Single-mode approximation

Particle occupation in the lossy well stabilizes when the total incoming current is exactly equal to the rate of particles lost from this well due to dissipation. A common approach to approximate the dynamics of the full array assumes the reservoir modes to be undepleted indefinitely, i.e. $\psi_{\pm 1}(t) = \sqrt{n_R}\exp(-i\mu_R t/\hbar)$ [51, 53]. Substitution in (6.2) reduces the set of L equations to only one that

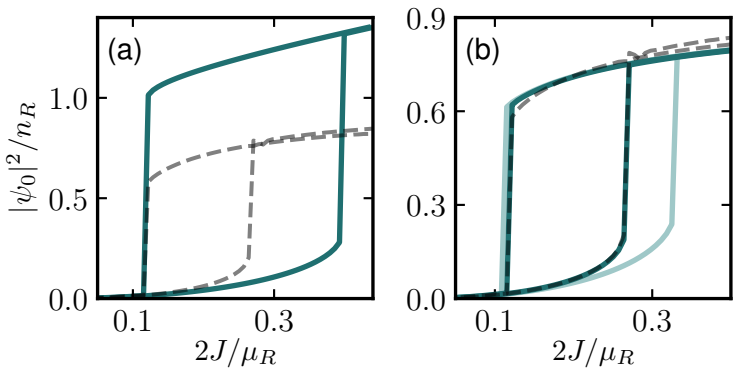

Figure 6.4 – Quantitative comparison of the steady states obtained from the dissipative BHM with those from the single-mode approximation (a), and the incoherently driven models (b) with $L = 3$ (light) and $L = 5$ (dark) coupled modes. The curves show the relative filling level during an adiabatic sweep of the tunnelling strength $J = \tilde{F}/2$ at a fixed loss rate $\gamma/\mu_R = 0.2$.

is given exactly by Eq. (5.4), with $F = 2J\sqrt{n_R}$ and driving frequency[2] $\omega_d = \mu_R/\hbar = Un_R/\hbar$ [7]. While there is a good correspondence with the full lattice model at the qualitative level, there are significant quantitative differences in the shape of the hysteresis, as illustrated in Fig. 6.4(a). The most salient discrepancies are the overestimation of the upper bistability threshold and the density on the upper branch. The latter, the so-called *overfilling*, unphysically predicts a *larger* occupation on the dissipative site in comparison to the neighbouring reservoir sites. Furthermore, fixing the driving phases also excludes the possibility to form of a soliton.

It is clear that this approximation of the reservoirs does not hold, because with it we formally break their $U(1)$-symmetry which is otherwise retained. Simulating the reservoir modes according to Eq.(6.2) allows spontaneous phase dynamics to take place and includes back-action from the open system on the internal reservoir, which leads to more complex dynamics altering the properties discussed in the previous chapter.

[2]The frequency and amplitude of the drive are inherently linked, contrasting the optical system from the previous chapter.

6.2.2 Incoherently pumped

We propose a different effective model that provides a more accurate description of the dissipative Bose-Hubbard lattice and still reduces the computational cost by multiple orders of magnitude. This model is inspired by the mean-field description of exciton-polariton condensates, in which the losses are compensated by incoherent pumping from a dynamic reservoir [62, 125]. The coherent Josephson couplings of the lossy site with the nearest neighbours are crucial given that it is the self-trapping effect that seeds the hysteresis. However, couplings between reservoir modes all operate in the linear tunnelling regime allowing us to approximate the contribution from further away modes by a single driving term. In order to maintain the $U(1)$-symmetry of the reservoirs, we model them as incoherent pumping baths, which corresponds physically to injecting particles in the fluid with random phases.

The smallest possible configuration is a Bose-Hubbard trimer ($L = 3$), schematically represented in Fig. 6.5(a), with losses on the central mode and reservoir modes that satisfy

$$i\hbar\frac{\mathrm{d}\psi_{\pm1}}{\mathrm{d}t} = -J\left(\psi_0 - \psi_{\pm1}\right) + U|\psi_{\pm1}|^2\psi_{\pm1} + i\frac{\kappa}{2}\left[1 - \frac{|\psi_{\pm1}|^2}{n_R}\right]\psi_{\pm1}. \tag{6.6}$$

Here, κ is the rate of saturation, simulating refilling from a large number of highly occupied wells with mean occupation n_R. On-site tunnelling in this equations simply shifts the ground-state energy. Focusing briefly on the incoherent gain term, we can write the current injected from the reservoir as

$$I^+(t) = \frac{\mathrm{d}n^+(t)}{\mathrm{d}t} = \kappa\left[1 - \frac{n^+}{n_R}\right]n^+. \tag{6.7}$$

Given some initial particle number $n_0 \equiv n(t = 0)$, the evolution in time follows a *logistic function*

$$n^+(t) = \frac{n_0 n_R}{n_R e^{-\kappa t} + n_0\left(1 - e^{-\kappa t}\right)}. \tag{6.8}$$

This signature s-shape, evident from the plots in Fig. 6.5(b), has been observed in previous experimental [47] as well as theoretical works [54–56] on the refilling of a localized density dip in a Josephson array without active loss process. The logistic curve has been identified empirically as the best fit for the refilling, hence our choice to model the reservoirs in this way.

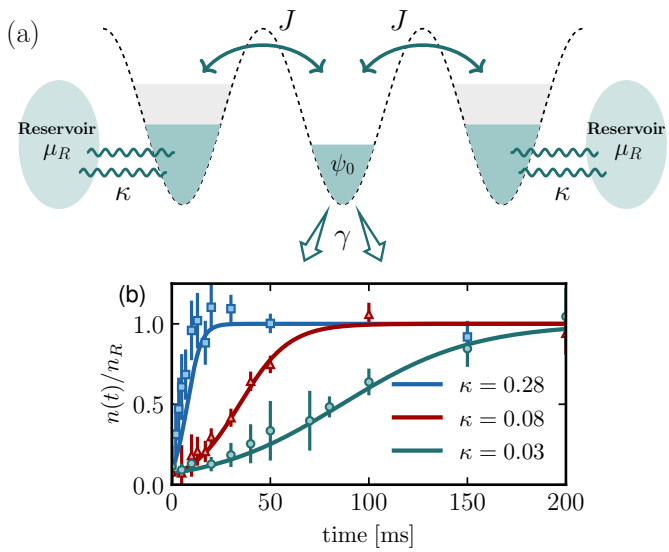

Figure 6.5 – (a) Schematic representation of the Bose-Hubbard trimer with incoherent driving at the outer sites. While μ_R and κ determine the saturation level and mean growth rate, an effective temperature T_{eff} is associated with the incoming current to account for fluctuations. (b) Refilling of a single depleted site in a closed Josephson array. Measurements of the density in this site, from Ref. [47], are empirically fitted with the logistic function of Eq. (6.8).

Steady-state densities of the dissipative mode are compared to the solutions from the full lattice in Fig. 6.4(b). It is clear that our proposed description outperforms the single-mode approximation. Most significant is the similarity in the filling levels of the upper branch which for the toy model depend mainly on the value of κ. The lower branch is less affected by variations in the saturation rate. Even better agreement with the benchmark is obtained by slightly increasing the size. Considering now $L = 5$ coupled modes, with the first and last again saturated as specified in Eq. (6.6), the resulting NESS's show overall excellent quantitative agreement with the benchmark. We illustrate this for a single value of γ in Fig. 6.4(b), but the comparison holds for the entire J-γ parameter space. It should be emphasized this model requires no fitting parameters. The choice for the rate of refilling κ, driven by superfluid transport in a Josephson array, naturally follows from the definition of the speed of sound $\kappa = \sqrt{2JUn_R}$. This model enables us to probe the mean-field properties of a dissipative Bose-Hubbard array with much less computational effort, and with the added benefit that steady-states are not restricted in time.

6.3 Quantum fluctuations

The mean-field approximation, while sufficient to understand the seemingly bistable nature in the classical limit, fails to capture quantum fluctuations on top of the mean-field dynamics. To capture these, we apply the TWA to the array of L coherently coupled modes. The EOM for the Wigner distribution $W[\Psi, \Psi^*]$ over $2L$-dimensional phase space, parametrized by the coherent-state amplitudes $\Psi = (\psi_1, \psi_2, ..., \psi_L)$, is derived from the master equation by way of the operator correspondences (4.22):

$$\begin{aligned}\frac{\partial W(\Psi, \Psi^*, t)}{\partial t} = -\sum_j \Bigg\{ \frac{\partial}{\partial \psi_j} \Big[iJ/\hbar(\psi_{j+1} + \psi_{j-1}) + U/\hbar(|\psi_j|^2 - 1)\psi_j \\ - \frac{\gamma_j}{2}\psi_j \Big] + c.c. \Bigg\} W + \sum_j \frac{\gamma_j}{2} \frac{\partial^2}{\partial \psi_j \partial \psi_j^*} W,\end{aligned} \tag{6.9}$$

where we have already neglected third order derivatives. Connection to an environment leads to a non-zero diagonal diffusion matrix in the Fokker-Planck equation, $\mathbf{D}_{ij} = \frac{1}{2}\sum_k \sigma_{ik}\sigma^*_{jk}$, where $\sigma_{ij} = \sqrt{\gamma_j/2}\delta_{ij}$. This diffusion term can be mapped onto an additional stochastic term in the Langevin equations [67]:

$$i\hbar \frac{\mathrm{d}\psi_j}{\mathrm{d}t} = -J\left(\psi_{j+1} + \psi_{j-1}\right) + U\left(|\psi_j|^2 - 1\right)\psi_j - i\frac{\hbar\gamma_j}{2}\psi_j + \sqrt{\frac{\gamma_j}{2}}\xi_j(t). \tag{6.10}$$

The term $-U\psi_j$ leads to a global phase shift that does not impact number conserving observables and can therefore safely be neglected. Given an appropriate initial Wigner function W_0 (read positive everywhere), determining its time evolution can again be done equivalently through sampling of W_0 and subsequent unravelling of the stochastic evolution. Quantum fluctuations still enter the dynamics due to the nondeterministic nature of the initial conditions, but additional dynamical noise is included, associated with the environment interaction. Here, $\xi_j(t)$ is a complex Gaussian variable, for which the following relation holds:

$$\langle \xi_j(t) \rangle = 0, \quad \langle \xi_i(t)\xi_j^*(t') \rangle = \delta_{ij}\delta(t - t'). \tag{6.11}$$

Note that this stochastic differential equation is no longer invariant under rescaling $\psi_j \to \sqrt{n_R}\tilde{\psi}_j$:

$$i\hbar \frac{\mathrm{d}\tilde{\psi}_j}{\mathrm{d}t} = -J\left(\tilde{\psi}_{j+1} + \tilde{\psi}_{j-1}\right) + \tilde{U}\left|\tilde{\psi}_j\right|^2\tilde{\psi}_j - i\frac{\gamma_j}{2}\tilde{\psi}_j + \sqrt{\frac{\gamma_j}{2n_R}}\xi_j(t) \tag{6.12}$$

As we discussed already in the previous chapter, the particle occupation is a good measure of the *classicality*. As n_R increases the effect of fluctuations compared to the mean-field value becomes smaller, reducing quantum effects overall. The fact that the stochastic term in (6.12) vanishes for $n_R \to \infty$ and the regular GPE from Eq. (6.2) is recovered confirms that the TWA is consistent with this interpretation. We can distinguish the zero-dimensional thermodynamic limit of large particle occupation, obtained while keeping $\mu_R = U n_R$ fixed, from the traditional thermodynamic limit of the BHM that sees the system size go to infinity, $L \to \infty$. For all simulations performed in this work, L is chosen sufficiently large as to avoid boundary effects during simulated evolution times.

We assume that the initial state, as it is experimentally prepared, is well described by a direct-product state of coherent states:

$$|\Psi_{ini}\rangle = \bigotimes_j \exp\left\{\bar{\psi}_j \hat{a}_j^\dagger - \bar{\psi}_j^* \hat{a}_j\right\} |0\rangle \,. \tag{6.13}$$

The corresponding Wigner function is then given by

$$W_0\left(\Psi, \Psi^*\right) = \left(\frac{2}{\pi}\right)^L \prod_j \exp\left\{-2\left|\psi_j - \bar{\psi}_j\right|^2\right\}. \tag{6.14}$$

Starting values for all phase space variables ψ_j are drawn independently from the coherent state Wigner function, a complex normal distribution around $\bar{\psi}_j$. The values of $\bar{\psi}_j$ are set equal to the ground state values of the closed system obtained from imaginary time evolving Eq. (6.2) with $\gamma = 0$. The average occupation of the central well is varied between *full*, $\bar{\psi}_0 = \sqrt{n_R}$, and *empty*, corresponding to a filling fraction of 5%.

6.3.1 Bimodality

The main effect of including quantum fluctuations is most clearly depicted by individual stochastic realisations, displayed in Fig. 6.6(a) and (b). Short-time dynamics in each trajectory is still determined by the initial condition; density on the central well quickly gravitates towards one of the two mean-field solutions (dashed lines in Fig. 6.6) and remains quivering around this value. On a much longer timescale, jumps between the complementary states can be observed. Adding fluctuations changes the bistability to bimodality, i.e. the system probes two regions in phase space that are centred around the mean-field solutions. This reflects the

density matrix being a statistical mixture. It is due to the 1D approximation that the long evolution times where these switches become relevant and large system sizes L needed to observe them are computationally within reach.

We can interpret this behaviour also from the spectral theory of the Liouvillian; see Chapter 3. The clearly distinct timescales are due to a separation of eigenvalues in the Liouvillian spectrum, $|\mathrm{Re}[\lambda_2]| \gg \lambda \equiv |\mathrm{Re}[\lambda_1]|$. The short-time transient is then determined by $\tau' = 1/|\mathrm{Re}[\lambda_2]|$. At times $t \gg \tau'$ the density matrix is approximately given by

$$\hat{\rho}(t) = \hat{\rho}_{ss} + c_1\hat{\rho}_1 = p^+(t)\hat{\rho}^+ + p^-(t)\hat{\rho}^-, \tag{6.15}$$

with probabilities $p^+(t) + p^-(t) = 1$. The metastable state is a mixture of the *macrostates* $\hat{\rho}^+$ and $\hat{\rho}^-$, the states on the upper and lower branch of the mean-field analysis. They correspond to $c_1 = c_1^{\max}$ and $c_1 = c_1^{\min} \leq 0$ respectively, the minimal and maximal overlap of any initial state with $\hat{\rho}_1$. The remaining dynamics is a generator of classical stochastic dynamics [73], trajectories of quantum jumps between $\hat{\rho}^+$ and $\hat{\rho}^-$. In principle, only averages over large ensembles of Wigner trajectories correspond to quantum-mechanical expectation values of observables that would allow us to make comparisons with averages over experimental observations. However, due to the classic stochastic nature, the independent realisations already resemble individual experimental measurements of the system performed, for example, by Benary *et al.* [50]. This follows directly from the large occupations in this and other related experiments for which the classical limit is a good predictor, with the important addition of small fluctuations.

At times $t \gtrsim \tau = 1/\lambda$, the system will further relax to the stationary state

$$\hat{\rho}_{ss} = [c_1^{\max}\hat{\rho}^+ - c_1^{\min}\hat{\rho}^-]/\Delta c_1, \tag{6.16}$$

where $\Delta c_1 = c_1^{\max} - c_1^{\min}$. In the simulations presented in Fig. 6.6(a), the system was initialized very close to $\hat{\rho}^+$. Assuming the higher order coefficients $c_{i\geq 2}$ in the decomposition are small, we can say that at the beginning of the metastability window $p^+ = 1$. Consequently, time evolution of the statistical weights is given by [73]

$$\begin{aligned} p^+(t) &= \left(c_1^{\max} - c_1^{\min}e^{-t/\tau}\right)/\Delta c_1, \\ p^-(t) &= -c_1^{\min}\left(1 - e^{-t/\tau}\right)/\Delta c_1. \end{aligned} \tag{6.17}$$

Similar reasoning can be applied when we initialize the system close to $\hat{\rho}^-$, like in Fig. 6.6(b). Switches in individual trajectories signal the slow relaxation of the density matrix to its true stationary state. Analysing the switching statistics allows the derivation of the characteristic relaxation time scale τ. Temporal distributions of the time to a first transition for a large sample of $\mathcal{O}(10^4)$ trajectories showcase a distinctive exponential tail, as demonstrated in Fig. 6.6(c) and (d). From this we determine the characteristic switching times τ_{up} and τ_{down}. The time it takes the system to relax to its unique steady state, through the process of branch switching, is then characterized by $\tau^{-1} = \tau_{\mathrm{up}}^{-1} + \tau_{\mathrm{down}}^{-1}$. The distributions in Fig. 6.6(c) and (d) deviate from a purely exponential decay that one would expect for a uniform Poisson process, indicating that the jumps are not completely independent. At early times suppression of the branch switching occurs. This effect is more pronounced in panel (c) for switches from large to small occupation, indicating the presence of dynamics preceding such a transition.

6.3.2 Closing of the Liouvillian gap

With the tools to derive the Liouvillian gap, we can analyse how it changes in the regime of bistability. As expected, the observed hysteresis is the consequence of an underlying criticality. Slowing down of the relaxation time, i.e. exponential decay of $\lambda = \tau^{-1}$ towards a critical point J_c, is a consequence of a first-order dissipative phase transition at this point in the system's thermodynamic limit. In Fig. 6.7(a) the closing is quantified by a plot of λ/U as a function of the tunnelling strength in the regime where mean-field theory predicts bistability. One can observe the diverging relaxation time when the critical point is approached from below or above. While the particle number is large compared to the dynamic noise, $n_R = 40$, the minimum of the gap remains relatively large. The phase transition will be more rounded, i.e. transitioning through the region of mean-field bistability will gradually change the weights in the quasi-probability function from one peak to the other, like it was visualized in Fig. 4.1 of the previous chapter. This indicates that switches are not only induced by noise from the environment connection, but are also brought about by fluctuations in the driving mechanism. Each mode in the array is initialized with vacuum fluctuations that cannot leave the system except via the central, lossy site.

From the requirement for detailed balance in the steady state, $p^+/\tau_{\mathrm{down}} = p^-/\tau_{\mathrm{up}}$, we can determine the statistical weights p^+ and p^-, and therefore fully determine the steady-state density matrix. Fig. 6.7(b) nicely shows the gradual transition of

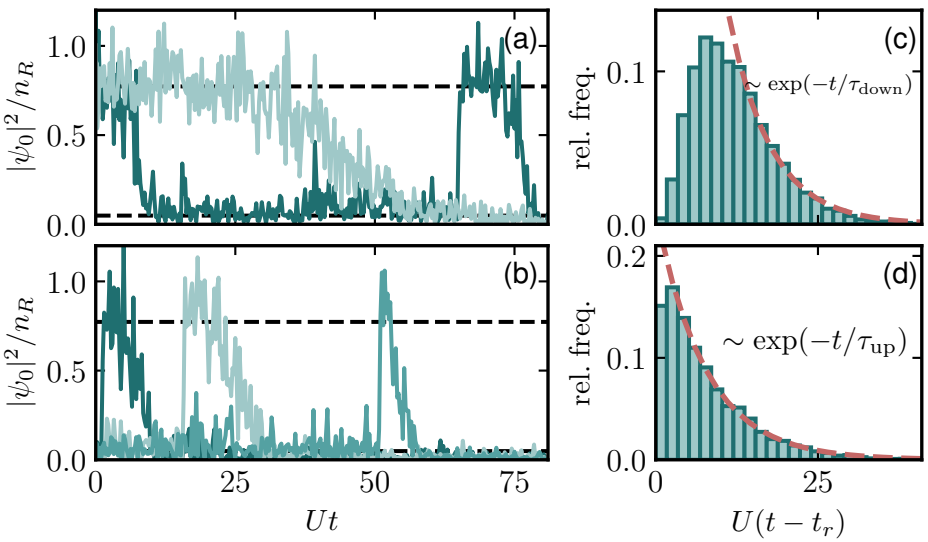

Figure 6.6 – Signatures of the bimodal character of the (quasi-)probability function. Examples of stochastic time evolution of the normalized central mode occupation starting *full* (a) or *empty* (b). Trajectories feature relatively long transients where the amplitude fluctuates around one of the steady states (dashed lines), with sudden jumps at seemingly random times. Temporal distributions of the first switch in a trajectory are shown in panel (c) and (d) for the same initial condition respectively. Tails of the distributions are fitted by an exponential (dashed lines). The short time t_r indicates the time for the system to relax to the metastable phase. System parameters for these trajectories are $J/\mu_R = 0.09$ and $\hbar\gamma/\mu_R = 0.2$.

the steady-state from $\hat{\rho} = \hat{\rho}^-$ to $\hat{\rho} = \hat{\rho}^+$. The predicted critical point for $\hbar\gamma/\mu_R = 0.2$, characterized by the state with equal probabilities, lies at $J_c/\mu_R \approx 0.091$. The minimum is derived from fitting a double exponential to the value of the Liouvillian gap, $\lambda(J) \sim Ae^{-\alpha J} + Be^{\beta J}$.

6.3.3 Thermal reservoir model

Deriving values for the Liouvillian gap close to the critical point requires very long simulation times and consequently large system sizes. In order to avoid finite size effects the maximum simulation time for a given system of size L is given by $t_{max} = L/\sqrt{2J\mu_R} = L/c_s$. These times and sizes are computationally feasible when dealing with the BHM, but become impossible to handle when we include also the transverse dynamics of each site [53, 55, 56]. It is here that our proposed effective model can bring salvation. Extending the description in Eq. (6.6) to the

TWA, we can describe a small array with the modes at the edges satisfying the stochastic differential equation

$$i\hbar\frac{\mathrm{d}\psi_j}{\mathrm{d}t} = -J\left(\psi_{j-1} - \psi_j\right) + U|\psi_j|^2\psi_j + i\Gamma_-(\psi_j)\psi_j + \sqrt{\Gamma^+(\psi_j)}\,\xi_j(t), \qquad (6.18)$$

where $\Gamma^{\pm}(\psi_j) = \kappa/2\left(1 \pm |\psi_j|^2/n_R\right)$. In the spatially smaller models, where $L = 3$ or $L = 5$, less noise originates from sampling the initial condition. Additionally, incoherent pumping at the edges will cause rapid damping of fluctuations in the system. Through the dynamic noise in the equation presented here we aim to account for these fluctuations that significantly impact the relaxation. Also shown in Fig. 6.7(a) is the closing of the gap, obtained with our effective description for $L = 5$ modes. The values $\lambda(J)$ slightly deviate from those for the BHM, indicating that the steady-state density matrix varies (see the second panel). The exponential decay is steeper resulting in a lower minimum for λ. In other words, the transition is less gradual as can also be observed in panel (b). With this the critical point slightly shifts, to $J/\mu_R \approx 0.087$. We can conclude that our effective description does not reproduce the exact same switching statistics as for the dissipative BHM, but contains all the properties to closely resemble it and is a major improvement on the laser-driving analogue.

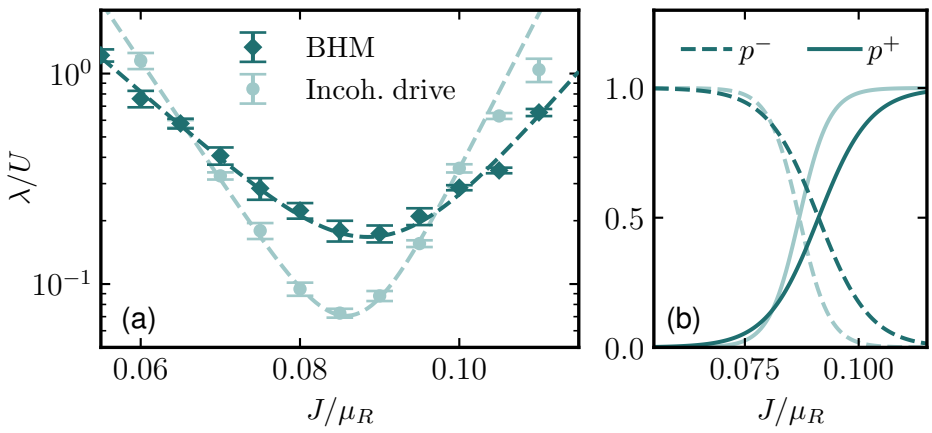

Figure 6.7 – (a) Closing of the Liouvillian gap (log scale) around the critical point indicates the presence of a first-order dissipative phase transition (in the thermodynamic limit). We compare the dissipative BHM with our proposed effective description. (b) From the relaxation rates the statistical weights of the bimodal mixture are determined. This clearly shows the transition in the density matrix from one macrostate to the other. Colours indicate the same model as in the left panel.

6.4 Multistability in binary mixtures

In the experiments on dissipative Josephson arrays [48, 50, 51], ultracold Rubidium-87 atoms were utilized, a common atomic species for BEC experiments. Not long after the first experimental realisation of a single-component Bose-Einstein condensate, concurrent condensation of ^{87}Rb atoms in two separate hyperfine states was achieved [159, 160]. Atoms in different hyperfine states are *distinguishable*, i.e. they should for all intents and purposes be regarded as different species. Interactions between particles in different hyperfine states in such a system, referred to as a binary mixture[3], give rise to a rich variety of phenomena. So as to not stray from the heart of the matter, we refer those seeking additional insights to some interesting reviews [12, 163]. Here, we limit the discussion to a proposal of an expansion on the current configuration using a binary mixture. Given the qualitative analogy with optical bistability, a natural continuation would be to leverage also spin properties to achieve *multistability*.

[3]Binary mixtures have also been realized with heteronuclear gases, where two different atomic species are simultaneously condensed, like for example a ^{41}K-^{87}Rb condensate [161, 162].

The two-component Bose-Hubbard model in it most general form is given by

$$\hat{H} = \sum_{\nu=1}^{2}\sum_{j=1}^{L}\left[-J_\nu\left(\hat{a}_{j,\nu}^\dagger \hat{a}_{j+1,\nu} + h.c.\right) + \frac{U_\nu}{2}\hat{n}_{j,\nu}(\hat{n}_{j,\nu}-1) - \mu_\nu \hat{n}_{j,\nu}\right] + U_{12}\sum_{j=1}^{L}\hat{n}_{j,1}\hat{n}_{j,2}. \tag{6.19}$$

Here, the operator $\hat{a}_{j,\nu}^\dagger$ ($\hat{a}_{j,\nu}$) creates (annihilates) a particles of species ν at the j-th site. The first part contains the single-species Hamiltonians, with component-dependent tunnelling J_ν, chemical potential and intraspecies interaction U_ν. We study the particular case where $U_1 = U_2 = U$ and $\mu_1 = \mu_2 = \mu/2$, but with different tunnelling strengths. Interspecies interactions, with a strength U_{12}, are represented by the second part, with $|U_{12}/U| < 1$ in order to avoid phase separation.

Inspired by spin multistability with microcavity polaritons [164], we suggest a novel manipulation scheme to realize this multivalued spin switching in the atomic configuration discussed above. To this end, we regard the spinor GPEs for the field amplitudes $\psi_{j,\nu} = \langle \hat{a}_{j,\nu}\rangle$

$$\begin{aligned} i\hbar\frac{\mathrm{d}\psi_{j,1}}{\mathrm{d}t} &= -J_1\left(\psi_{j-1,1}+\psi_{j+1,1}\right) + \left(U|\psi_{j,1}|^2 + U_{12}|\psi_{j,2}|^2 - \mu_1 - i\frac{\gamma_j}{2}\right)\psi_{j,1}, \\ i\hbar\frac{\mathrm{d}\psi_{j,2}}{\mathrm{d}t} &= -J_2\left(\psi_{j-1,2}+\psi_{j+1,2}\right) + \left(U|\psi_{j,2}|^2 + U_{12}|\psi_{j,1}|^2 - \mu_2 - i\frac{\gamma_j}{2}\right)\psi_{j,2}, \end{aligned} \tag{6.20}$$

where $\gamma_j = \gamma\delta_{j,0}$. Given a large number of reservoir modes with equal spin populations, *polarization* of the drive onto the lossy site can be adjusted by taking

$$J_1(\sigma_d) = J\frac{1+\sigma_d}{2},\ J_2(\sigma_d) = J\frac{1-\sigma_d}{2}. \tag{6.21}$$

Just like the single-component case, densities of both species in the central well equilibrate at different levels depending on the initial state. However, changing the polarization σ_d can significantly alter the typical bistability, in analogy with the polariton experiment in Ref. [164]. Fig. 6.8 shows the degree of polarization on the lossy site,

$$\Delta n_0 = \frac{|\psi_{0,1}|^2 - |\psi_{0,2}|^2}{|\psi_{0,1}|^2 + |\psi_{0,2}|^2}, \tag{6.22}$$

in the (quasi) steady-state as a function of the excitation polarization. Polarization is varied between $\sigma_d = -0.7$ and $\sigma_d = 0.7$ for two different initial conditions of

the lossy site $j = 0$. While each site starts with equal occupations of both species, particles in the central well at $t = 0$ are initially all from one species. At the lowest tunnelling strength studied here, $J/\hbar = 0.8$, a single hysteresis loop is observed. The local density switches from one species entirely to the other as the polarization varies. As J grows and the relative difference of the component dependent drive increases, the single loop breaks up into two distinct polarization hysteresis loops. The individual bistabilities for each component move away from each other, creating a middle stable branch. At $J/\hbar = 1.0$, when the loops still partially overlap, a region with three stable spin configurations is indicated by the shaded area. Technically, this corresponds to four steady-states, because of the two-fold degeneracy of the middle branch. The $\Delta n_0 = 0$ configuration can occur with both densities on their respective lower branch or both on the upper branch. Further increasing J, decreases this overlap and eventually leads to the separation of the two loops.

Although the expansion to this multicomponent version comes naturally from a theoretical point of view, and its potential within atomtronics for creating multi-valued logic gates is undoubted, it is certainly not trivial to show that this system can be realised experimentally. However, general techniques have been introduced that would allow experimentalists to induce and control spin-dependent tunnelling for two-state bosonic or fermionic atoms in optical lattices [165, 166].

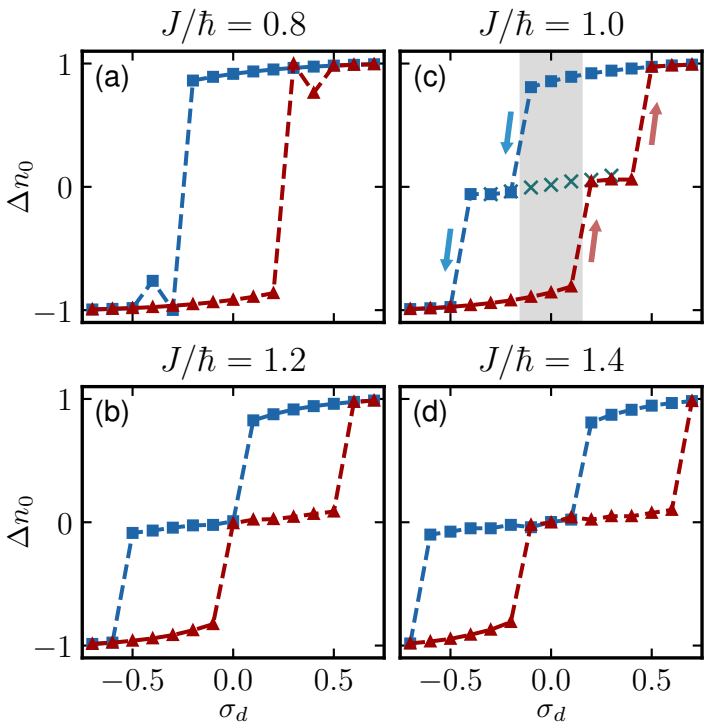

Figure 6.8 – Multistability in the two-component Bose-Hubbard model. Fractional density on the lossy site Δn_0 as a function of the drive polarization σ_d. The blue (red) points indicate the steady-state fraction after starting from $\Delta n_0 = 1$ ($\Delta n_0 = -1$). (a) A single hysteresis loop is observed at smaller tunnelling when the bistabilities of both components overlap. (b) With increasing J both loops disperse, creating a region of multistability (shaded). Steady-states indicated by the green crosses can be accessed by starting from the middle branch and scanning σ_d back and forth. (c),(d) Further increasing J eventually leads to two separate hysteresis loops for the two components.

6.5 Summary

In this chapter, we have studied a 1D Bose-Hubbard chain with single-particle losses at the central site, approximately representing the experiments in Refs.[48, 50, 51], using classical field methods. This model is able to capture the main features of interest on a qualitative level. First, properties of this system were studied on a mean-field level. Using these results a comparison was made with a compact effective description that replaces a large number of reservoir modes by a single saturation term, following recent efforts to reduce computational load for this system. Without the need for any fitted parameters, good quantitative agreement is obtained in the steady-state physics, thanks to its preservation of the $U(1)$-symmetry of the reservoir.

Bimodality of the steady states, observed on longer timescales, is studied using the truncated Wigner method. Switching between the metastable states is seen to be characterized by a critical slowing down towards a critical point, indicative of a first order phase transition in the thermodynamic limit. Through analysis of the switching statistics we derived the effective Liouvillian gap as a function of the tunnelling, showing that our effective description underestimates fluctuations.

Finally, we demonstrated the versatility of this configuration by briefly addressing the two-component version. An even richer phase diagram could be observed here due to the additional spin degree of freedom.

CHAPTER 7

Out-of-equilibrium condensation in driven-dissipative systems

Treating the condensate at each minimum in the optical lattice as effectively zero-dimensional, like we did in the previous chapter, allows a thorough analysis of the physics in the longitudinal, discrete direction. However, for a more complete picture and quantitative comparison to experimental results we should take into account the transverse degrees of freedom as well. Because the chemical potential in the experiments is much larger than the harmonic energy level spacing, the radial dynamics potentially plays an important role. It does become clear very quickly that this is a very demanding task. The processing power required for the simulations in this chapter is orders of magnitude larger, but is just within reach courtesy of the projected (semi-)classical field methods, detailed in Sec. 4.4.

In this chapter we will focus more on the nature of the phases in the mean-field bistability regime, paying special attention to the low-density state. Previous works [50, 53] classified the state on the lower branch as a thermal cloud, a *normal* state. We expect, however, that at low densities, where interactions play a less significant role, properties of the cloud in the central well are dominated by the coherent driving mechanism.

7.1 Multi-mode description

Unitary evolution of the Bose gas harmonically trapped in the x-y plane and subject to a 1D lattice potential in the z direction is governed by

$$\begin{aligned}\hat{H} = &\sum_j \left\{ \int \mathrm{d}^2\mathbf{r}\ \hat{\Psi}_j^\dagger \left[-\frac{\hbar^2}{2m}\boldsymbol{\nabla}_r^2 + \frac{m\omega_r^2}{2}\mathbf{r}^2 \right] \hat{\Psi}_j + \frac{g_{2\mathrm{D}}}{2} \int \mathrm{d}\mathbf{r}\ \hat{\Psi}_j^\dagger \hat{\Psi}_j^\dagger \hat{\Psi}_j \hat{\Psi}_j \right\} \\ &- J \sum_j \int \mathrm{d}^2\mathbf{r} \left(\hat{\Psi}_j^\dagger \hat{\Psi}_{j-1} + \hat{\Psi}_j^\dagger \hat{\Psi}_{j-1} \right),\end{aligned} \tag{7.1}$$

where integration is over the radial degrees of freedom $\mathbf{r} = (x, y)$ and $\hat{\Psi}_j \equiv \hat{\Psi}_j(\mathbf{r}, t)$. The effective 2D interaction strength is given by $g_{2\mathrm{D}} = g \int \mathrm{d}z |w_0(z)|^4$. It is assumed that the tight-binding approximation for the lattice direction, valid for sufficiently deep potentials, holds and that the tunnelling strength is given by (2.18). With the atom cloud in the central well subject to a homogeneous loss process[1], dynamics is tracked via the Lindblad master equation:

$$\frac{\partial \hat{\rho}}{\partial t} = -\frac{i}{\hbar}\left[\hat{H}, \hat{\rho}\right] + \sum_j \frac{\gamma_j}{2} \int \mathrm{d}^2\mathbf{r}\ \left(2\hat{\Psi}_j \hat{\rho} \hat{\Psi}_j^\dagger - \hat{\Psi}_j^\dagger \hat{\Psi}_j \hat{\rho} - \hat{\rho} \hat{\Psi}_j^\dagger \hat{\Psi} \right). \tag{7.2}$$

Due to the system's enormous Hilbert space the only tractable approaches to treat this problem are the c-field methods that consist of expressing the system at each site j by a classical (stochastic) field $\Psi_j(\mathbf{r}, t)$. With the inclusion of noise to mimic quantum fluctuations a small occupation is added in each mode, causing the integral over the density to diverge, even for the vacuum $|0\rangle$. When working in the TWA framework, care should be taken to avoid this ultraviolet catastrophe. As discussed in Sec. 4.4, a consistent cut-off is incorporated through the use of projection operators, introducing a separation between the low-energy, coherent region and the very sparsely populated high-energy modes in the incoherent region. Neglecting the latter and its effect on the coherent region results in a time evolution for the central well $j = 0$ governed by

$$i\hbar \mathrm{d}\psi_0 = \left\{ (H_{gp} - i\frac{\gamma}{2})\psi_0 - J\left(\psi_{-1} + \psi_1\right) \right\} \mathrm{d}t + \sqrt{\frac{\hbar\gamma}{2}} \mathrm{d}W(\mathbf{r}), \tag{7.3}$$

while for $j \neq 0$

$$i\hbar \mathrm{d}\psi_j = \left\{ H_{gp}\psi_j - J(\psi_{j-1} + \psi_{j+1}) \right\} \mathrm{d}t. \tag{7.4}$$

[1] In practice, this is achieved by rapidly scanning the electron beam over the entire atom cloud in the central well [167].

Here, the coherent field is given by

$$\psi_j(\mathbf{r},t) = \mathcal{P}\left[\Psi_j(\mathbf{r},t)\right] = \sum_{n\in\mathcal{C}} c_n(t)\Phi_n(x,y), \tag{7.5}$$

with $n = (n_x, n_y)$ and

$$H_{gp}\psi_j = \mathcal{P}\left\{\left[-\frac{\hbar^2\boldsymbol{\nabla}_r^2}{2m} + \frac{m\omega_x^2x^2}{2} + \frac{m\omega_y^2y^2}{2} + g_{2\mathrm{D}}|\psi_j|^2\right]\psi_j\right\} \tag{7.6}$$

is the projected Gross-Pitaevskii operator. The most suitable basis is given by the single-particle eigenstates, i.e. the harmonic oscillator eigenfunctions

$$\left[-\frac{\hbar^2\nabla^2}{2m} + \frac{m\omega_x^2x^2}{2}\right]\alpha_{n_x}(x) = \hbar\omega_x\left(n_x + \frac{1}{2}\right)\alpha_n(x). \tag{7.7}$$

The 2D fields can then be factorised as $\Phi_n(x,y) = \alpha_{n_x}(x)\alpha_{n_y}(y)$ and the coherent region defined by an energy cut-off E_c:

$$\mathcal{C} = \left\{\forall n \in \mathbb{N}^2 : E_n = \hbar\omega_x\left(n_x + \frac{1}{2}\right) + \hbar\omega_y\left(n_y + \frac{1}{2}\right) \leq E_c\right\}. \tag{7.8}$$

This inevitably leads to a dependence of results on the number of modes included. Particles enter the lossy system site at an energy close to μ_R, the chemical potential of a full site. For these particles to be able to relax to the ground state we should include in the coherent region modes up to at least $2\mu_R$. Previous simulations by Reeves & Davis have indicated that results are insensitive to the choice of E_c within the range of $2\mu_R$ to $3\mu_R$ [53]. Modes in the coherent region above the chemical potential will only be sparsely occupied making them susceptible to quantum fluctuations. We therefore consider the TWPGPE, treating the initial conditions stochastically and including the noise term in Eq. (7.3), which satisfies

$$\langle \mathrm{d}W(\mathbf{r},t)\mathrm{d}W(\mathbf{r}',t')\rangle = \mathrm{d}t\mathrm{d}t'\delta_{\mathcal{C}}(\mathbf{r},\mathbf{r}')\delta(t-t'). \tag{7.9}$$

The kernel of the coherent region, defined as $\delta_{\mathcal{C}}(\mathbf{r},\mathbf{r}') = \sum_{n\in\mathcal{C}}\Phi_n(\mathbf{r})\Phi_n(\mathbf{r}')$, acts as a Dirac delta function when working on that subspace.

7.1.1 Filling dependent tunnelling

The chemical potential of a full site μ_R is generally greater than the radial harmonic oscillator spacing $\hbar\omega_r$. In the case of two coupled sites which are both full,

particles can resonantly tunnel directly from one condensate mode into the other. Conversely, for a large population imbalance high energetic particles from the full site can only tunnel into excited modes of the (nearly) empty well and relax to the bottom of the trap through collisions. Overlap between these excited modes and the driving wave function is rather small, meaning the effective tunnelling rate is diminished, $J_{\text{eff}} < J$. The filling-dependent nature of the tunnelling is again evidenced by the particle currents. Taking $\psi_j(\mathbf{r}) = \sqrt{n_j(\mathbf{r})}e^{i\theta_j(\mathbf{r})}$ and integrating over the radial degrees of freedom, $N_j = \int \mathrm{d}^2\mathbf{r}\; n_j(\mathbf{r})$, we find from Eq. (7.3):

$$\frac{\mathrm{d}N_j}{\mathrm{d}t} = \frac{2J}{\hbar}\left(\eta_{j-1,j}\sqrt{N_{j-1}N_j} + \eta_{j+1,j}\sqrt{N_{j+1}N_j}\right) - \gamma_j N_j, \tag{7.10}$$

with the so-called *Franck-Condon factors* [48, 53, 56]

$$\eta_{k,j} = \frac{\mathrm{Im}\left[\langle\psi_k|\psi_j\rangle\right]}{\sqrt{N_k N_j}} = \frac{1}{\sqrt{N_k N_j}}\int \mathrm{d}^2\mathbf{r}\;\sqrt{n_k(\mathbf{r})n_j(\mathbf{r})}\sin\left[\Delta\theta_{k,j}(\mathbf{r})\right], \tag{7.11}$$

normalized measures of the wave function overlap between coupled fields that reduces the effective tunnelling. Here, $\Delta\theta_{k,j}(\mathbf{r}) \equiv \theta_k(\mathbf{r}) - \theta_j(\mathbf{r})$. The main consequence of this filling dependent tunnelling is the observation of *bistability* in the finite time steady-states and resulting hysteresis loops as J or γ are varied.

7.2 Inherited coherence

Steady-states of the lossy system on the upper and lower branch of the hysteresis loop are in the literature referred to as *superfluid* and *normal* phases, respectively [48, 50, 53]. Where the former is evident from the large particle currents and extensive phase coherence, the latter is less obvious. On the lower branch, driving is very much detuned from the ground state. It was assumed that particles can only relax to the condensate through collisions [53]. This neglects the possibility of a large fraction of the atoms accumulating in an excited state.

7.2.1 Non-equilibrium condensation

The system's out-of-equilibrium nature means that steady states deviate from thermodynamic equilibria, giving rise to a richer phase diagram. States are determined by a competition between losses, inherent or engineered, and additional pumping. As we know from earlier chapters, these systems commonly occur in quantum optics. A specific medium that has been at the centre of intensive re-

search over the past decades is the polariton fluid in a semiconductor microcavity [168]. Many phenomena related to quantum degeneracy, e.g. macroscopic phase coherence or superfluidity, have been observed in this intrinsically non-equilibrium system [169, 170].

Exciton-polaritons are quasi-particles that are formed by a strong coupling between photons coherently injected into the cavity by a laser, and excitons[2] in the medium. Due to the polariton's finite lifetime a continuous replenishment is required. A distinction can be made in the way that long-range coherence over spatially extended areas manifests for these bosonic quasi-particles. One way to introduce a coherent polariton fluid is to have the laser pump close to resonance with the polariton mode [119, 171, 172]. Basically, the polariton field inherits the coherent properties of the laser and a condensate appears. However, this condensate is not the result of *spontaneous* breaking of the continuous symmetry under global rotations of the phase, characteristic of the second-order phase transition. Instead, $U(1)$-symmetry is explicitly violated by the pump, i.e. macroscopic coherence is imprinted on the system by the coherent laser. In a single-mode approximation this setup is well described by the model that we discussed in Chapter 5. An analogy can be made with a ferromagnet, which has random spins at high temperature above the critical point. The coherence length is set by λ_{dB}. Applying a strong external magnetic field will align spins and lead to a non-zero order parameter. In other words, $U(1)$-symmetry is forcefully broken and displays the same long range order generally related to condensation.

Alternatively, polaritons can be injected through continuous high-energy illumination, away from resonance. Cooling down through the emission of phonons and polariton scattering leads to a complete loss of the coherent properties of the injected laser light. Increasing the laser power, and consequently the density, above a threshold value leads to an accumulation of polaritons in the in-plane zero momentum state [62, 168]. As a consequence, macroscopic coherence can be observed, but not as a direct inheritance from the pump. Condensation in this setup does correspond to a spontaneous breaking of $U(1)$-symmetry.

Non-equilibrium condensation is interesting in that it can display more exotic features like condensation in excited states [173]. A thorough understanding of the phases in the central, lossy well of the dissipative Josephson array is still lacking, hence we study it here. Similar to optical systems, condensation in the lossy

[2] An exciton is itself a quasi-particle, an electron-hole bound pair state in a semiconductor.

site will depend on inheritance from the pump profile and the relaxation to the ground state during which coherence is most likely lost. In the dissipative Josephson array the reservoirs resemble an imperfect laser, since they are themselves subject to quantum fluctuations. Although dephasing between the sites reduces the coherence of the drive onto the central well, the sites that couple to it remain largely occupied and fairly coherent structures. The pumping scheme is a balance between coherent driving and the injection of incoherent *hot* particles. In the following, we talk about a 'condensate' in an out-of-equilibrium setting to refer to the macroscopic occupation of a coherent wave function. We focus on the coherence properties transferred from the reservoir sites. We assess condensation in particular through the first-order and second order coherence functions.

7.2.2 Perfect coherent drive

In a first instance, 'imperfection' of the drive is neglected. We start by examining the multi-mode analogue of the single Kerr resonator as a frame of reference. For simplicity a one-dimensional wire is considered, mimicking the setup where one of the radial trapping frequencies is much larger $\omega_y \gg \omega_x$. Neglecting any dephasing and reduction in the reservoirs, we approximate the dynamics as being captured by the stochastic PGPE

$$i\hbar \mathrm{d}\psi_S(x,t) = \{(H_{gp} - i\gamma/2)\,\psi_S(x,t) + F(x,t)\}\,\mathrm{d}t + \sqrt{\gamma/2}\mathrm{d}W(x,t), \qquad (7.12)$$

where the projected Gross-Pitaevskii operator is similar to (7.6), but limited to one spatial degree of freedom. Different from many optical systems, the driving amplitude is not spatially homogeneous, but $F(x,t) = 2J\psi_R(x)e^{-i\mu_R t/\hbar}$, where the spatial profile $\psi_R(x)$ is obtained by solving for the ground state solution of the GP operator,

$$(H_{gp} - \mu_R)\,\psi_R = 0. \qquad (7.13)$$

The frequency of the drive is again determined by the chemical potential and so is the spatial profile, unlike a laser which has the possibility of tuning both the power and frequency independently. Typically, the reservoir modes in experiments start with a large particle occupation, $\mathcal{O}(10^2\text{-}10^3)$, and retain more or less the same level of filling throughout the measurement. Kinetic energy for these large, slowly varying atom clouds is relatively small compared to the interaction (or potential) energy. The driving profile is therefore well approximated by the inverted parabola that is the Thomas-Fermi profile $|\psi_R|^2 = [\mu_R - V(x)]/g$, as demonstrated in Fig. 7.1(a).

Due to the non-uniform nature, exact solutions for the correlation functions are out of reach. However, to achieve a better understanding we solve the problem semi-analytically at different levels of approximation. Given that the particle density on the lower branch is relatively low, with an occupation of less than 10% of that of the reservoirs, it is a reasonable assumption that the interaction energy in this phase plays a less significant role in comparison to the driving. A first, zeroth order approximation treats the ideal, non-interacting Bose gas deterministically. The fully coherent steady-state solution is found to be

$$\psi_S(x) = \sum_{n\in\mathcal{C}} \frac{2Jc_n^{(r)}}{E_n - \mu_R - i\gamma/2}\alpha_n(x), \tag{7.14}$$

given that the driving profile can be expanded as $\psi_R(x) = \sum_{n\in\mathcal{C}} c_n^{(r)}\alpha_n(x)$. Comparison to the numerically obtained stationary solution of the interacting system in Fig. 7.1(b) confirms that qualitatively the solution for the driven-dissipative cloud is mainly determined by the properties of the pump. The spatial profile of this out-of-equilibrium state is remarkably different from the ground state of the trap and actually resembles very closely the harmonic eigenfunction with eigenenergy $E_n = \hbar\omega_x(n + 1/2) \approx \mu_R$, in this case $n = 13$, shown in the same figure by the dashed line. Highly energetic atoms are pumped into an excited state, at an energy close to that of the reservoir, where they would generally undergo collisions through which they would relax to the ground state. Due to dissipation, however, particles are lost from the trap before having the chance to relax.

In order to determine the correlation functions, we go beyond the mean-field limit that treats only the coherent part of the matter field. A treatment in the TWA allows the calculation of all equal time correlators. To start, the reduced one-body density matrix and the first-order correlation function are determined respectively as

$$\rho^{(1)}(x,x') = \langle\hat{\psi}_S^\dagger(x,t)\hat{\psi}_S(x',t)\rangle = \langle\psi_S^*(x,t)\psi_S(x',t)\rangle_W - \frac{1}{2}\delta_{x,x'} \tag{7.15}$$

and

$$g^{(1)}(x,x') = \frac{\rho^{(1)}(x,x')}{\left[\langle\hat{n}(x,t)\rangle\langle\hat{n}(x',t)\rangle\right]^{1/2}}, \tag{7.16}$$

where $\langle\hat{n}(x,t)\rangle = \langle|\psi_S(x,t)|^2\rangle_W - 1/2$. The expectation values $\langle\ .\ \rangle_W$ denote the statistical average over an ensemble of realisations of the stochastic PGPE in Eq. (7.12). Fig. 7.2 displays the similarities and contrast between the *superfluid* and *normal phase*. The broad background in the one-body density matrix around

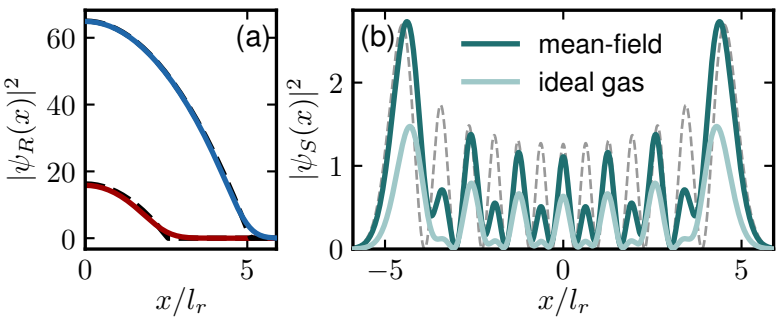

Figure 7.1 – Stationary states in a 1D harmonic trap. (a) Ground states of the time-independent GPE (7.13) for $\mu_R/\hbar\omega_x = 13$ (blue) and $\mu_R/\hbar\omega_x = 3.3$ (red). Dashed black lines display the corresponding Thomas-Fermi profile. (b) Density profile of the *normal* state obtained as a numerical solution of the PGPE (7.12) in the absence of fluctuations and the noise term. This is compared to the analytic solution for the ideal Bose gas in Eq. (7.14). For reference, the dashed line displays $|\alpha_n(x)|^2$, the n-th harmonic oscillator eigenfunction with $n = 13$.

the diagonal $n(x) = \rho^{(1)}(x, x)$, evident for the superfluid phase in Fig. 7.2(a), characterizes the off-diagonal long range order. The background for the same quantity in the normal phase is more irregular; see Fig. 7.2(b). Coherence exists between peaks in the density, whereas the regions of vanishing density lead to scars in the off-diagonal long range order. The density profile can be read from the diagonal $\rho^{(1)}(x, x)$. Just like the mean-field picture, density in the low occupied state is peaked away from the centre. The normalised first order correlation function emphasizes phase coherence even more. The maximum value on the diagonal now lies at unity. When the lossy system is densely occupied, ψ_S couples resonantly to the perfectly coherent reservoir ψ_R and is therefore itself fully coherent over the whole atom cloud, as shown in Fig. 7.2(c). No fluctuations are present due to the coherent pumping of the condensate overpowering any noise from the interactions. Despite the smaller particle number on the lower branch, a very similar result is obtained in Fig. 7.2(d) for the *normal* state. Off-diagonal values of $g^{(1)}$ come close to unity, but uniformity of the background is disrupted by lines of reduced coherence due to the oscillatory density pattern. Artefacts at the edges ($x \approx x' \gtrsim 6l_r$) originate from the energy cut-off on the one hand and a finite sample size for the Wigner averages on the other.

Additionally, one can consider the equal time second-order correlation function, a

measure of the density coherence defined as

$$g^{(2)}(x,x') = \frac{\langle \hat{\psi}_S^\dagger(x,t)\hat{\psi}_S^\dagger(x',t)\hat{\psi}_S(x,t)\hat{\psi}_S(x',t)\rangle}{\hat{n}(x,t)\hat{n}(x',t)}, \tag{7.17}$$

where the fourth order correlator is given in terms of Wigner averages as

$$\langle \hat{\psi}_S^\dagger(x,t)\hat{\psi}_S^\dagger(x,t)\hat{\psi}_S(x,t)\hat{\psi}_S(x,t)\rangle = \langle |\psi_S(x,t)|^4\rangle_W - 2\langle |\psi_S(x,t)|^2\rangle_W - \frac{1}{2}. \tag{7.18}$$

A plot of the density-density correlations $g^{(2)}(x,x)$ is given in Fig. 7.2(e), comparing both phases. Generally, a thermal state features a second-order correlator close to the maximum value $g^{(2)}(x,x) \approx 2$, while these values are suppressed to unity for a condensate. The results for the superfluid phase are consistent with this, whereas the normal state is not. The overlap between $\psi_S(x)$ on the lower branch and $\psi_R(x)$ is maximal away from the centre, resulting in peaks in density at $x \approx \pm 3l_x$ and a $g^{(2)}$ closer to one. Some particles move to the centre through collisional relaxation making them thermal. It is clear that the matter field contains both an incoherent, thermal part and a substantial condensate component.

7.2.3 Bogoliubov in the TWA

In order to further our understanding of these out-of-equilibrium phases we decompose the field into a fully coherent condensate $\psi_0(x)$ and an incoherent part capturing fluctuations $\delta\psi(x,t)$, so that $\psi_S(x,t) = \psi_0(x) + \delta\psi(x,t)$. The former is obtained from imaginary time evolving Eq. (7.12) without noise or fluctuations and satisfies $|\psi_0| \gg |\delta\psi|$. Evolution of the fluctuations in time is, up to first order, governed by

$$\mathrm{d}\mathbf{\Delta}_x = \{-iB\mathbf{\Delta}_x - \gamma/2\}\,\mathrm{d}t + \sqrt{\gamma/2}\mathrm{d}\mathbf{W}_x, \tag{7.19}$$

where we defined the vector $\mathbf{\Delta}_x \equiv \left[\delta\psi(x),\ \delta\psi^*(x)\right]^T$, the noise vector $\mathrm{d}\mathbf{W} \equiv \left[\mathrm{d}W(x,t),\ \mathrm{d}W(x,t)^*\right]^T$, and the well-known Bogoliubov matrix

$$B = \begin{pmatrix} \epsilon(x) + 2g_{1\mathrm{D}}|\psi_0(x)|^2 - \mu_R & g_{1\mathrm{D}}\psi_0(x)^2 \\ -g_{1\mathrm{D}}\left[\psi_0^*(x)\right]^2 & -\epsilon(x)^* - 2g_{1\mathrm{D}}|\psi_0(x)|^2 + \mu_R \end{pmatrix}, \tag{7.20}$$

with $\epsilon(x)$ the free particle kinetic energy. The fluctuation field can be expanded in the harmonic oscillator basis as well in which case an equivalent equation of

motion is obtained:

$$\mathrm{d}\mathbf{\Delta}_n = \left\{-iQ^\dagger BQ\mathbf{\Delta}_n - \gamma/2\mathbf{\Delta}_n\right\}\mathrm{d}t + \sqrt{\gamma/2}Q^\dagger d\mathbf{W}. \tag{7.21}$$

Given a finite spatial grid of $\mathcal{N}$ points with grid spacing Δx and an energy cut-off in the spectral basis $E_c = \hbar\omega_x(N_c+1)$, the transformation to the coherent region is represented by the matrix

$$Q = \begin{bmatrix} P & O \\ O & P \end{bmatrix}, \text{ where } P = \sqrt{\Delta x}\begin{bmatrix} \alpha_0(x_1) & \dots & \alpha_{N_c}(x_1) \\ \vdots & \ddots & \vdots \\ \alpha_0(x_\mathcal{N}) & \dots & \alpha_{N_c}(x_\mathcal{N}) \end{bmatrix}. \tag{7.22}$$

Our aim is to find a solution for the correlation matrix

$$\langle\mathbf{\Delta}\mathbf{\Delta}^\dagger\rangle = \left\langle \begin{pmatrix} \delta\vec{\psi} \\ \delta\vec{\psi}^* \end{pmatrix}\begin{pmatrix} \delta\vec{\psi}^* & \delta\vec{\psi} \end{pmatrix}\right\rangle_W. \tag{7.23}$$

Using the rules of Ito calculus,

$$\mathrm{d}\mathbf{\Delta}\mathbf{\Delta}^\dagger = (\mathrm{d}\mathbf{\Delta})\mathbf{\Delta}^\dagger + \mathbf{\Delta}(\mathrm{d}\mathbf{\Delta}^\dagger) + \mathrm{d}\mathbf{\Delta}\cdot\mathrm{d}\mathbf{\Delta}^\dagger, \tag{7.24}$$

the stochastic differential equation for this new variable is derived and after taking the expectation value results in

$$\mathrm{d}\langle\mathbf{\Delta}\mathbf{\Delta}^\dagger\rangle = \left\{-i\tilde{B}\langle\mathbf{\Delta}\mathbf{\Delta}^\dagger\rangle + i\langle\mathbf{\Delta}\mathbf{\Delta}^\dagger\rangle\tilde{B}^\dagger - \gamma\langle\mathbf{\Delta}\mathbf{\Delta}^\dagger\rangle + \frac{\gamma}{2}I\right\}\mathrm{d}t, \tag{7.25}$$

with the Bogoliubov matrix $\tilde{B} = Q^\dagger BQ$ expressed in the spectral basis. Alternatively, we can vectorize the correlation matrix

$$\langle\mathbf{\Delta}\mathbf{\Delta}^*\rangle = \left\langle \begin{pmatrix} \delta\vec{\psi} \\ \delta\vec{\psi}^* \end{pmatrix}\otimes\begin{pmatrix} \delta\vec{\psi}^* \\ \delta\vec{\psi} \end{pmatrix}\right\rangle_W \tag{7.26}$$

and the corresponding equation of motion,

$$\mathrm{d}\langle\mathbf{\Delta}\mathbf{\Delta}^*\rangle = \left\{-i\left(\tilde{B}\otimes I - I\otimes\tilde{B}^*\right)\langle\mathbf{\Delta}\mathbf{\Delta}^*\rangle - \gamma\langle\mathbf{\Delta}\mathbf{\Delta}^*\rangle + \frac{\gamma}{2}I\otimes I\right\}\mathrm{d}t. \tag{7.27}$$

A stationary solution is then readily derived to be

$$\langle\mathbf{\Delta}\mathbf{\Delta}^*\rangle = A^{-1}\cdot\frac{\gamma}{2}I\otimes I, \tag{7.28}$$

where we set $A = -i(\tilde{B} \otimes I - I \otimes \tilde{B}^*) - \gamma I \otimes I$. The one-body density matrix of the coherent region is then defined as

$$\rho_B^{(1)}(x, x') = \langle \hat{\psi}_S^\dagger(x)\hat{\psi}_S(x')\rangle = \psi_0^*(x)\psi_0(x') + \sum_{n,m}^{N_c} \langle \delta\hat{\psi}_n \delta\hat{\psi}_m\rangle \alpha_n(x)\alpha_m(x'), \quad (7.29)$$

with the operator expectation values $\langle \delta\hat{\psi}_n \delta\hat{\psi}_m\rangle = \langle \delta\psi_n \delta\psi_m\rangle_W - \frac{1}{2}\delta_{n,m}$.

Phase coherence in the normal state is qualitatively very similar in the Bogoliubov picture, as is clear from Fig. 7.3(a) and (b). A quantitative comparison is shown in Fig. 7.3(c) confirming the agreement with the TWA approach. The coherently driven, lossy system is well-described by a coherent field and additional Gaussian fluctuations. This indicates that interactions are present, but their effect is limited. The steady-state is determined by a balance between pumping and losses. Atoms are more likely to be lost from the system rather than undergo collisional relaxation to the ground state. This also implies that the TWA results won't have a high cut-off dependency if $E_c \gtrsim 2\mu_R$.

7.2.4 Josephson array

Let us now consider the entire dissipative Josephson array, where pumping originates from internal degrees of freedom and constitutes an imperfect 'pumping laser'. Neighbouring sites are not perfectly coherent but contain a small thermal part, meaning that the condensate fraction on the lossy site will also be reduced. We solve Eq. (7.3) for a reasonably large system of $L = 121$ coupled wires, with $J = 0.3\hbar\omega_x$, $\gamma = 0.6\omega_x$ and an interaction strength $g_{1\mathrm{D}} = 0.1\hbar\omega_x l_x$. With the chemical potential set to $\mu_R/\hbar\omega_x = 12$ a full site contains in its ground state around $N_f \approx 850$ atoms, similar to experiments. The steady state on the lower branch is reached when the central well is initially depleted to 5% of a full site. An ensemble of 2×10^4 simulations is averaged over at time $t = 40\omega_x^{-1}$ to determine the steady-state properties presented in Fig. 7.4.

Phase coherence (see panel (a)) is clearly diminished compared to the coherently driven system, yet regions of long-range coherence persist with intermediate values up to $g^{(1)} \approx 0.75$. Density fluctuations, shown in Fig. 7.4(b), convey a similar story. The suppression of fluctuations is again less pronounced, yet second order coherence is still lowered significantly. At the edges of the atom cloud, around $x/l_x = \pm 4$, it reaches the smallest value $g^{(2)} \approx 1.6$. Towards the centre of the cloud, we again observe dips in density fluctuations at the positions of the density

maxima, where also the first order coherence is enhanced. This means that the field still contains a notable condensate part. The part of the density that corresponds to the condensate is in fact related to the second order correlation function through as $n_c(x) = \sqrt{2 - g^{(2)}(x,x)}n(x)$ [90]. For comparison, the proportion of condensate to the full matter field is plotted in Fig 7.4(b) as well. Spatial integration of $n_c(x)/n(x)$ or straightforward diagonalization of the density matrix results in an overall condensate fraction $N_c/N \approx 40\%$, while it is approximately 90% in the neighbouring wells.

7.2.5 Validity of the TWA

Here, we report briefly on the validity of the results. An all-encompassing set of validity conditions for the TWA is difficult to establish. Technically, the TWPGPE is only valid when every mode has a large occupation [81], strongly limiting its applicability. This requirement is clearly not satisfied for the current system, where for each site a number of modes are included that lie above the chemical potential and that are dominated by noise. From their comparison of the truncated Wigner method with the time-dependent Bogoliubov approximation, Sinatra *et al.* [174] concluded that simulations break down when the noise over all modes exceeds the total particle number. A less stringent validity condition is therefore:

$$N \gg \mathcal{N}/2, \tag{7.30}$$

with total particle number N and number of simulated modes $\mathcal{N}$. Regarding each site in the Josephson array as a separate multimode system, this requirement is definitely satisfied for a full site, but not for the central well in the low-density state.

However, dissipation or *damping* γ is a known stabilizer of the TWA method in regimes where it would otherwise fail for closed systems. A thorough analysis of the regimes of validity for a multi-mode driven-dissipative system was performed in Ref. [175]. A straightforward application of their conclusions is not possible due to the different detuning of the drive for each mode in the central well. However, in our simulations we remain far enough from the interaction dominated regime where the TWA generally breaks down, i.e. in general $\gamma/U \gtrsim 1$. The physics we describe is fairly classical, meaning it does not feature a high degree of entanglement that the TWA ordinarily fails to capture. Nonetheless, signal-to-noise ratio does becomes challenging at small densities, especially to determine $g^{(2)}$. To mitigate this we require averages over a large ensemble of trajectories.

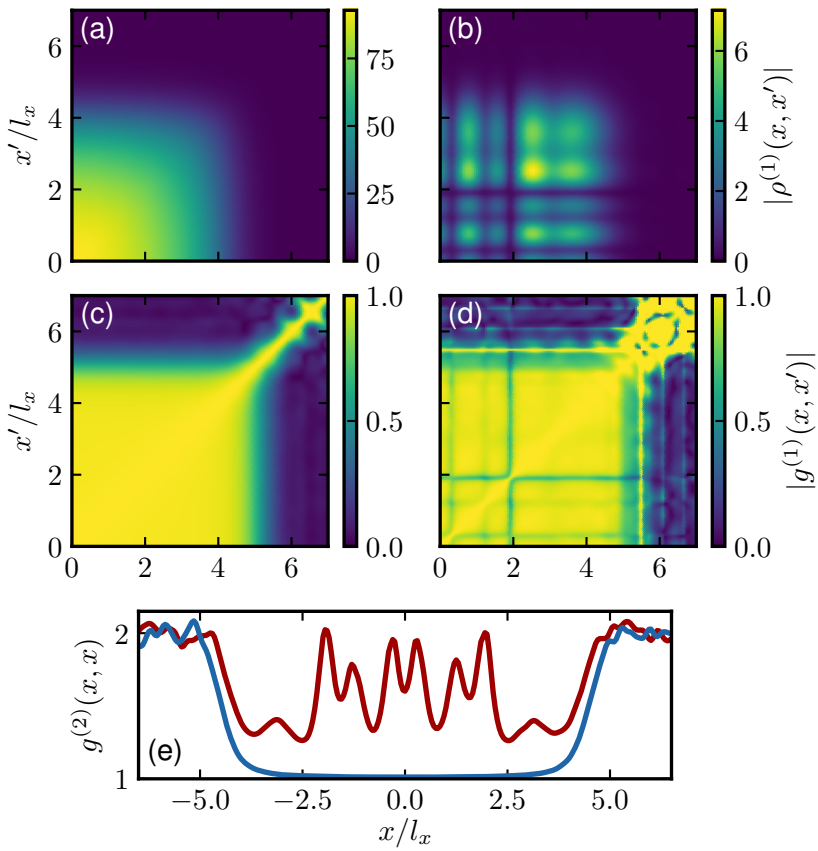

Figure 7.2 – Comparing equal time correlation functions of the two (meta)stable states. The one-body density matrix for the superfluid (a) and normal (b) phase of the harmonically trapped, coherently driven atom cloud. Normalised first order correlation functions are plotted respectively in (c) and (d). (e) The local second-order correlator for the condensate on the upper branch (blue) and the normal state on the lower branch (red). System parameters are $J = 0.35\hbar\omega_x$, $g_{1D} = 0.1\hbar\omega_x l_x$, $\mu_R = 9\hbar\omega_x$ and $\gamma = 0.8\omega_x$.

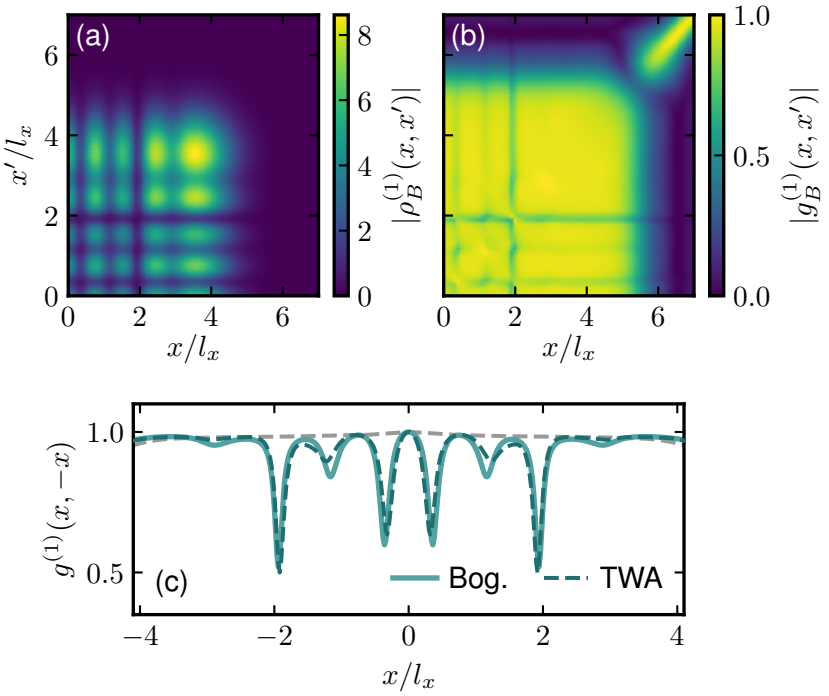

Figure 7.3 – Phase coherence in the Bogoliubov picture. One-body density matrix (a) and normalized coherence function determined by numerically solving Eq. (7.28). (c) Quantitative comparison shows excellent agreement in the predicted phase coherence between the semi-analytic Bogoliubov solution (full) and numerical TWA results (dashed). The gray dashed line displays the same quantity for the superfluid phase.

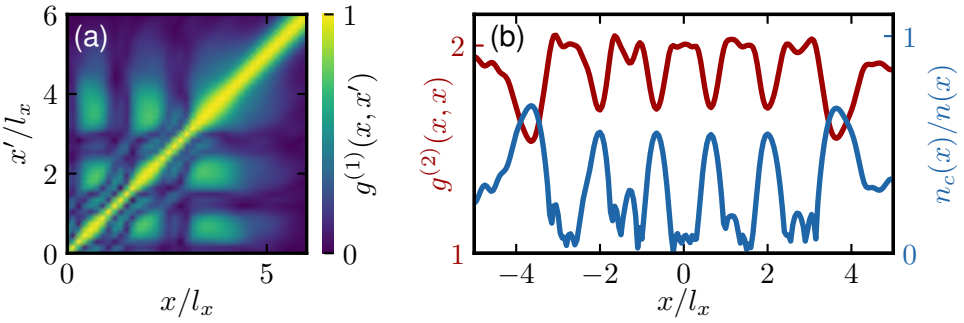

Figure 7.4 – Inherited coherence in the Josephson array. (a) Phase coherence characterized by off-diagonal peaks of $g^{(1)} \approx 0.75$ corresponding again to peaks in density. (b) Local second order correlation function and the ratio of condensate density to total density derived from it.

7.3 Dimensional crossover

The dimensionality of a condensed matter system profoundly impacts its properties, in particular the long-range order. In lower dimensional, equilibrium systems thermal and quantum fluctuations tend to destroy order [29, 176]. A transition to a quasi-condensate can however still occur, where coherence decays over distance following a power-law in 2D [177, 178] and exponentially in 1D [4]. The sites in the Josephson array are, however, finite due to the harmonic trapping and to small to witness the decay in the long-range order. Therefore, we still speak of condensation in this setting.

We study the effect of dimensionality on the out-of-equilibrium state by changing the geometry of the harmonic trap. A gradual transition from 2D to 1D is realised by increasing the trap frequency ω_y while keeping ω_x fixed. Physics changes drastically as the trap's geometry is altered. The interaction energy naturally increases as the gas is confined more in the y-direction. For a fixed number of particles this would lead to an increase of the chemical potential, modifying the bistability as a result. To consistently probe the same point in the hysteresis loop at different trappings we instead keep the detuning $E_0 - \mu_R$ constant, although this may not be the most experimentally relevant protocol. In Fig. 7.5 we show the occupancy of the single-particle energy levels E_n for different ratios of the trapping frequencies. Particles are pumped into the excited levels of the central well closest to the chemical potential of the reservoirs, $E_n \approx \mu_R = 9\hbar\omega_x$. Conservation of symmetry from the driving profile of the neighbouring wells makes that primarily even levels are occupied.

In the first panel of Fig. 7.5, the spectral density distribution is displayed for a radially isotropic system. Here, one can clearly observe the degenerate levels corresponding with $n_x + n_y = 8$, from which the symmetric ones are resonantly pumped. From there, scattering indeed leads to the relaxation towards lower energy levels and consequently also to small occupations in the sea of levels above μ_R. Scattering can occur in both directions, x and y, except for states in the ground state of one of the two traps, e.g. $(n_x = 0, n_y = 8)$ and $(n_x = 8, n_y = 0)$. Particles in these excited states have less possible scattering channels, hence the slight peak in occupation there. By increasing ω_y – for a fixed ω_x – we increase the level spacing in the y-direction, effectively suppressing interactions in that direction. The second panel of Fig. 7.5 depicts the setup where $\Lambda = \omega_y/\omega_x = 2$, where the clear outlier of the occupation in the excited state $E(n_x = 0, n_y = 4)$ is

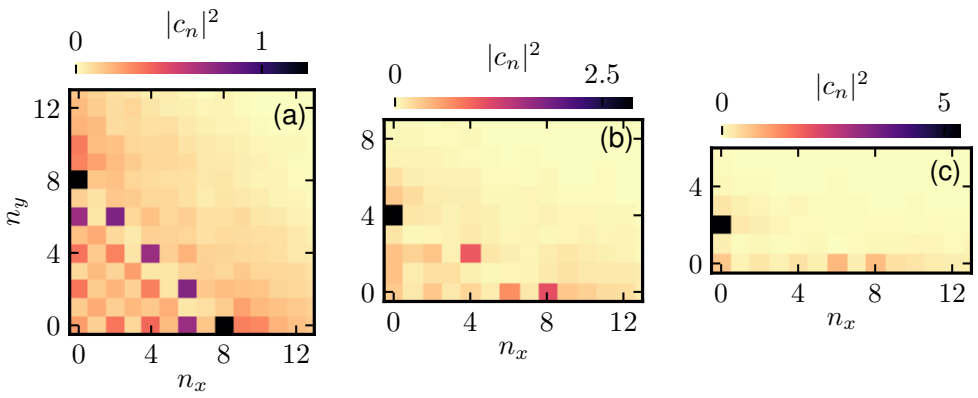

Figure 7.5 – Occupation of single-particle states at different trapping ratios $\Lambda = \omega_y/\omega_x$. (a) With equal level spacing in both directions, interactions dominate. With increasing anisotropy, excited states of the tight trap (y-direction) become isolated due to growing level spacing. This leads to an accumulation of density in the excited states (b) $E(n_x = 0, n_y = 4)$ for $\Lambda = 2$ and (c) $E(n_x = 0, n_y = 2)$ for $\Lambda = 4$ (c).

obvious. From here, particles can only relax further through scattering in the y-direction, where the level spacing is larger. Compare this with $E(n_x = 8, n_y = 4)$, a degenerate level that is an excited state of the trap along the x-axis and that has a significantly lower steady-state occupation. Excited states in the y-direction become more isolated as the trap becomes tighter, so when particles are resonantly pumped there they don't scatter that much. The effect is even more pronounced in the third panel, for which $\Lambda = 4$.

7.3.1 Condensate fractions

There exist many ways to characterize condensation. A macroscopic number of particles occupying the single-particle ground state only makes sense for non-interacting particles in equilibrium. The requirement for true condensation that the one-body density matrix $\rho^{(1)}(\mathbf{r}-\mathbf{r}')$ tends to a finite value in the limit $|\mathbf{r} - \mathbf{r}'| \to \infty$ is not really relevant for trapped systems. A more general measure is provided by the Penrose-Onsager criterion [179], also based on the reduced density matrix. One speaks of condensation when the largest eigenvalue of $\rho^{(1)}$ is of the order of the total particle number, i.e. when an eigenstate of the system is macroscopically occupied. These eigenstates are only equivalent to the single-particle states, e.g. harmonic oscillator eigenstates in our case, for non-interacting particles. This criterion can thus be applied independent of the interactions or the system's geo-

metry and irrespective of whether the system is at thermal equilibrium or not [173].

From diagonalization of the numerically constructed reduced density matrix – see Eq. (7.15) – we obtain the eigenvalue spectra of which examples are shown in Fig. 7.6(a) and (b). All spectra display a single eigenvalue with significantly larger occupancy. Additionally, in Fig. 7.6(c) the proportion of this eigenvalue in relation to the overall occupancy, in other words the condensate fraction, is depicted at different trapping ratios Λ. From this it is clear that as the trap becomes more one-dimensional, the difference in occupancy with the rest of the spectrum increases, hence the condensate fraction increases. This relates back to the peak in the spectral density becoming more pronounced as the trap anisotropy grows. Although the eigenstates of our interacting system do not correspond exactly to the single-particle states, they are a good approximation. This increase persists up to $\Lambda = 4$, after which a sharp drop is observed. When $\omega_y \geq 5\omega_x$, the first symmetric excited state in the y-direction exceeds the chemical potential, effectively freezing out that direction of motion. As such, the drop can be regarded as the point of transition from an array of coupled 2D wells to 1D. Because energy level spacing along the x-axis is still much smaller than μ_R, the effect of scattering increases again leading to a drop in the coherent fraction.

Generally, we conclude that the low-density state in the central, lossy well is characterized by a significant inheritance of the coherent properties of the drive. This holds both in the case of coupled 1D as well as 2D sites. A balance between driving and losses results in an accumulation of particles in excited single-particle state. The precise condensate fraction greatly depends on the geometry of the traps and the interaction strength. Our work provides more insight in this regard, but it is also clear that further research is required for a more detailed understanding of the kinematics.

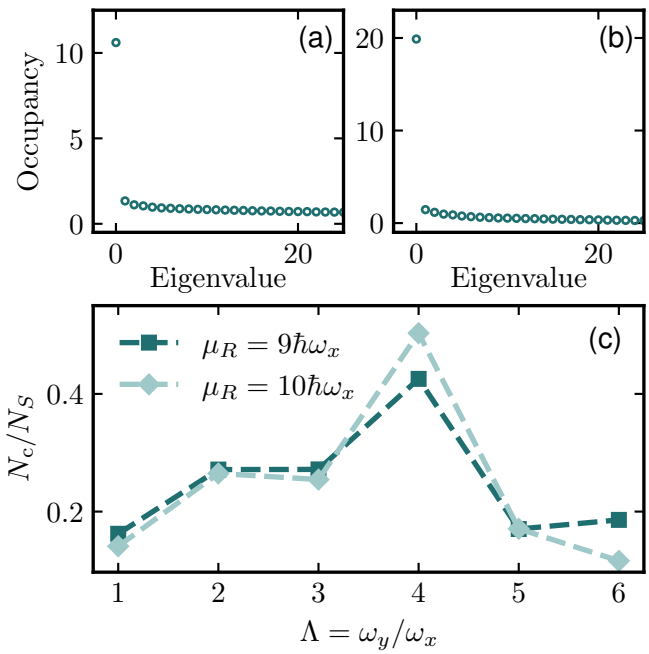

Figure 7.6 – Nonequilibrium condensate fraction. (a),(b) Eigenvalue spectra for $\Lambda = 1$ and $\Lambda = 4$, respectively, indicate a single eigenvalue with significantly larger occupation compared to the remainder. (c) Dependence of the condensate fraction on the ratio of trapping frequencies. Independent of the geometry in the transverse directions, the wave function of the central well contains a notable coherent part.

7.4 Summary

In this chapter we investigated the properties of the *normal* state in the mean-field bistability region. Reservoirs in the Josephson array serve as an imperfect laser for the dissipative well at its centre, suggesting coherence should be inherited up to some level even at low densities. First, we regarded a setup where one transverse spatial degree of freedom is frozen out. The case of a perfect coherent drive shows that interactions play a role, but don't dominate the steady-state. The balance of driving and losses results in a largely coherent, oscillating density profile closely resembling an excited single-particle state. In the Josephson array, where the reservoir modes are also subject to fluctuations, a similar result is obtained, but less pronounced. A smaller, but still significant condensate fraction is present in the low-density phase.

Interactions have a larger effect in the experimentally relevant stack of coupled 2D systems, due to a larger phase space. This results in a smaller condensate fraction inherited from the coherent reservoirs. Interestingly, with increasing anisotropy the condensate fraction rises significantly and this while interactions actually become stronger. Relaxation in the tightly trapped direction becomes suppressed, leading to the majority of particles accumulating in one excited single-particle state.

CHAPTER 8

Dynamical instability of the dark soliton

The contents of this chapter are subject of a manuscript in preparation:

Dark Soliton Formation as a Dark State Phase Transition in a Dissipative Bose-Hubbard Model
R. Ceulemans, S.E. Begg, M.J. Davis & M. Wouters

So far, we have overlooked an intriguing region in the phase diagram of (quasi-) one-dimensional systems, the soliton. In Sec. 6.1 we briefly mentioned the emergence of this additional phase with zero density on the lossy site, marked by a π phase difference between the two reservoirs. Including this state introduces dynamics fundamentally different from those discussed so far, where both reservoirs were assumed to drive in phase. While explicit experimental evidence of such a dark state remains elusive, simulations reveal its pronounced impact on the systems behaviour, altering properties like hysteresis or the Liouvillian gap. The stability of this phase – and thus its experimental detectability – depends on a number of system properties including the trap geometry or the presence of

localized losses. In this chapter, we explore the hypothesis that the experiments reported in Refs. [48, 50, 51] may actually exhibit a novel form of nonequilibrium criticality underpinned by dark soliton formation.

8.1 Introduction: Properties of localized non-linear excitations

Solitons are fundamental excitations, ubiquitous in non-linear systems [148–154], that exhibit particle-like properties and which have been observed in a range of cold atom experiments [155–158]. We start this chapter with a brief overview of the fundamental properties, both within the continuous and discrete 1D non-linear Schrödinger equation (NLS).

8.1.1 Uniform condensate

Let us first consider the one-dimensional time-dependent GPE

$$i\hbar\frac{\partial\psi(x,t)}{\partial t} = \left[-\frac{\hbar^2\nabla_x^2}{2m} + V(x) + g_{1\mathrm{D}}|\psi(x,t)|^2 - \mu\right]\psi(x,t), \tag{8.1}$$

that approximately describes a cigar-shaped BEC [180, 181]. For repulsive interactions, $g_{1\mathrm{D}} > 0$, this equation supports a family of solitonic *kink* excitations – localized density modulations or dips in the uniform background, accompanied by a phase jump. These kinks move through the system at a constant velocity v in such a way that their shape is preserved. So-called *grey* solitons are, in the absence of external trapping $V(x) = 0$, given by [4, 182–184]

$$\psi_s(x;q) = \sqrt{n_\infty}e^{-i\theta}\left(i\beta + \sqrt{1-\beta^2}\tanh\left[\frac{x-q}{\sqrt{2}\xi}\sqrt{1-\beta^2}\right]\right). \tag{8.2}$$

Here, the minimum is located at $q \equiv q(t) = q(0)+vt$, moving at a subsonic velocity v, such that $|\beta| \equiv |v/c| < 1$, where the speed of sound is given as $c = \sqrt{\mu/m}$. The width of a kink in the uniform background density n_∞ is determined by the healing length $\xi = \hbar/\sqrt{2m\mu}$, but is amplified by a factor of $1/\sqrt{1-\beta^2}$. Consequently, in the limit of $v \to \pm c$ the soliton broadens, its depth reduces, and it eventually tends to a sound wave before disappearing into the motionless, uniform ground state. The soliton energy can be expressed as [4]

$$E_s = \frac{4}{3}n_\infty\hbar c\left(1-\beta^2\right)^{3/2}. \tag{8.3}$$

Solitons behave as free particles with *negative effective mass* in the sense that their energy decreases with increasing velocity. Note that the energy of the solution is independent of the choice for the global phase θ. Experimentally, grey solitons have been created by means of different procedures [155–158, 185–187].

The particular case of a soliton at rest ($\beta = 0$), known as the *standing dark soliton* or *black soliton* (DS), is set apart by the exact zero density at its minimum and a π phase shift across the dip. It is the highest excited state in the family of grey solitons. Short-time fluctuations $\delta\psi(x,t)$ around the stationary solution in Eq. (8.1) can be described in Bogoliubov theory. In the thermodynamic limit, the continuous phonon spectrum on the mean-field background

$$\psi_s(x) = \sqrt{n_\infty}\tanh\left(x/\sqrt{2}\xi\right) \tag{8.4}$$

is given by [183, 188]

$$\epsilon_k = \sqrt{\epsilon_k^{(0)}\left(\epsilon_k^{(0)} + 2g\rho\right)}, \tag{8.5}$$

which matches the spectrum of a homogeneous condensate. Rather than to scatter the phonons, the standing soliton simply shifts their phase. Despite its energetic (and topological) instability, the dark soliton's eigenvalue spectrum is completely real, rendering it dynamically stable. A mode expansion of the fluctuations is complicated by the presence of zero-eigenvalue eigenmodes. Besides the phonon modes for $k > 0$, there are two *zero modes* with eigenenergy $\epsilon = 0$, arising from the breaking of continuous symmetries. Choosing the classical solution (8.4), we explicitly set the global phase to $\theta = 0$ as well as fix the position of the soliton at $q = 0$. However, the solution is invariant under change of the global phase or translation of the minimum in space. The Goldstone theorem states that the spontaneous breaking of a continuous symmetry, like we did by choosing (8.4), is associated with a gapless excitation mode, a Goldstone mode.

8.1.2 Dark soliton in an optical lattice

Introducing a periodic potential $V(x) = V_0\cos^2(kx)$, that effectively discretizes the spatial degree of freedom, profoundly affects soliton properties. As opposed to the exactly solvable 1D hard-core Bose gas [30, 31], integrability is broken for the Bose-Hubbard model. As a consequence, already on a mean-field level the dark soliton becomes unstable. Remembering the discrete GPE found in the

tight-binding limit,

$$i\hbar\frac{\mathrm{d}}{\mathrm{d}t}\psi_j = -J\left(\psi_{j-1} + \psi_{j+1} - 2\psi_j\right) + U|\psi_j|^2\psi_j - \mu\psi_j, \tag{8.6}$$

a discrete analogue of the static dark soliton can be expressed as [182, 189]

$$\phi_j = \sqrt{n_\infty}\tanh\left[(jd - q)/\sqrt{2}\xi\right], \tag{8.7}$$

with the healing length in the discrete system given by $\xi = \sqrt{Jd^2/\mu}$. Due to the discrete background the solution varies as the minimum shifts within the interval $0 \leq q < d$. Two extremes can be distinguished: the *site soliton* (SS) for $q = 0$, characterized by a single minimum zero-density lattice site, and the *link soliton* (LS) for $q = d/2$. The latter has two sites with minimal, but non-zero density. Both types are depicted in Fig. 8.1.

Changing q affects the structure of the excited state and, correspondingly, the excitation energy. The site soliton has a larger kinetic and potential energy than the LS, with the difference between the two constituting an energy barrier, the Peierls-Nabarro (PN) barrier [189, 190], impacting the stability of both solutions. A dynamic stability analysis, carried out through Bogoliubov-de-Gennes (BdG) linearization of the discrete GPE, reveals that both versions of the dark soliton are generally subject to a discreteness-induced instability [191]. Fig. 8.1 includes plots of the growth rates of the unstable modes, $\max\left(\mathrm{Im}[\omega_l]\right)$, representing the inverse of the solution's lifetime, in both cases as a function of J/μ. The LS exhibits a single unstable mode corresponding to a purely imaginary eigenvalue at every value of J/μ, which is localized around the soliton centre (as shown in the figure's inset). In contrast, the SS features a pair of unstable modes with both real and imaginary non-zero part that are each other's complex conjugate. These exponentially growing, oscillatory modes are more delocalized over the array. Both solutions become asymptotically stable as the soliton width increases. In the limit $J/\mu \to \infty$, the healing length becomes very large compared to the lattice spacing ($\xi \gg d$) such that one recovers the continuum limit and the energetic difference between LS and SS states vanishes. To the soliton the background becomes approximately continuous.

The dynamic instability leads in both cases to a decay of the excited state in real-time, depicted in Fig. 8.2. Most noteworthy is the oscillatory mechanism that impacts the site soliton, which can be explained as an effect of the PN energy barrier. The configuration with $q = 0$ is isolated on an energy peak, preventing

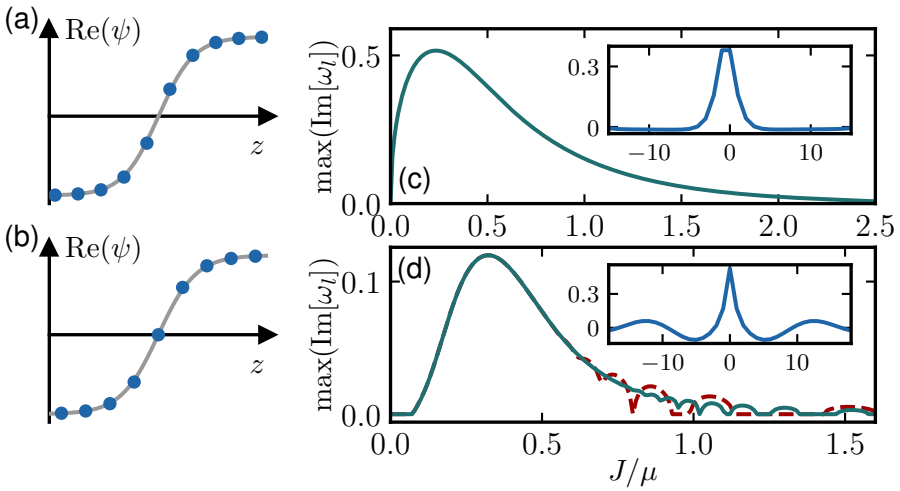

Figure 8.1 – Discrete dark soliton types and their instability. Spatial profiles of the link soliton (a) and site soliton (b). (c)-(d) Exponential growth rate of the unstable normal mode as a function of J for the respective excitations. Insets show the spatial profile of the phase fluctuations $(u_j - v_j)/2i$. The spectrum in (d) is depicted for both $L = 101$ (red) and $L = 301$ (green).

movement through the lattice. Before transitioning away from its initial position, like we see in the top panels for the LS, the site soliton must dissipate energy by coupling to real-frequency phonon modes, emitting sound waves that lead to the typical oscillating behaviour of nearby densities; see panel (d). This energy loss eventually enables the SS to decay in a fashion similar to the LS. Here, the soliton depth decreases while the velocity increase, i.e. the black soliton turns grey. The density dip then propagates ballistically in a spontaneously chosen direction.

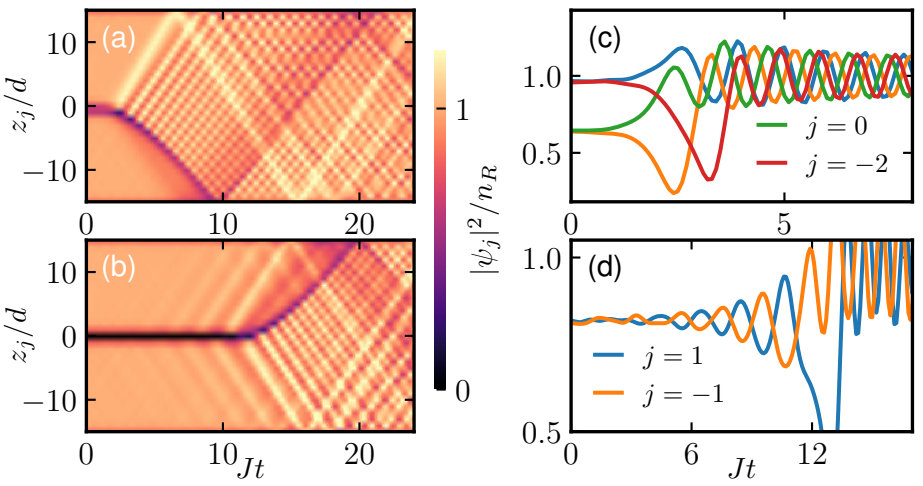

Figure 8.2 – Decay mechanisms of the link and site soliton. (a)-(b) Spatio-temporal plots of soliton decay show the quick departure of the LS (a) from its initial position, compared to the SS that oscillates around the centre for longer (b). (c)-(d) Time evolution of the density around the soliton core. This clearly shows the oscillatory nature of the SS instability.

8.2 Impact of soliton formation in quasi-1D Josephson array

We briefly mentioned in Chapter 6 how the soliton naturally appears in the 1D dissipative Bose-Hubbard model. While solitons are known to play an important role in 1D systems, their relevance in the fully 3D configuration is less obvious. Transverse spatial degrees of freedom introduce an additional instability mechanism, the snaking instability, through which the excited state can decay. In this section we discuss the impact of soliton formation in the experimentally relevant setup. We consider the array of 2D harmonically trapped BECs, described by the TWPGPE detailed in Eq. (7.3) in the previous chapter. Similar to the experimental setup, each well is assumed isotropic $\omega_x = \omega_y \equiv \omega_r$. To highlight the prevalence of the soliton, we briefly discuss the dynamics for the case without dissipation ($\gamma = 0$), which was considered experimentally in Ref. [47] and recently modelled quantitatively [56].

8.2.1 Impact of phase randomization on superfluid currents

Previously, the two half-chains driving the (lossy) low-density site were assumed to be phase coherent, as this was an ongoing assumption in literature [47, 50, 53, 55]. However, with the way the initial state is prepared experimentally this isn't necessarily always the case. Experimental runs that start with a depleted central well are preceded by a ramping up of the lattice potential. The increased optical lattice effectively isolates the atoms in each well for a fixed time during which the central well is depleted using the electron beam. Subsequently, the periodic potential is lowered rapidly, indicating the start of a measurement. During the preparation time, however, phases of each well are expected to drift due to thermal and quantum fluctuations and it has been verified that sites are decoupled long enough for the phases to be completely randomized [56]. The effect of such random phases can easily be lost in averages over many measurements (or stochastic trajectories) and is often assumed to be negligible.

Begg *et al.* studied the filling dynamics of a depleted site $j = 0$ after losses were turned *off* and nevertheless demonstrated a clear correlation of the current with the phase gradient $\Delta\Theta_0 = \Theta_{-1} - \Theta_{+1}$ [56]. Here, Θ_j is the spatially averaged phase, defined as

$$\Theta_j = A^{-1} \int_A \mathrm{d}^2\mathbf{r}\ \theta_j(\mathbf{r}) \equiv \langle \theta_j \rangle_{\mathbf{r}}, \tag{8.8}$$

with A a region in the centre of the harmonic trap of well j covering the bulk of the atomic cloud. To mimic the effect of dephasing, one entire half of the chain is multiplied by a random phase $e^{i\phi}$ at the beginning of each simulation. Filling times t_f in individual trajectories, defined as the time it takes the initially depleted well to reach 2/3 of its final value, are plotted against the initial phase difference $|\Delta\Theta_0|$ in Fig. 8.3. For moderate and large tunnelling strengths, the filling time shows a significant increase when the left and right reservoirs start out of phase. This reflects the fact that atoms tunnelling onto the depleted site can hop to adjacent sites if there is a phase gradient $\Delta\Theta_0$, keeping the occupation $N_{j=0}$ low. The system therefore remains macroscopically self-trapped, which further inhibits the bosonic enhancement that occurs for wells with comparable, large, atom numbers. This is highly suggestive of dark soliton formation.

8.2.2 Dark soliton and its breakdown

Of particular interest are the trajectories starting with an initial phase difference close to π. An exemplary simulation is displayed in Fig. 8.4(a), where the evol-

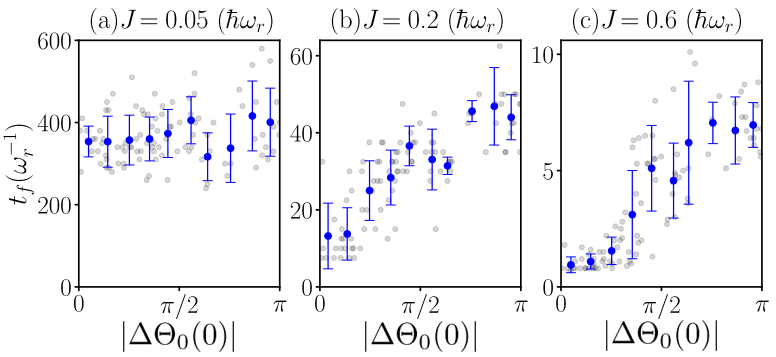

Figure 8.3 – Refilling times t_f in individual trajectories in function of the (random) phase difference between the two neighbouring wells. Three different values of the tunnelling strength are shown. Figure reproduced with permission from Ref. [56].

ution of the population on the central well, N_0, is plotted in time together with $|\Delta\Theta_0|$. It shows a single trajectory in the TWA formalism with $|\Delta\Theta_0(t=0)| \approx \pi$, which corresponds approximately to an individual experimental run [81]. The phase difference can be seen to remain locked at $|\Delta\Theta_0| \sim \pi$ until close to the time at which the density has grown significantly. The robustness of a soliton-like excitation over these timescales is supported by the slow change in density compared to cases with smaller phase differences; see Ref. [56] for details. The rate of change in the density is given by

$$\frac{\mathrm{d}N_j}{\mathrm{d}t} = \frac{2J}{\hbar}\left(I_{j+1,j} + I_{j-1,j}\right), \tag{8.9}$$

where $I_{k,j} = \int \mathrm{d}\mathbf{r}\ \mathrm{Im}[\psi_k^* \psi_j]$ is the current due to atoms flowing between site j and site k. Fig. 8.4(b) shows the contributions to the current from the respective driving wells, $I_{-1,0}$ and $I_{1,0}$, vs time. While the overall current remains small for some time, as seen by the slowly changing atom number in the panel (a), contributions from the individual driving wells oscillate with approximately equal magnitude but opposite sign. This is characteristic of the oscillatory instability for the on-site soliton, detailed in the previous section. The nature of the dominant decay mechanism is purely one-dimensional, despite the prominent radial size ($\mu_R > \hbar\omega_r$). In Sec. 8.4, we go into more detail about the nature of the instability. We conclude now that for experimentally relevant parameters the effect of the radial extension on the instability of the dark soliton is negligible. The result does however confirm that the vicinity to the soliton phase causes an increase in filling

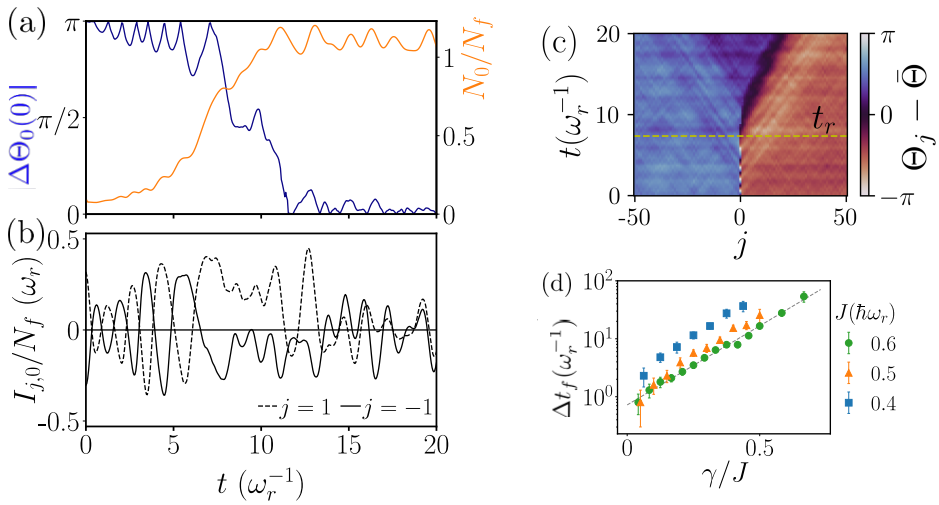

Figure 8.4 – (a) Evolution of the phase difference between driving wells $|\Delta\Theta_0(t)|$ (left axis) and normalized density N_0/N_f on the lossy site (right axis) in time. (b) Time evolution of the contributions to the current into the central well from the respective driving wells, $I_{1,0}$ and $I_{-1,0}$ (shown normalized by N_f). (c) Colour plot showing the evolution of the spatial phase profile in time. The mean phase $\overline{\Theta}$ is subtracted for ease of visualization, and the yellow dashed line indicates the relaxation time t_f of the lossy site. Data in (a), (b) and (c) corresponds to a single trajectory with initial $\Delta\Theta_0(0) \approx \pi$ and $\gamma = 0$. (d) Trajectory-averaged relaxation time (lifetime) of the soliton as a function of dissipation strength γ shifted by the dissipationless result, $\Delta t_f = t_f - t_f(\gamma = 0)$. Error bars indicate standard error from 10 samples. Results correspond to $J = 0.6\hbar\omega_r$, $g_{2D} = 0.23\hbar\omega_r$ with $L = 101$ sites.

time.

Fig. 8.4(c) shows the evolution of the corresponding spatial phase profile as a function of time. At approximately the time in which the central well becomes full (yellow dashed line), the location of the π phase jump becomes unstable and its boundary propagates ballistically in a spontaneously chosen direction (selected by quantum noise) at the sound velocity, seeding resynchronisation of the phase.

Finally, the continuous loss process is added back into the mix. In Fig.8.4(d) we present the relaxation time, t_f, as a function of γ, which was kept zero up until now. It can be seen that the relaxation time diverges exponentially with γ as $\Delta t_f = t_f - t_f(\gamma = 0) \propto 10^{6.28\gamma/J}$, indicating that for fixed J the soliton becomes

stable at sufficiently high dissipation rates. It is observed from the numerical simulation that if the system is initialized with a random phase at either side of the empty site, the phase difference generally quickly relaxes to $|\Delta\Theta_0| \approx \pi$. Therefore, while we initialize the system with a random phase difference over the central well to mimic the experimental procedure, the soliton becomes relevant almost immediately.

8.2.3 Steady-state phase diagram

We now construct the phase diagram as a function of the tunnelling amplitude J and dissipation strength γ by solving Eq. (7.3) in the TWA for a system of $L = 250$ lattice sites. Similar to the experimental protocol, we consider the state of the system at $t = 80$ms, starting from two different initial states: the initially empty central well and the initially full central well respectively. Fig. 8.5(a) shows the atom number difference $|\Delta N|$ between these two scenarios in parameter space. A significant $|\Delta N|$ implies that the state is dependent on the initial condition - therefore indicating bistability. Results are compared to the experimentally obtained phase boundaries from Ref. [48], displayed by the squares (upper boundary) and circles (lower boundary). Our simulations can be seen to match the experimental data very well at the upper boundary (large J), where the soliton transitions to a uniform superfluid. This has not been captured by prior works without numerous additional assumptions [53].

In order to highlight the role of the soliton, Fig. 8.5(b) displays analogous results for a system where the soliton formation is impeded by imposing mirror symmetry around the dissipative site. This restriction ensures there is a conventional optical bistability [48, 53, 141]. Clearly, the upper boundary in this case strongly differs from the experimental data. Soliton free simulations predict a transition at *lower* J values than the one that is experimentally observed, which is especially hard to reconcile. While a lowering of the upper boundary can be possibly attributed to thermal and quantum fluctuations, it is much harder to account for an increase of the hysteresis area. This is a strong indication that the experimentally probed state on the lower branch is not symmetric, but rather the anti-symmetric dark soliton. We conclude that the spatial phase structure of the sites neighbouring the lossy site plays a crucial role in the observed bistability.

Notably, both phase diagrams differ significantly from the experimental data at the lower boundary. While theoretically this boundary is predicted to follow $J = \hbar\gamma/4$, experimental results indicate a much steeper linear relation, $J = \hbar\gamma$. However, it

is our judgement that this discrepancy is due to the experiment [48] suffering a finite-size effect. A large density on the central well, $N_0 \approx N_f$, equals a large drain of the system. In order to hold the quasi-steady state during the entire transient of 80ms, the number of highly-occupied reservoir sites in the array therefore has to be large enough. A rough estimate based on the sound velocity in the lattice, $c = \sqrt{2J\mu}$, indicates that this would require $L \geq 200$. However, the experiment from which we plotted the data here was performed on a smaller cloud; around 45×10^3 atoms corresponding to an array of approximately 65 sites containing $N_f = 700$ particles. In this case, the dissipation has time to reduce the atom number of all sites substantially, lowering the interaction energy and making it easier to switch to the soliton state. The experimental data points plotted in blue in Fig. 8.5 therefore no longer accurately portray the phase boundary of the bistable regime. An initially empty well prevents substantial atom losses, meaning the ensuing dynamics is far less affected by finite-size effects.

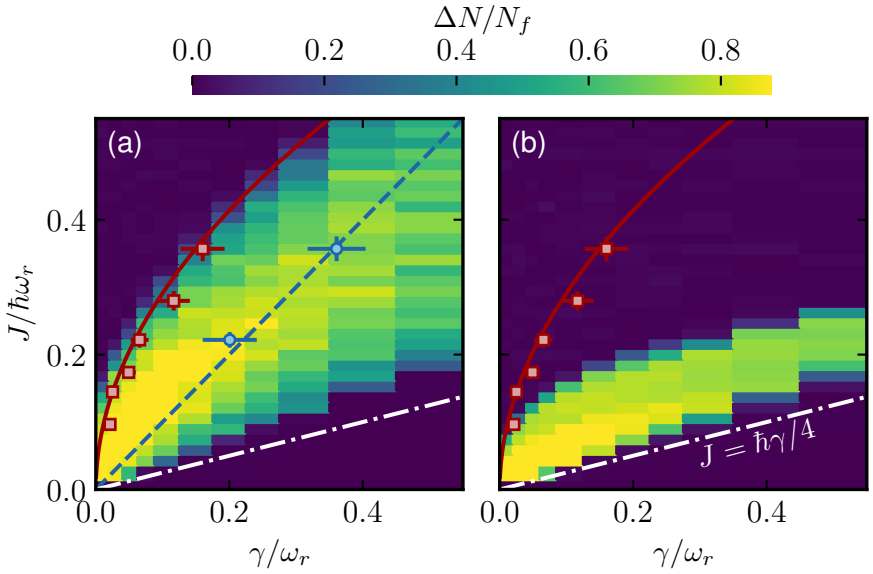

Figure 8.5 – (a) Phase diagram as a function of tunneling amplitude J and dissipation strength γ, indicating the late time (normalized) atomic population difference ΔN between simulations starting from different initial states: the empty and full central wells respectively. A finite ΔN indicates a bistable regime. The experimental phase boundary from Ref. [48] is displayed with points and a fit $J \sim \sqrt{\gamma}$. (b) Same, for a system with imposed mirror symmetry around the central well, which is incapable of hosting a dark soliton. Displayed data corresponds to $t = 80$ ms and 250 lattice sites, with 64 trajectories for each point.

8.3 Dissipative phase transition: optical vs soliton bistability

Having made clear in the previous section that the soliton is able to persist in the 3D geometry over long time-scales, even in the absence of localized loss, we now turn to discussing how this impacts the bistability first-order phase transition. As pointed out above, even in the full 3D setting, it is the *sloshing* mode, i.e. the oscillatory instability of the discrete dimension, which constitutes the dominant decay mechanism. A qualitative picture is therefore already obtained from a 1D Bose-Hubbard model where the transverse dynamics are neglected.

8.3.1 Critical loss rate

As we know from Chapters 5 and 6, the (quasi) steady states observed at finite times can already be understood from mean-field predictions for large occupations. In Chapter 6 the mean-field analysis was already performed for the case of the left and right half chains driving in sync. Here, both steady states are symmetric. In the absence of this restriction the system displays a bistability between the superfluid phase and an anti-symmetric dark soliton, a dark state of the Liouvillian. A direct comparison of the two types of bistability is presented in Fig. 8.6(a). In the soliton bistability the density on the central well $|\psi_S|^2$ remains perfectly zero over the whole lower branch. The hysteresis surface is clearly much larger when the soliton is allowed to form, indicated in the figure by the hatched area. While the dark soliton is always a solution of the mean-field equations, it is the change in its stability that determines the boundary of this bistability region.

In order to probe the dynamical stability of the dark state we analyse the eigenvalues of Bogoliubov excitations on top of the dark soliton state, i.e. we numerically solve the set of equations

$$\begin{aligned} \omega_l u_{j,l} &= (-2J + 2U|\phi_j|^2 - \mu - i\gamma/2)u_{j,l} + \phi_j^2 v_{j,l} - J\left(u_{j-1,l} + u_{j+1,l}\right), \\ \omega_l v_{j,l} &= -(-2J + 2U|\phi_j|^2 - \mu + i\gamma/2)v_{j,l} - \phi_j^2 u_{j,l} + J\left(v_{j-1,l} + v_{j+1,l}\right), \end{aligned} \tag{8.10}$$

where ϕ_j is given by Eq. (8.7). Fig. 8.7(b) shows the complex eigenvalues ω_l with largest real part for $J/\mu = 0.18$. These are shown to have $\max\left(\mathrm{Im}[\omega_l]\right) < 0$ for $\gamma_c^{mf} < \gamma$, which implies that the modes are damped and that the soliton (8.7) is a stable fixed point, acting as an attractor in the dynamics. For $\gamma < \gamma_c^{mf}$, a pair of complex eigenvalues cross the real axis, indicating unstable modes and constituting

a *Hopf bifurcation*. In comparison, optical bistabilities have been shown to cause saddle node bifurcations [124]. The absence of a stable limit cycle for $\gamma < \gamma_c^{mf}$ indicates that the bifurcation is subcritical, leading the system to settle in the stable superfluid state further away.

Adding single-particle losses to the site that corresponds to exactly zero density in the soliton profile thus acts as a drain of fluctuations effectively stabilizing this excited state and holding it in place indefinitely. Changes in the instability growth rate, $\max[\mathrm{Im}(\omega_l)]$, as a function of losses are illustrated in Fig. 8.7(c). Here, we compare finite-size systems with the 1D thermodynamic limit in the form of the reservoir model introduced in Sec. 6.2.2. One can distinguish two regimes. At first, the growth rate decreases independently of system size, but at the tipping point the curves branch off. At this point the remaining instability is a finite size effect. Excitations brought about by the defect at the centre, the imaginary potential, can not leave the system but reflect from the hard-wall boundaries and destroy the excited state. Because of this, the soliton lifetime increases with a growing size L at a fixed value of γ in this second regime. These excitations will eventually be suppressed at larger loss rates as well, rendering the soliton truly stable. In the thermodynamic limit this effect is absent, and the instability quickly diminishes just right of the tipping point, leading to the critical loss rate $\gamma_c^{mf}(J)$. One can see in Fig. 8.7 how a growing system size approaches the thermodynamic limit better.

We associate this stabilisation with a Zeno-like effect. The quantum-Zeno effect refers to the suppression of coherent Hamiltonian dynamics by a continuous, (non-)ideal measurement [66]. The dark soliton, that we can intuitively regard as a particle with negative mass, is initially highly localized around the position q. The initial wave packet would in a continuous setting spread out due to quantum fluctuations [188, 192]. The oscillatory instability, however, has a similar effect for the discrete classical analogue in [193]. The linear loss term can be regarded as a continuous indirect measurement of the density at the central site. It prevents the spreading of the wave packet and keeps it localized to the centre. In other words it inhibits the internal dynamics, the onset of the oscillatory instability. The possibility of stabilizing dark solitons through local dissipation in the continuous counterpart of this setup has also been demonstrated theoretically [60, 194].

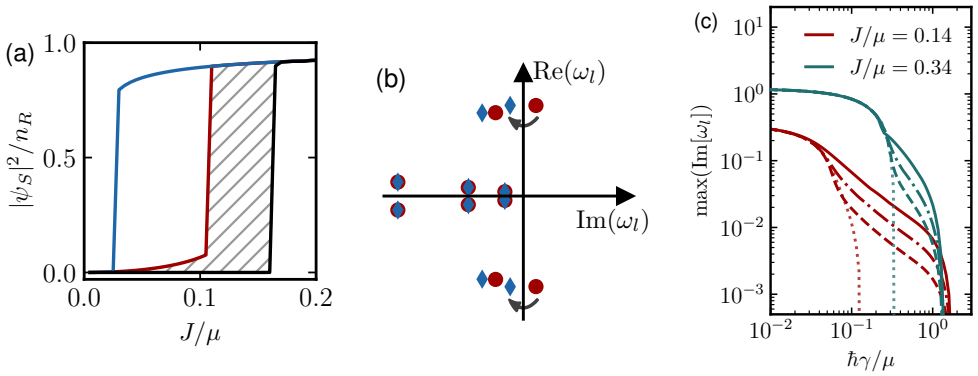

Figure 8.6 – Stabilisation through losses, a Zeno-like effect. (a) Comparison of the *regular* bistability that resembles an optical resonator (coloured lines) vs. the soliton bistability (black line). The hatched area indicated the difference in surface of the hysteresis loop. (b) Map of the eigenvalues of discrete dark soliton (8.7) in the dissipative Bose-Hubbard model. This excited state is dynamically unstable for $\gamma < \gamma_c$ (red), but becomes a stable fixed point after crossing the bifurcation point (blue). (c) Imaginary value of the pair of unstable modes as a function of γ (log-log scale). Different line styles indicate different system sizes; respectively $L = 101$, 201 and 401 for the full, dash-dotted and dashed line. The dotted line illustrates the thermodynamic limit that was effectively realised with the incoherently pumped model introduced in Sec. 6.2.2.

8.3.2 Liouvillian gap

We continue to investigate the first-order phase transition that underlies the observed hysteresis (in the thermodynamic limit). At the mean-field level, the soliton is a dark state[1] of the dissipative time evolution, a state where particles are no longer emitted. Quantum fluctuations prevent, however, a true dark state. In the TWA for example, noise from the connection to the environment will lead to a small occupation of the vacuum in the centre in the individual stochastic trajectories. This can be enough to destroy the mean-field stability even when $\gamma \gtrsim \gamma_c^{mf}$. Just like in Chapter 6, including quantum fluctuations induces switching between the previously stable states on a much longer timescale. This eventually drives the system towards detailed balance between the two metastable states.

In Fig. 8.7(a) we present the effective Liouvillian gap λ, derived in the TWA[2], as a function of tunnelling J at a fixed loss rate $\gamma = 2$. We compare the results of

[1] Sometimes referred to as absorbing state as well.
[2] For details on the derivation of λ we refer back to Sec. 6.3.

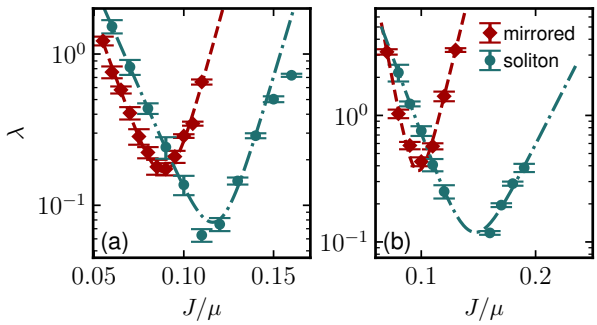

Figure 8.7 – Effective Liouvillian gap as a function of the tunnelling strength at dissipation rates $\gamma = 2.0$ (a) and $\gamma = 3.0$ (b). Hysteresis is a consequence of the closing of the gap around a critical value. Results are compared to those obtained with imposed mirror-symmetry (red diamonds), which excludes the possibility of a soliton.

the full chain with those of the system with imposed mirror-symmetry around the lossy site. The latter excludes the formation of a soliton and displays the regular optical bistability. The minimum gap, which indicates the transition point, is seen to be lower for the soliton-superfluid transition. This can be attributed to the different nature of the transition. In regular, optical bistability (red curves) the transition is localized to the single well that is subject to losses. Switches in separate trajectories, triggered by the dynamic noise and by fluctuations in the reservoirs, only need a change in the field of one well. However, in order to switch from a soliton to the upper branch the phase of the entire reservoir on the left or right has to be flipped by π. A switch involves a much larger region in space and is therefore more suppressed.

The curve also broadens significantly for the soliton-superfluid transition, which reflects a wider region around the minimum that is affected by critical slowing down. This difference between the simulations with and without soliton increases as the loss rate γ grows, as shown in Fig. 8.7(b). Most notably, while optical bistability sees a closing of the region of bistability with increasing γ [61], the opposite seems to hold for the soliton bistability. This is in agreement with the experimentally relevant phase diagram, Fig. 8.5(a)-(b).

8.4 Soliton in higher dimensional settings

The question remains why the finite radial size of the Josephson array does not lead to a transverse modulation of the planar dark soliton, the famous *snake instability*. Generally, the dynamical stability of a planar dark soliton in a cylindrical trap geometry depends on the radial size. In the absence of a lattice potential, the soliton is stable for a transverse size under a certain critical radius R_c [195], but decays to a soliton train when $R > R_c$. The onset of instability at the critical length is accompanied by the solitonic vortex that becomes energetically favourable [196]. This single confined vortex with solitonic properties is the smallest unit of decay. With increasing radial size the soliton plane decays in an increasing number of vortices. In a recent theoretical study by Baals *et al.* [197], the dark soliton was shown to decay to a solitonic vortex in the continuous equivalent of the Josephson-array experiments. Here, we will determine the effect of a lattice potential on the snaking instability.

8.4.1 Snaking instability

Let us consider in the mean-field framework a 3D Bose gas trapped in a box potential with an additional 1D periodic potential along the z-axis. Dimensions of the box in which the gas is trapped are given by $\{L_x, L_y = L_x, L_z = N_z d\}$, i.e. the system is isotropic in the transverse directions. The GPE for the matter field inside the box potential is given by

$$i\hbar\frac{\partial\psi_j(\mathbf{r},t)}{\partial t} = \left[-\frac{\hbar^2\nabla_{\mathbf{r}}^2}{2m} + g_2|\psi_j|^2 - \mu\right]\psi_j - J\left(\psi_{j-1} + \psi_{j+1} - 2\psi_j\right), \tag{8.11}$$

while it is trivially zero outside. Due to the translational invariance in the transverse direction, the soliton in the discrete direction ϕ_j given by Eq. (8.7), is also a solution of the 3D system. The intrinsic length scale in the transverse direction is the healing length $\xi = \hbar/\sqrt{m\mu}$, where $\mu = g_2 n_\infty$ with n_∞ the bulk density. Without loss of generality, excitations in the transverse plane can be represented as plane waves:

$$\psi_j(\mathbf{r},t) = \phi_j + \sum_l u_{j,l}e^{-i(\omega_l t - \mathbf{k}\cdot\mathbf{r})} + v_{j,l}^* e^{i(\omega_l^* t - \mathbf{k}\cdot\mathbf{r})}. \tag{8.12}$$

Decoupling of the radial degrees of freedom results in the relatively simple set of BdG equations for each normal mode

$$\omega_l u_{j,l} = \left[\epsilon_k - 2J + 2g_2|\phi_j|^2 - \mu\right] u_{j,l} + \phi_j^2 v_{j,l} - J\left(u_{j-1,l} + u_{j+1,l}\right), \tag{8.13}$$

$$\omega_l v_{j,l} = -\left[\epsilon_k - 2J + 2g_2|\phi_j|^2 - \mu\right] v_{j,l} - \phi_j^2 u_{j,l} + J\left(v_{j-1,l} + v_{j+1,l}\right), \tag{8.14}$$

where the free particle energy $\epsilon_k = \hbar^2 k^2/2m$ depends solely on the radial wavenumber $k = \sqrt{k_x^2 + k_y^2}$. From the eigenvalues we determine the fastest growing unstable modes as a function of k. In order to better understand the decay mechanisms we also determine the nature of the instabilities by introducing the following fields

$$P_j = \frac{u_j + v_j}{2}, \tag{8.15}$$

$$Q_j = \frac{u_j - v_j}{2i}. \tag{8.16}$$

These relate respectively to the density and phase fluctuations of the order parameter in the linearized theory. From the norm of both fields we can then determine whether an unstable eigenmode has rather a phase or a density character by introducing the mixing parameter [198]:

$$\eta = \frac{\sum_j |P_j|^2}{\sum_j |P_j|^2 + |Q_j|^2}. \tag{8.17}$$

This parameter is confined to the range $0 \leq \eta \leq 1$ where the boundaries represent a pure phase or amplitude nature of the mode, respectively.

As indicated above, the continuum limit is reached when $J/\mu \gg 1$. In this limit the regular snaking instability is recovered, illustrated in Fig. 8.8 for $J/\mu = 5$. The effect takes its name from the typical transverse density modulations that in 2D look like a snake and unavoidably leading to the breakdown of the dark soliton into a sequence of vortices. In the 2D case that is illustrated here, the line soliton transitions to a vortex train, whereas a planar soliton would decay to stable vortex rings [185]. The Bogoliubov spectrum shown in Fig. 8.8(a) is intimately linked to this phenomenon [195, 199]. The maximum growth rate is characterized by a linear dependence $\mathrm{Im}\left[\omega(k)\right] = k\xi/\sqrt{3}$ at small momenta (dashed line), a peak at $k\xi = 1/\sqrt{2}$ (dashed line) and eventually a decrease to the critical point $k_c\xi = 1$. The instability originates from the transfer of kinetic energy, related

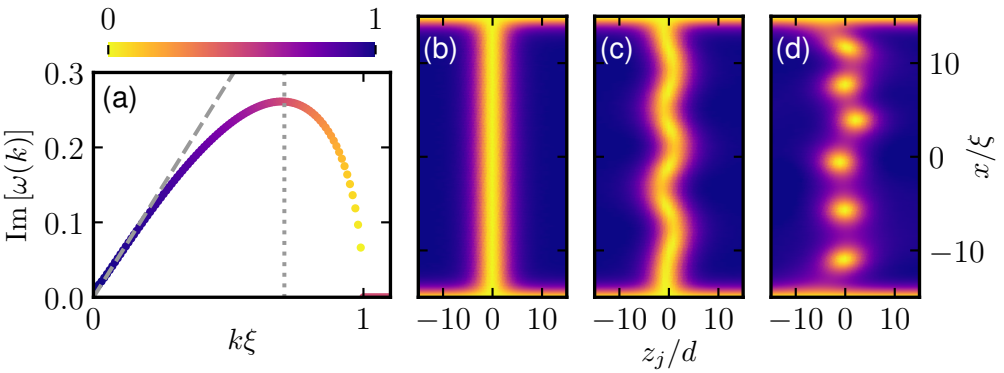

Figure 8.8 – Snaking instability in the continuum limit, specifically $J/\mu = 5$. (a) Imaginary part of the eigenenergies of unstable modes in relation to the transverse momentum. The colors indicate the value of η as defined in Eq. (8.17). (b)-(d) Snapshots of the normalized density $|\psi_j(x)|^2/n_\infty$ around the soliton line in a 2D numerical time evolution at respective times $t/\mu = 13,\ 36,\ 59$. The initial state is a slightly-perturbed stationary line soliton obtained through imaginary time evolution of the GPE. Here, we took $L_x = 30\xi$, with a spatial resolution of $\Delta x = 0.1\xi$.

to the density dip, to the radial modes. The transverse motion energy $\hbar^2k^2/2m$ exceeds the soliton energy for $k > 1$ making the modes above the critical point dynamically stable. Given a transverse size L_x, the smallest momentum mode corresponds to $k = 2\pi/L_x$. One can see that for very small system sizes, $L_x \lesssim 6\xi$, no unstable modes are possible.

Colours of the points in Fig. 8.8(a) indicate the value of the mixing parameter η for that unstable mode. With increasing wavenumber the unstable modes go from being fully amplitude-like to fully phase-like. The $k = 0$ amplitude mode $\delta\psi \propto \Delta z \partial_z \psi_s$ is consistent with a uniform displacement of the soliton line, whereas the magnitude of displacement varies periodically in x and y for finite k, leading to the typical snaking. The fastest growing mode at $k\xi = 1/\sqrt{2}$ has both an amplitude and a phase nature. Its phase component leads to local currents at the soliton core causing its breakdown into a vortex train. One can assume this mode to be the dominant mode to manifest in the dynamics shown in Fig. 8.8(b)-(d).

8.4.2 Continuous to discrete crossover

In the opposing limit, $J/\mu \lesssim 1$, the width of the kink becomes comparable to the lattice spacing and the soliton becomes aware of the discreteness in the z-direction. Where the difference between the link and site soliton is negligible in the continuum limit, very different behaviours are observed in the discrete regime. We start by treating the site soliton, which is most relevant for our work, but also consider the link soliton for the sake of completeness.

Site soliton

In Fig. 8.9, we present the growth rate spectra for decreasing values of J. As the tunnelling strength is reduced, the first notable change occurs at long-wavelengths, where the previously unstable amplitude modes become stable. This effect can be attributed to the Peierls-Nabarro barrier [189], emerging due to a growing energy difference between site and link solitons. As J decreases, the PN barrier grows, leading to a greater excess in energy of the site soliton compared to the link soliton. This excess prevents coupling to the lowest-energy transverse modes, thereby shifting the minimum wavenumber k of the radial modes through which the SS can decay. The nature of the fastest-growing instability remains unchanged at first, but it shifts to slightly shorter wavelengths, resulting in more bends along the soliton line over the same length. This trend is reflected in the top row of Fig. 8.10, where at $J/\mu = 0.6$ the soliton breakdown results in one more vortex compared to the benchmark at $J/\mu = 5$.

As tunnelling is reduced even further, a new branch of unstable modes emerges at the lower end of the spectrum and eventually becomes the dominant decay mechanism. These modes, which features a non-zero real part not reflected in the figure, correspond to the oscillatory instability characteristic of the 1D discrete soliton. For each value of k, this instability is primarily phase-like. Since the largest growth rate in panels (c) and (d) occurs at finite k, the dominant decay mechanism remains spatially periodic. The bottom row of Fig. 8.10 illustrates how alternating currents fill up the kink without the signature snaking pattern. In this regime, vortex nucleation is completely absent and the soliton gradually dissipates.

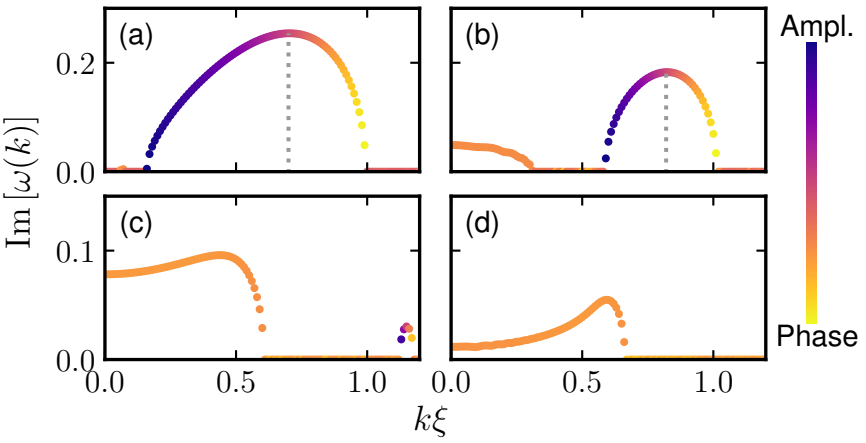

Figure 8.9 – Growth rate spectra $\mathrm{Im}\,[\omega(k)]$ for an on-site soliton at different tunnelling strengths $J/\mu = 1.25$, 0.6, 0.2 and 0.1 respectively. The colour of each point denotes the value of η, defined by Eq. (8.17), indicating the nature of that instability.

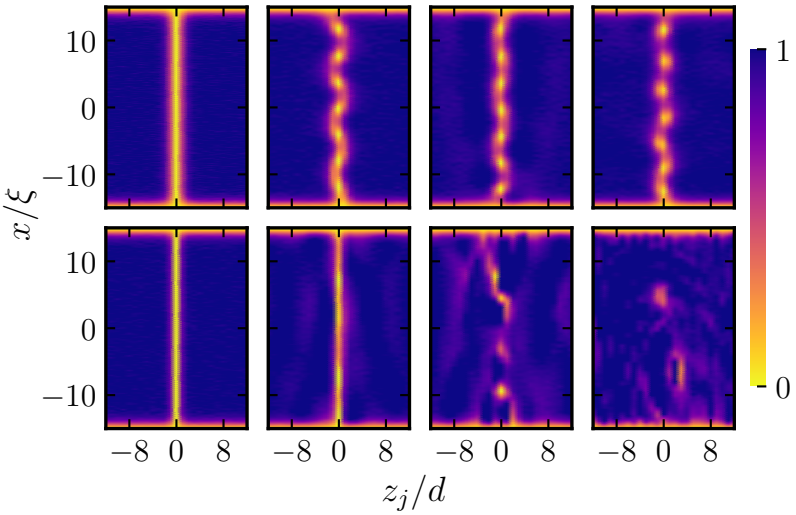

Figure 8.10 – Decay of the site soliton in real-time. On the top row, the relative density $|\psi_j(x,t)|^2/n_\infty$ is displayed for a tunnelling $J/\mu = 0.6$ at evolution times $t/\mu = 1$, 35, 43 and 59. On the bottom row, slightly different times are shown ($t/\mu = 20$, 60, 75 and 99) for $J/\mu = 0.2$.

Link soliton

The instability dynamics of the link soliton is quite different, as reflected by the change in the growth rate spectra presented in Fig. 8.11. As the soliton width lessens, several effects can be observed. Low momentum modes become increasingly unstable, leading to enhanced long-wavelength modulations that overlay the usual snaking. This effect is evident from the real time evolution in the top row of Fig. 8.12. Additional density modulations cause some of the vortices to be expelled from the previously stable vortex line. Deep in the anti-continuum limit, unstable modes become predominantly phase-like over the entire domain. The dominant decay mode shifts to $k = 0$, corresponding to a uniform modulation of the depletion plane. In this regime, vortex nucleation occurs at short times without the typical snaking. Instead, currents varying over the xy-plane with long periods result in a single vortex being formed. Simultaneously, the critical point k_c shifts to lower values, indicating a growing transverse size below which the dark soliton remains stable. This result is particularly relevant for experimental realizations.

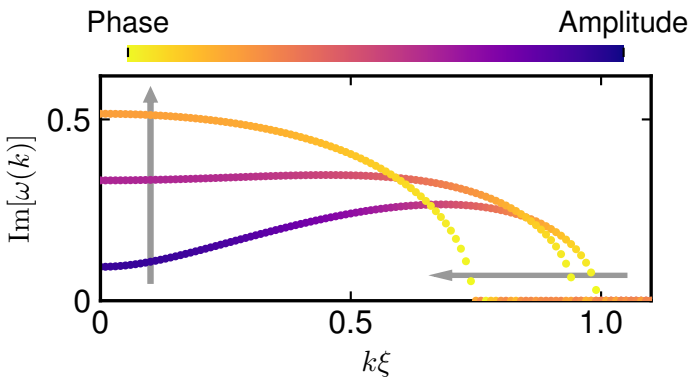

Figure 8.11 – The maximum growth rate as a function of the transverse wavenumber k for a link soliton at different tunnelling strengths J/μ =1.25, 0.6, and 0.25. Arrows indicate the decrease of J. The colour of each point denotes the value of η, defined by Eq. (8.17) and ranging from 0 (phase) to 1 (amplitude), indicating the nature of the unstable mode.

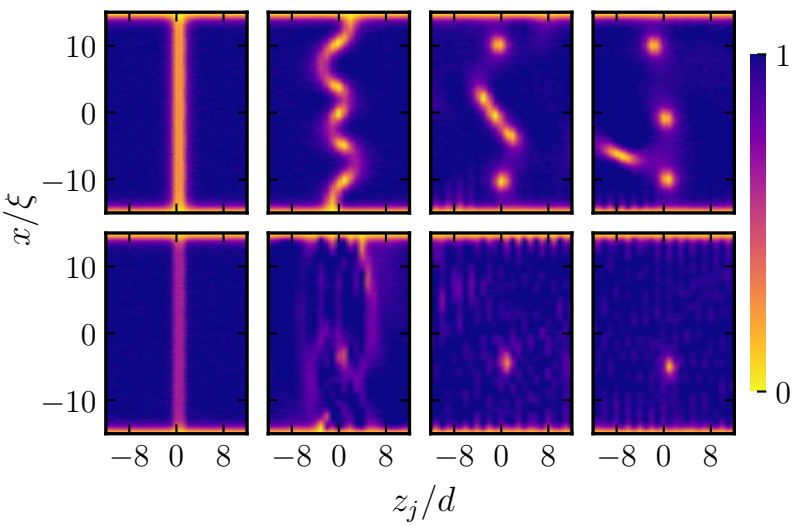

Figure 8.12 – Decay of the link soliton through snapshots of the 2D density $|\psi_j(x,t)|^2/n_\infty$ at evolution times $t/\mu = 5$, 26, 48 and 70 (from left to right). The two rows correspond respectively to $J/\mu = 0.6$ and $J/\mu = 0.25$.

8.5 Conclusion & outlook

In this chapter the impact of the standing dark soliton on a (quasi-) 1D Josephson array has been investigated by means of numerical simulations. After a brief introduction of some of the key properties of dark solitons in the 1D continuous and discrete non-linear Schrödinger equations, the experimentally relevant array of 2D trapped BECs was considered. Where a previous theoretical study had already indicated the importance of the phase difference between the reservoir sites, it was conclusively shown here that it is the possibility to form a standing dark soliton that drastically alters the out-of-equilibrium dynamics. Although the discrete soliton is dynamically unstable in the closed system, its slow decay rate significantly enhances the refilling time. Furthermore, we identified the mechanism behind the decay to be the oscillatory instability characteristic of the discrete soliton in 1D, acknowledging the quasi-one-dimensional nature of the experiment. Adding a local loss process at the central well is shown to stabilise this exotic state through a Zeno-like effect. Consequently, the bistability that naturally follows is altered significantly. For the first time the experimental phase diagram was reproduced from first principles modelling, confirming also here the impact of the soliton formation. One question on the nature of the discrepancy of the lower

boundary in the phase diagram remains open. A more thorough understanding of the experimental protocol might deliver more insight here.

Next, a qualitative understanding of this new type of bistability was provided through numerical analysis of the dissipative Bose-Hubbard model. We showed that the bistability can be related to a different type of bifurcation. Widening of the bistability regime was analysed by means of the Liouvillian gap and was ascribed to a suppression of fluctuations. Where the phase transition was conventionally regarded as a local change in the central well, we concluded here that it actually affects a larger region of the system surrounding the dissipation.

The results of this chapter are interesting in themselves as they shed new light on the experimental observations, but they also trigger a number of ideas for follow-up studies. A natural continuation of the dissipative Bose-Hubbard chain would be a square grid, realised by two perpendicular lattice potentials. The question can be asked whether the phenomena observed in 1D carry over to two dimensions. Would a vortex, the 2D equivalent of a dark soliton, naturally follow from the experimental protocol in the same way as the soliton and does a similar phase transition between a vortex and a superfluid occur? This would be particularly interesting due to a vortex (in a continuous medium) being topologically protected, unlike the 1D soliton.

In Chapter 6 we already pitched the idea of realising multistability in binary mixtures, but limited our calculations to mean-field simulations where fluctuations are lacking. Given the results from this chapter, an even richer phase diagram is to be expected in the presence of quantum fluctuations. The additional spin degree of freedom in this setup might lead to even more complex topological structures like half-solitons, that feature a soliton in only one of the two components.

Part III

Conclusions

CHAPTER 9

General conclusions and outlook

In this thesis we performed a theoretical and computational study of the dissipative Josephson array, a configuration of ultracold atomic gases loaded into a 1D optical lattice potential and subject to a very precise, external loss process. Motivation for this study is found in a number of intriguing experimental observations in this setup. At first glance, these properties greatly resemble those of the non-linear Kerr resonator, a relatively simple archetype system from the field of quantum optics. Our work has shown, however, that the atomic system is subject to increased complexity and even richer physics than originally assumed.

First, the complementary problem of the dissipative Bose-Hubbard model was regarded, which neglects transverse degrees of freedom of the experimental configuration. Isolating the lattice dynamics allowed us to focus on the main features of this system. The non-equilibrium steady-states and bistability were studied in the mean-field limit and compared to an effective model. This model, that incorporates elements from the description of polariton condensates, was shown to capture the physics on a mean-field level very well. Interestingly, both models indicated the prevalence of an additional phase of the system not observed experimentally, a dark soliton. A more accurate representation was obtained in the truncated Wigner approximation. Through the derivation of the Liouvillian gap the unique steady-state density matrix of the lossy mode was reconstructed. Additionally, a similar configuration for a binary mixture was considered and demonstrated a regime of multistability, in analogy to spin multistability with microcavity polari-

tons.

The qualitative agreement with a laser driven cavity suggests that the atom cloud in the lossy well would contain a significant condensate fraction even at low densities. In the next chapter, coherence properties in the central well were studied by including transverse degrees of freedom of each well in the array. Investigation of the first and second order correlation functions revealed the presence of a significant condensate fraction in what was assumed to be the normal state. The non-equilibrium steady-state is characterized by large occupation of one eigenstate, closely related to an excited single-particle state.

Finally, in the last chapter a more thorough investigation of the dark soliton state is performed. A brief introduction summarizes the properties of the state, focussing on the characteristics in a discrete setting. These are of key importance in recognizing the one dimensional excited state in the three dimensional setting. It was shown that the standing soliton not only easily persists in the configuration, but that it is crucial in order to obtain quantitative agreement with the experimentally observed phase diagram. Due to the presence of a dark soliton we observe a growing region of bistability with increasing dissipation strength, as opposed to the regular optical bistability. This is features in the Liouvillian gap closing as well. It indicates a novel type of bistability between a dark state of the system and the superfluid state. Lastly, a stability analysis is performed to better understand the decay mechanisms of the dark soliton in systems with a significant radial size.

As a general conclusion we can say that the dissipative Josephson array displays even more interesting behaviour than originally assumed. Our approach, starting from a simplified representation and building up complexity, has greatly contributed to the better understanding of this system and the uncovering of hidden features.

The research performed in this thesis naturally leads to a number of possible directions for future studies. The last part of Chapter 6 already introduced the possibility to expand the notion of bistability to more levels by regarding an additional spin degree of freedom. The treatment of a spin-1/2 or spin-1 version of the dissipative Josephson array with spin-dependent tunnelling seems feasible also from an experimental point of view. A more detailed understanding of the density matrix and how it behaves under variation of the polarization could be obtained in combination with a theoretical treatment in the TWA. Taking into account the

results from Chapter 9, the spinor case becomes especially interesting. The observation of a soliton in the single component case suggests that 1D half-solitons will come into play in the spin system. Additionally, it would be interesting to consider higher-dimensional lattices for the regular, single-component gas. Would the same bistability physics manifest for example in a 2D lattice and if so is a vortex state reached as easily as the counterpart in 1D? Given that a vortex is topologically more robust, it is of significant interest to verify whether the novel type of dissipative phase transition we uncovered in this work is universal.

APPENDIX A

Numerical implementation

In this Appendix we outline in more detail the projected Gross-Pitaevskii formalism for a harmonically trapped system. The first section will deal with the differential equations that are solved, more specifically it will elaborate on how the correct interaction elements are calculated. In the second section, we briefly discuss how the model parameters are estimated from the details of the experiment.

A.1 Expansion in harmonic basis

Here, we further elaborate on the formalism used to accurately represent the dynamics of an harmonically trapped degenerate Bose gas, as it was reported in Refs. [89, 93]. To simulate a homogeneous Bose gas a plane-wave basis is an appropriate choice, but for trapped gases it is no longer sufficient. The optimal basis for expanding the (semi-)classical wave function is the one that diagonalizes the linear part of the Hamiltonian

$$\hat{H} = \int \mathrm{d}^2\mathbf{r}\ \hat{\Psi}^\dagger(\mathbf{r}) \left[-\frac{\hbar^2\nabla^2}{2m} + V(\mathbf{r}) \right] + \frac{g}{2} \int \mathrm{d}^2\mathbf{r}\ \hat{\Psi}^\dagger\hat{\Psi}^\dagger\hat{\Psi}\hat{\Psi} \tag{A.1}$$

for an isotropic, 2D harmonic trap $V(\mathbf{r}) = \frac{1}{2}m(\omega_x^2x^2+\omega_y^2y^2)$. Following the Projected GPE method, as described in Sec. 4.4, we neglect the field operator character $\hat{\Psi}(\mathbf{r}) \to \Psi(\mathbf{r})$, project onto the delineated coherent region $\psi(\mathbf{r}) = \mathcal{P}\{\Psi(\mathbf{r})\}$ and

solve the resulting GPE:

$$i\hbar\frac{\partial\psi(\mathbf{r},t)}{\partial t} = \mathcal{H}_{sp}\psi(\mathbf{r},t) + g\mathcal{P}\left\{|\psi(\mathbf{r},t)|^2\psi(\mathbf{r},t)\right\}, \tag{A.2}$$

where we can expand the classical coherent field as

$$\psi(\mathbf{r},t) = \sum_{n_x,n_y\in\mathcal{C}} c_{n_x n_y}(t)\alpha_{n_x}(x)\alpha_{n_y}(y). \tag{A.3}$$

The wave functions $\alpha_n(x)$ are harmonic oscillator eigenstates that satisfy

$$\left(-\frac{\hbar^2}{2m}\nabla_x^2 + \frac{1}{2}m\omega_x^2 x^2\right)\alpha_n(x) = \hbar\omega_x\left(n+\frac{1}{2}\right)\alpha_n(x) \tag{A.4}$$

and which are defined as

$$\alpha_n(x) = \left(n!2^n l_x\sqrt{\pi}\right)^{-1/2} e^{-x^2/(2l_x^2)}H_n(x/l_x). \tag{A.5}$$

Here, $H_n(u)$ denotes the n-th order *physicist's* Hermite polynomial and $l_x = \sqrt{\hbar/m\omega_x}$ is the harmonic oscillator length. The coherent region is given by

$$\mathcal{C} = \{n_x, n_y : \hbar\omega_x(n_x+1/2) + \hbar\omega_y(n_y+1/2) \leq E_{cut}\}. \tag{A.6}$$

For pedagogical purposes and to keep things notationally uncluttered, we work out the simulation procedure for a 1D system. Starting from the simple case

$$i\hbar\frac{\partial\psi(x,t)}{\partial t} = \left(-\frac{\hbar^2}{2m}\nabla^2 + \frac{m\omega^2}{2}x^2\right)\psi(x,t) + \mathcal{P}\left[g|\psi(x,t)|^2\psi(x,t)\right] \tag{A.7}$$

and substituting

$$\psi(x,t) = \sum_{n=0}^{\mathcal{N}_x} c_n(t)\alpha_n(x) \tag{A.8}$$

we find an equation for the time evolution of the expansion coefficients:

$$i\hbar\frac{\mathrm{d}C(t)}{\mathrm{d}t} = EC(t) + gF[C(t)]. \tag{A.9}$$

Here, $C \in \mathbb{C}^{\mathcal{N}_x+1}$ is an array of the elements c_n. The interaction term can be

worked out explicitly:

$$\begin{aligned} F_n[C(t)] &= \int_{-\infty}^{\infty} dx\ \alpha_n^*(x)|\psi(x,t)|^2\psi(x,t) \\ &= \sum_{k,p,q=0}^{N} c_k c_p^* c_q \int_{-\infty}^{\infty} dx\ \alpha_n^*(x)\alpha_k(x)\alpha_p^*(x)\alpha_q(x) \\ &= \sum_{k,p,q=0}^{N} c_k c_p^* c_q I_{nkpq}. \end{aligned}$$

First we focus on the integral over real space I. From the definition of the eigenfunctions in (A.5) we find that

$$I_{nkpq} = \int_{-\infty}^{\infty} dx\ Q(x/l_x)e^{-2x^2/l_x^2} = \frac{l_x}{\sqrt{2}}\int_{-\infty}^{\infty} du\ Q(u/\sqrt{2})e^{-u^2}, \tag{A.10}$$

the function $Q(x)$ is the product of Hermite polynomials and is therefore itself a polynomial of order $n \cdot k \cdot p \cdot q \leq 4\mathcal{N}_x$. The degree of the polynomial which we wish to integrate is bounded by four times the number of modes in the coherent region. As a consequence, every integral can be calculated *numerically exact* with a Hermite-Gauss quadrature of *only* $2\mathcal{N}_x$ points [200]. This means that for any set of indices

$$I_{nkpq} = \frac{l_x}{\sqrt{2}}\int_{-\infty}^{\infty} du\ Q(u/\sqrt{2})e^{-u^2} = \frac{l_x}{\sqrt{2}}\sum_{i=1}^{2\mathcal{N}_x+1} w_i Q(u_i/\sqrt{2}), \tag{A.11}$$

where u_i are the roots of the $2\mathcal{N}_x + 1$-th order Hermite polynomial and w_i the associated weights. Because of the factorization of the wave function in Eq.(A.3), in the case of a 2D system the double integrals with integrand $Q(x,y)e^{-(x^2+y^2)/4}$ can be split up into two integrals of the same shape as Eq.(A.11). Assuming an equal number of modes $\mathcal{N}$ in the coherent region for each dimension, the integrals can also here be calculated exactly with a 2D spatial quadratures grid of $4\mathcal{N}^2$ points. Substituting the result from Eq. (A.11) back in the expression for F_n we find

$$F_n[C(t)] = \sum_{i=1}^{2\mathcal{N}_x+1} \frac{l_x}{\sqrt{2}} w_i e^{2x_i^2/l_x^2}\alpha_n(x_i)|\psi(x_i,t)|^2\psi(x_i,t), \tag{A.12}$$

with $x_i/l_x = u_i/\sqrt{2}$. It is a clear advantage of this method that the numerical implementation does not require any further approximations. Although the solving scheme contains a transformation to a quadrature space and back, this method still

outperforms a general plane-wave approach with the added benefit of accurately time evolving all the modes included in the coherent region. The performance that we managed to achieve is partly due to the scheme presented here, but is also owed to the use of the Julia programming language [201]. More precisely the *DifferentialEquations.jl* package provides an extensive list of high-performance ordinary and stochastic differential equations solvers [202].

A.2 Estimation of the Bose-Hubbard parameters

In Chapter 2 the derivation of the Bose-Hubbard model through the expansion in the basis of Wannier states is described. In the *lowest band approximation* and the *tight-binding approximation* the model is completely defined by the tunnelling amplitude

$$J = -\int \mathrm{d}x\; w_0^*(x - x_j)\left[-\frac{\hbar^2\nabla^2}{2m} - V_0\cos^2(kx)\right] w_0(x - x_{j+1}), \tag{A.13}$$

and the on-site interaction strength

$$U = g\int \mathrm{d}z\; |w_0(z)|^4. \tag{A.14}$$

Here, we elaborate on the numerical estimation of these parameters from the experimental values of the lattice depth and lattice spacing. The Wannier functions are found through the inverse Fourier transform of the periodic Bloch functions:

$$w_n(x - x_j) = \frac{1}{\sqrt{L}}\sum_q^{BZ} e^{-iqx_j}\phi_{n,q}(x). \tag{A.15}$$

The Bloch functions are the eigenfunctions of the single particle Hamiltonian,

$$\left[-\frac{\hbar^2\nabla^2}{2m} - V_0\cos^2(kx)\right]\phi_{n,q}(x) = E_{n,q}\phi_{n,q}(x), \tag{A.16}$$

and can be expressed as $\phi_{n,q}(x) = e^{iqx}u_{n,q}(x)$. The function $u_{n,q}(x)$ contains the same periodicity as the lattice $V(x)$ so that it can be written as Fourier series

$$u_{n,q}(x) = \sum_j c_j^{(n,q)} e^{i2kjx}, \tag{A.17}$$

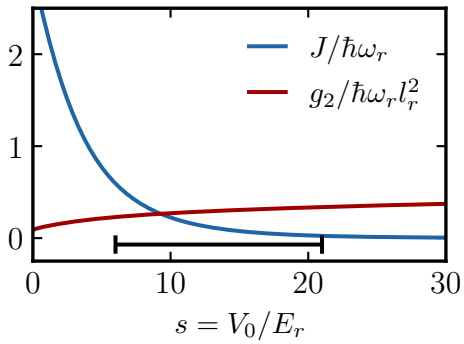

Figure A.1 – Estimation of the tunnelling J and 2D interaction strengths. Results are obtained by numerically evaluating Eqs. (A.13) and (A.14) respectively. The parameters are expressed in units of the radial harmonic oscillator. The black bar indicates the range of values for s achieved in the experiment of Ref. [50].

with $k = \pi/d$ en $j \in \mathbb{Z}$. Substitution in Eq. (A.16) results in

$$\sum_j \left[E_r(q/k + 2j)^2 c_j^{(n,q)} - \frac{V_0}{4}(c_{j-1}^{(n,q)} + c_{j+1}^{(n,q)}) \right] e^{i2kjx} = E_{n,q} \sum_j c_j^{(n,q)} e^{i2kjx}, \tag{A.18}$$

where the kinetic energy is given in terms of the recoil energy $E_r = \hbar^2 k^2/2m$. This can be further decoupled in a set of equations, one for each j, which can be written conveniently in matrix notation. For a given quasi-momentum q the solutions are found as the eigenvectors of the resulting tridiagonal matrix. The Bloch wave function of the n-th band can be determined from the eigenvectors $(\ldots, c_{j-1}^{(n,q)}, c_j^{(n,q)}, c_{j+1}^{(n,q)}, \ldots)^T$ which has a corresponding eigenenergy $E_{n,q}$. For the evaluation of Eqs. (A.13) and (A.14) only the lowest energy band is taken into account. In Fig. A.1 both tunnelling and interaction strengths are plotted as a function of the lattice depth $V_0 = sE_r$. These estimated values are applied for example in Chapter 8 to reproduce the experimental phase diagram. The chemical potential is approximated from the Thomas-fermi approximation:

$$\mu_R = \sqrt{g_2 m \omega_r^2 N/\pi}, \tag{A.19}$$

with $N = 700$.

Bibliography

[1] S. N. Bose. Plancks Gesetz und Lichtquantenhypothese. *Zeitschrift fur Physik.* **26**(1): 178–181, (1924).

[2] A. Einstein. Quantentheorie des einatomigen idealen Gases. *Sitzungsberichte der Preussischen Akademie der Wissenschaften.* **22**:261–267, (1924).

[3] A. Einstein. Quantentheorie des einatomigen idealen Gases. Zweite Abhandlung. *Sitzungsberichte der Preussischen Akademie der Wissenschaften.* **23**:3–14, (1925).

[4] C. Pethick & H. Smith. *Bose-Einstein condensation in dilute gases.* Cambridge University Press, Cambridge ; New York, (2002). ISBN 978-0-521-66580-3.

[5] H. T. C. Stoof, K. B. Gubbels, & D. B. M. Dickerscheid. *Ultracold quantum fields.* Theoretical and mathematical physics. Springer, Dordrecht ; New York, (2009). ISBN 978-1-4020-8763-9.

[6] P. E. Matthews, editor. *Bose Einstein Condensates: Theory, Characteristics, and Current Research.* Nova Science Pub Inc, Hauppauge, N. Y, (2011). ISBN 978-1-61728-114-3.

[7] L. Pitaevskii & S. Stringari. *Bose-Einstein Condensation and Superfluidity.* Oxford University Press, Oxford, UK, (2016).

[8] F. Dalfovo, S. Giorgini, L. P. Pitaevskii, & S. Stringari. Theory of Bose-Einstein condensation in trapped gases. *Reviews of Modern Physics.* **71**(3):463–512, (1999).

[9] D. Jaksch, C. Bruder, J. I. Cirac, C. W. Gardiner, & P. Zoller. Cold Bosonic Atoms in Optical Lattices. *Physical Review Letters.* **81**(15):3108–3111, (1998).

[10] I. Bloch, J. Dalibard, & W. Zwerger. Many-body physics with ultracold gases. *Reviews of Modern Physics.* **80**(3):885–964, (2008).

[11] C. Gross & I. Bloch. Quantum simulations with ultracold atoms in optical lattices. *Science.* **357**(6355):995–1001, (2017).

[12] A. Recati & S. Stringari. Coherently Coupled Mixtures of Ultracold Atomic Gases. *Annual Review of Condensed Matter Physics.* **13**(1):407–432, (2022).

[13] L. de Broglie. Recherches sur la théorie des Quanta. *Annales de Physique.* **10**, (1925).

[14] D. J. Griffiths & D. F. Schroeter. *Introduction to Quantum Mechanics.* Cambridge University Press, 3 edition, (2018). ISBN 978-1-107-18963-8.

[15] M. Born. Quantenmechanik der Stoßvorgänge. *Zeitschrift für Physik.* **38**(11):803–827, (1926).

[16] W. Pauli. Über den Zusammenhang des Abschlusses der Elektronengruppen im Atom mit der Komplexstruktur der Spektren. *Zeitschrift für Physik.* **31**(1):765–783, (1925).

[17] S. Van Loon. *Path integral description of excitations in superfluid Fermi gases.* Ph.D. thesis, University of Antwerp, Antwerp, (2020).

[18] M. H. Anderson, J. R. Ensher, M. R. Matthews, C. E. Wieman, & E. A. Cornell. Observation of Bose-Einstein Condensation in a Dilute Atomic Vapor. *Science.* **269**(5221): 198–201, (1995).

[19] K. B. Davis, M. O. Mewes, M. R. Andrews, N. J. Van Druten, D. S. Durfee, D. M. Kurn, & W. Ketterle. Bose-Einstein Condensation in a Gas of Sodium Atoms. *Physical Review Letters.* **75**(22):3969–3973, (1995).

[20] C. Deppner, W. Herr, M. Cornelius, P. Stromberger, T. Sternke, C. Grzeschik, A. Grote, J. Rudolph, S. Herrmann, M. Krutzik, A. Wenzlawski, R. Corgier, E. Charron, D. Guéry-Odelin, N. Gaaloul, C. Lämmerzahl, A. Peters, P. Windpassinger, & E. M. Rasel. Collective-Mode Enhanced Matter-Wave Optics. *Physical Review Letters.* **127**(10):100401, (2021).

[21] J. Tempere. *Bose-Einstein Condensation, Superfluidity and Superconductivity.* Universiteit Antwerpen, (2024).

[22] A. Burchianti, C. D'Errico, L. Marconi, F. Minardi, C. Fort, & M. Modugno. Effect of interactions in the interference pattern of Bose-Einstein condensates. *Physical Review A.* **102**(4):043314, (2020).

[23] R. Onofrio, C. Raman, J. M. Vogels, J. R. Abo-Shaeer, A. P. Chikkatur, & W. Ketterle. Observation of Superfluid Flow in a Bose-Einstein Condensed Gas. *Physical Review Letters.* **85**(11):2228–2231, (2000).

[24] I. Carusotto, S. X. Hu, L. A. Collins, & A. Smerzi. Bogoliubov-Čerenkov Radiation in a Bose-Einstein Condensate Flowing against an Obstacle. *Physical Review Letters.* **97**(26): 260403, (2006).

[25] P. Engels & C. Atherton. Stationary and Nonstationary Fluid Flow of a Bose-Einstein Condensate Through a Penetrable Barrier. *Physical Review Letters.* **99**(16):160405, (2007).

[26] N. Navon, R. P. Smith, & Z. Hadzibabic. Quantum gases in optical boxes. *Nature Physics.* **17**(12):1334–1341, (2021).

[27] D. Jaksch & P. Zoller. The cold atom Hubbard toolbox. *Annals of Physics.* **315**(1):52–79, (2005).

[28] D. Petrov, D. M. Gangardt, & G. V. Shlyapnikov. Low-dimensional trapped gases. *Journal de Physique IV Proceedings.* **116**:5–44, (2004).

[29] N. D. Mermin & H. Wagner. Absence of Ferromagnetism or Antiferromagnetism in One- or Two-Dimensional Isotropic Heisenberg Models. *Physical Review Letters.* **17**(22):1133–1136, (1966).

[30] E. H. Lieb & W. Liniger. Exact Analysis of an Interacting Bose Gas. I. The General

Solution and the Ground State. *Physical Review.* **130**(4):1605–1616, (1963).

[31] E. H. Lieb. Exact Analysis of an Interacting Bose Gas. II. The Excitation Spectrum. *Physical Review.* **130**(4):1616–1624, (1963).

[32] M. Greiner, O. Mandel, T. Esslinger, T. W. Hänsch, & I. Bloch. Quantum phase transition from a superfluid to a Mott insulator in a gas of ultracold atoms. *Nature.* **415**(6867):39–44, (2002).

[33] M. Albiez, R. Gati, J. Fölling, S. Hunsmann, M. Cristiani, & M. K. Oberthaler. Direct Observation of Tunneling and Nonlinear Self-Trapping in a Single Bosonic Josephson Junction. *Physical Review Letters.* **95**(1):010402, (2005).

[34] L. Amico, M. Boshier, G. Birkl, A. Minguzzi, C. Miniatura, L. C. Kwek, D. Aghamalyan, V. Ahufinger, D. Anderson, N. Andrei, A. S. Arnold, M. Baker, T. A. Bell, T. Bland, J. P. Brantut, D. Cassettari, W. J. Chetcuti, F. Chevy, R. Citro, S. De Palo, R. Dumke, M. Edwards, R. Folman, J. Fortagh, S. A. Gardiner, B. M. Garraway, G. Gauthier, A. Günther, T. Haug, C. Hufnagel, M. Keil, P. Ireland, M. Lebrat, W. Li, L. Longchambon, J. Mompart, O. Morsch, P. Naldesi, T. W. Neely, M. Olshanii, E. Orignac, S. Pandey, A. Pérez-Obiol, H. Perrin, L. Piroli, J. Polo, A. L. Pritchard, N. P. Proukakis, C. Rylands, H. Rubinsztein-Dunlop, F. Scazza, S. Stringari, F. Tosto, A. Trombettoni, N. Victorin, W. V. Klitzing, D. Wilkowski, K. Xhani, & A. Yakimenko. Roadmap on Atomtronics: State of the art and perspective. *AVS Quantum Science.* **3**(3):039201, (2021).

[35] L. Amico, D. Anderson, M. Boshier, J. P. Brantut, L. C. Kwek, A. Minguzzi, & W. von Klitzing. Colloquium: Atomtronic circuits: From many-body physics to quantum technologies. *Reviews of Modern Physics.* **94**(4):041001, (2022).

[36] A. Micheli, A. J. Daley, D. Jaksch, & P. Zoller. Single Atom Transistor in a 1D Optical Lattice. *Physical Review Letters.* **93**(14):140408, (2004).

[37] B. T. Seaman, M. Krämer, D. Z. Anderson, & M. J. Holland. Atomtronics: Ultracold-atom analogs of electronic devices. *Physical Review A.* **75**(2):023615, (2007).

[38] J. A. Stickney, D. Z. Anderson, & A. A. Zozulya. Transistorlike behavior of a Bose-Einstein condensate in a triple-well potential. *Physical Review A.* **75**(1):013608, (2007).

[39] R. A. Pepino, J. Cooper, D. Meiser, D. Z. Anderson, & M. J. Holland. Open quantum systems approach to atomtronics. *Physical Review A.* **82**(1):013640, (2010).

[40] C. F. Roos, P. Cren, D. Guéry-Odelin, & J. Dalibard. Continuous loading of a non-dissipative atom trap. *Europhysics Letters.* **61**(2):187–193, (2003).

[41] A. A. Zozulya & D. Z. Anderson. Principles of an atomtronic battery. *Physical Review A.* **88**(4):043641, (2013).

[42] D. Aghamalyan, N. T. Nguyen, F. Auksztol, K. S. Gan, M. M. Valado, P. C. Condylis, L. C. Kwek, R. Dumke, & L. Amico. An atomtronic flux qubit: a ring lattice of Bose–Einstein condensates interrupted by three weak links. *New Journal of Physics.* **18**(7):075013, (2016).

[43] H. Kiehn, V. P. Singh, & L. Mathey. Implementation of an atomtronic SQUID in a strongly confined toroidal condensate. *Physical Review Research.* **4**(3):033024, (2022).

[44] F. Jendrzejewski, S. Eckel, N. Murray, C. Lanier, M. Edwards, C. Lobb, & G. Campbell.

Resistive Flow in a Weakly Interacting Bose-Einstein Condensate. *Physical Review Letters.* **113**(4):045305, (2014).

[45] C. Ryu, E. C. Samson, & M. G. Boshier. Quantum interference of currents in an atomtronic SQUID. *Nature Communications.* **11**(1):3338, (2020).

[46] L. Pezzè, K. Xhani, C. Daix, N. Grani, B. Donelli, F. Scazza, D. Hernandez-Rajkov, W. J. Kwon, G. Del Pace, & G. Roati. Stabilizing persistent currents in an atomtronic Josephson junction necklace. *Nature Communications.* **15**(1):4831, (2024).

[47] R. Labouvie, B. Santra, S. Heun, S. Wimberger, & H. Ott. Negative Differential Conductivity in an Interacting Quantum Gas. *Physical Review Letters.* **115**(5):050601, (2015).

[48] R. Labouvie, B. Santra, S. Heun, & H. Ott. Bistability in a Driven-Dissipative Superfluid. *Physical Review Letters.* **116**(23):235302, (2016).

[49] A. Müllers, B. Santra, C. Baals, J. Jiang, J. Benary, R. Labouvie, D. A. Zezyulin, V. V. Konotop, & H. Ott. Coherent perfect absorption of nonlinear matter waves. *Science Advances.* **4**(8):eaat6539, (2018).

[50] J. Benary, C. Baals, E. Bernhart, J. Jiang, M. Röhrle, & H. Ott. Experimental observation of a dissipative phase transition in a multi-mode many-body quantum system. *New Journal of Physics.* **24**(10):103034, (2022).

[51] M. Röhrle, J. Benary, E. Bernhart, & H. Ott. Dynamic hysteresis across a dissipative multi-mode phase transition. *SciPost Physics.* **16**(6):158, (2024).

[52] G. Barontini, R. Labouvie, F. Stubenrauch, A. Vogler, V. Guarrera, & H. Ott. Controlling the dynamics of an open many-body quantum system with localized dissipation. *Physical Review Letters.* **110**(3):035302, (2013).

[53] M. Reeves & M. Davis. Bistability and nonequilibrium condensation in a driven-dissipative Josephson array: A c-field model. *SciPost Physics.* **15**(2):068, (2023).

[54] D. Fischer & S. Wimberger. Models for a multimode bosonic tunneling junction: Models for a multimode bosonic tunneling junction. *Annalen der Physik.* **529**(7):1600327, (2017).

[55] C. Mink, A. Pelster, J. Benary, H. Ott, & M. Fleischhauer. Variational truncated Wigner approximation for weakly interacting Bose fields: Dynamics of coupled condensates. *SciPost Physics.* **12**(2):051, (2022).

[56] S. E. Begg, M. J. Davis, & M. T. Reeves. Nonequilibrium Transport in a Superfluid Josephson Junction Chain: Is There Negative Differential Conductivity?. *Physical Review Letters.* **132**(10):103402, (2024).

[57] S. Diehl, A. Micheli, A. Kantian, B. Kraus, H. P. Büchler, & P. Zoller. Quantum states and phases in driven open quantum systems with cold atoms. *Nature Physics.* **4**(11):878–883, (2008).

[58] F. Verstraete, M. M. Wolf, & J. Ignacio Cirac. Quantum computation and quantum-state engineering driven by dissipation. *Nature Physics.* **5**(9):633–636, (2009).

[59] J. T. Barreiro, M. Müller, P. Schindler, D. Nigg, T. Monz, M. Chwalla, M. Hennrich, C. F. Roos, P. Zoller, & R. Blatt. An open-system quantum simulator with trapped ions. *Nature.* **470**(7335):486–491, (2011).

[60] D. Sels & E. Demler. Thermal radiation and dissipative phase transition in a BEC with local loss. *Annals of Physics.* **412**:168021, (2020).

[61] P. D. Drummond & D. F. Walls. Quantum theory of optical bistability. I. Nonlinear polarisability model. *Journal of Physics A: Mathematical and General.* **13**(2):725–741, (1980).

[62] M. Wouters & I. Carusotto. Excitations in a Nonequilibrium Bose-Einstein Condensate of Exciton Polaritons. *Physical Review Letters.* **99**(14):140402, (2007).

[63] E. M. Kessler, G. Giedke, A. Imamoglu, S. F. Yelin, M. D. Lukin, & J. I. Cirac. Dissipative phase transition in a central spin system. *Physical Review A.* **86**(1):012116, (2012).

[64] G. Kordas, S. Wimberger, & D. Witthaut. Dissipation-induced macroscopic entanglement in an open optical lattice. *Europhysics Letters.* **100**(3):30007, (2012).

[65] Z. Wang, C. Navarrete-Benlloch, & Z. Cai. Pattern Formation and Exotic Order in Driven-Dissipative Bose-Hubbard Systems. *Physical Review Letters.* **125**(11):115301, (2020).

[66] H. P. Breuer & F. Petruccione. *The theory of open quantum systems.* Clarendon Press, Oxford, (2009). ISBN 978-0-19-852063-4 978-0-19-921390-0.

[67] C. Gardiner & P. Zoller. *Quantum Noise: A Handbook of Markovian and Non-Markovian Quantum Stochastic Methods with Applications to Quantum Optics.* Springer, Berlin Heidelberg, (2004). ISBN 978-3-540-22301-6.

[68] A. Rivas & S. F. Huelga. *Open Quantum Systems: An Introduction.* Springer, Berlin, Heidelberg, (2011). ISBN 978-3-642-23353-1.

[69] F. Minganti, A. Biella, N. Bartolo, & C. Ciuti. Spectral theory of Liouvillians for dissipative phase transitions. *Physical Review A.* **98**(4):042118, (2018).

[70] F. Minganti & D. Huybrechts. Arnoldi-Lindblad time evolution: Faster-than-the-clock algorithm for the spectrum of time-independent and Floquet open quantum systems. *Quantum.* **6**:649, (2022).

[71] L. Landau & E. Lifshitz. *Statistical Physics*, volume 5. Pergamon Press, Oxford, 2nd edition, (1969).

[72] S. Sachdev. *Quantum Phase Transitions.* Cambridge University Press, New York, 2nd edition, (2011).

[73] K. Macieszczak, M. Guţă, I. Lesanovsky, & J. P. Garrahan. Towards a Theory of Metastability in Open Quantum Dynamics. *Physical Review Letters.* **116**(24):240404, (2016).

[74] H. Spohn. Approach to equilibrium for completely positive dynamical semigroups of N-level systems. *Reports on Mathematical Physics.* **10**(2):189–194, (1976).

[75] V. V. Albert & L. Jiang. Symmetries and conserved quantities in Lindblad master equations. *Physical Review A.* **89**(2):022118, (2014).

[76] D. Nigro. On the uniqueness of the steady-state solution of the Lindblad–Gorini–Kossakowski–Sudarshan equation. *Journal of Statistical Mechanics: Theory and Experiment.* **2019**(4):043202, (2019).

[77] L. De Sarlo, L. Fallani, J. E. Lye, M. Modugno, R. Saers, C. Fort, & M. Inguscio. Unstable

regimes for a Bose-Einstein condensate in an optical lattice. *Physical Review A.* **72**(1): 013603, (2005).

[78] M. O. Scully & M. S. Zubairy. *Quantum Optics.* Cambridge University Press, Cambridge, 1st ed edition, (1997).

[79] D. F. Walls & G. J. Milburn. *Quantum optics.* Springer, Berlin, 2nd edition, (2008). ISBN 978-3-540-28573-1.

[80] M. J. Steel, M. K. Olsen, L. I. Plimak, P. D. Drummond, S. M. Tan, M. J. Collett, D. F. Walls, & R. Graham. Dynamical quantum noise in trapped Bose-Einstein condensates. *Physical Review A.* **58**(6):4824–4835, (1998).

[81] P. B. Blakie, A. S. Bradley, M. J. Davis, R. J. Ballagh, & C. W. Gardiner. Dynamics and statistical mechanics of ultra-cold Bose gases using c-field techniques. *Advances in Physics.* **57**(5):363–455, (2008).

[82] D. Witthaut, F. Trimborn, H. Hennig, G. Kordas, T. Geisel, & S. Wimberger. Beyond mean-field dynamics in open Bose-Hubbard chains. *Physical Review A.* **83**(6):063608, (2011).

[83] E. Wigner. On the Quantum Correction For Thermodynamic Equilibrium. *Physical Review.* **40**(5):749–759, (1932).

[84] K. V. Kheruntsyan. Wigner function for a driven anharmonic oscillator. *Journal of Optics B: Quantum and Semiclassical Optics.* **1**(2):225–233, (1999).

[85] C. W. Gardiner. *Handbook of Stochastic Methods: for Physics, Chemistry and the Natural Sciences.* Springer, Berlin Heidelberg, 3rd edition, (2004). ISBN 978-3-540-20882-2.

[86] M. J. Davis, S. A. Morgan, & K. Burnett. Simulations of Bose Fields at Finite Temperature. *Physical Review Letters.* **87**(16):160402, (2001).

[87] M. J. Davis, R. J. Ballagh, & K. Burnett. Dynamics of thermal Bose fields in the classical limit. *Journal of Physics B: Atomic, Molecular and Optical Physics.* **34**(22):4487–4512, (2001).

[88] M. J. Davis, S. A. Morgan, & K. Burnett. Simulations of thermal Bose fields in the classical limit. *Physical Review A.* **66**(5):053618, (2002).

[89] P. B. Blakie & M. J. Davis. Projected Gross-Pitaevskii equation for harmonically confined Bose gases at finite temperature. *Physical Review A.* **72**(6):063608, (2005).

[90] N. Proukakis, S. Gardiner, M. Davis, & M. Szymańska. *Quantum Gases: Finite Temperature and Non-Equilibrium Dynamics*, volume 1 of *Cold Atoms.* Imperial College Press, (2013). ISBN 978-1-84816-810-7 978-1-84816-812-1.

[91] B. Opanchuk & P. D. Drummond. Functional Wigner representation of quantum dynamics of Bose-Einstein condensate. *Journal of Mathematical Physics.* **54**(4):042107, (2013).

[92] A. S. Bradley, P. B. Blakie, & C. W. Gardiner. Properties of the stochastic Gross-Pitaevskii equation: Projected Ehrenfest relations and the optimal plane wave basis. *Journal of Physics B: Atomic, Molecular and Optical Physics.* **38**(23):4259–4280, (2005).

[93] C. M. Dion & E. Cancès. Spectral method for the time-dependent Gross-Pitaevskii equation

with a harmonic trap. *Physical Review E.* **67**(4):046706, (2003).

[94] N. Bartolo, F. Minganti, W. Casteels, & C. Ciuti. Exact steady state of a Kerr resonator with one- and two-photon driving and dissipation: Controllable Wigner-function multimodality and dissipative phase transitions. *Physical Review A.* **94**(3):033841, (2016).

[95] B. Buča, C. Booker, M. Medenjak, & D. Jaksch. Bethe ansatz approach for dissipation: exact solutions of quantum many-body dynamics under loss. *New Journal of Physics.* **22** (12):123040, (2020).

[96] M. Nakagawa, N. Kawakami, & M. Ueda. Exact Liouvillian Spectrum of a One-Dimensional Dissipative Hubbard Model. *Physical Review Letters.* **126**(11):110404, (2021).

[97] P. Kattel, P. R. Pasnoori, & N. Andrei. Exact solution of a non-Hermitian PT -symmetric spin chain. *Journal of Physics A: Mathematical and Theoretical.* **56**(32):325001, (2023).

[98] S. Sayyad & J. L. Lado. Topological phase diagrams of exactly solvable non-Hermitian interacting Kitaev chains. *Physical Review Research.* **5**(2):L022046, (2023).

[99] T. Botzung & P. Nataf. Exact Diagonalization of SU (N) Fermi-Hubbard Models. *Physical Review Letters.* **132**(15):153001, (2024).

[100] J. Dalibard, Y. Castin, & K. Mølmer. Wave-function approach to dissipative processes in quantum optics. *Physical Review Letters.* **68**(5):580–583, (1992).

[101] M. B. Plenio & P. L. Knight. The quantum-jump approach to dissipative dynamics in quantum optics. *Reviews of Modern Physics.* **70**(1):101–144, (1998).

[102] A. J. Daley. Quantum trajectories and open many-body quantum systems. *Advances in Physics.* **63**(2):77–149, (2014).

[103] A. Giraldo, S. J. Masson, N. G. R. Broderick, & B. Krauskopf. Semiclassical bifurcations and quantum trajectories: a case study of the open Bose–Hubbard dimer. *The European Physical Journal Special Topics.* **231**(3):385–401, (2022).

[104] H. Weimer. Variational Principle for Steady States of Dissipative Quantum Many-Body Systems. *Physical Review Letters.* **114**(4):040402, (2015).

[105] H. Weimer, A. Kshetrimayum, & R. Orús. Simulation methods for open quantum many-body systems. *Reviews of Modern Physics.* **93**(1):015008, (2021).

[106] L. Gravina & V. Savona. Adaptive variational low-rank dynamics for open quantum systems. *Physical Review Research.* **6**(2):023072, (2024).

[107] W. Verstraelen & M. Wouters. Gaussian Quantum Trajectories for the Variational Simulation of Open Quantum-Optical Systems. *Applied Sciences.* **8**(9):1427, (2018).

[108] D. Huybrechts & M. Wouters. Dynamical hysteresis properties of the driven-dissipative Bose-Hubbard model with a Gutzwiller Monte Carlo approach. *Physical Review A.* **102** (5):053706, (2020).

[109] L. Fernandes, M. Wouters, & J. Tempere. Gaussian trajectory description of fragmentation in an isolated spinor condensate. *Physical Review A.* **105**(1):013305, (2022).

[110] T. E. Lee, S. Gopalakrishnan, & M. D. Lukin. Unconventional Magnetism via Optical Pumping of Interacting Spin Systems. *Physical Review Letters.* **110**(25):257204, (2013).

[111] D. Paz & M. Maghrebi. Time-reversal symmetry breaking and emergence in driven-dissipative Ising models. *SciPost Physics.* **12**(2):066, (2022).

[112] W. Verstraelen, D. Huybrechts, T. Roscilde, & M. Wouters. Quantum and Classical Correlations in Open Quantum Spin Lattices via Truncated-Cumulant Trajectories. *PRX Quantum.* **4**(3):030304, (2023).

[113] H. Carmichael. Breakdown of Photon Blockade: A Dissipative Quantum Phase Transition in Zero Dimensions. *Physical Review X.* **5**(3):031028, (2015).

[114] W. Casteels & C. Ciuti. Quantum entanglement in the spatial-symmetry-breaking phase transition of a driven-dissipative Bose-Hubbard dimer. *Physical Review A.* **95**(1):013812, (2017).

[115] W. Casteels, R. Fazio, & C. Ciuti. Critical dynamical properties of a first-order dissipative phase transition. *Physical Review A.* **95**(1):012128, (2017).

[116] L. M. Sieberer, S. D. Huber, E. Altman, & S. Diehl. Dynamical Critical Phenomena in Driven-Dissipative Systems. *Physical Review Letters.* **110**(19):195301, (2013).

[117] R. Sett, F. Hassani, D. Phan, S. Barzanjeh, A. Vukics, & J. M. Fink. Emergent Macroscopic Bistability Induced by a Single Superconducting Qubit. *PRX Quantum.* **5**(1): 010327, (2024).

[118] H. Gibbs. *Optical Bistability: Controlling Light With Light.* Academic Press Inc, 1st edition, (2012). ISBN 978-0-12-281940-7.

[119] I. Carusotto & C. Ciuti. Quantum fluids of light. *Reviews of Modern Physics.* **85**(1): 299–366, (2013).

[120] S. Rodriguez, W. Casteels, F. Storme, N. Carlon Zambon, I. Sagnes, L. Le Gratiet, E. Galopin, A. Lemaître, A. Amo, C. Ciuti, & J. Bloch. Probing a Dissipative Phase Transition via Dynamical Optical Hysteresis. *Physical Review Letters.* **118**(24):247402, (2017).

[121] T. Fink, A. Schade, S. Höfling, C. Schneider, & A. Imamoglu. Signatures of a dissipative phase transition in photon correlation measurements. *Nature Physics.* **14**(4):365–369, (2018).

[122] I. Siddiqi, R. Vijay, F. Pierre, C. M. Wilson, M. Metcalfe, C. Rigetti, L. Frunzio, & M. H. Devoret. RF-Driven Josephson Bifurcation Amplifier for Quantum Measurement. *Physical Review Letters.* **93**(20):207002, (2004).

[123] F. R. Ong, M. Boissonneault, F. Mallet, A. Palacios-Laloy, A. Dewes, A. C. Doherty, A. Blais, P. Bertet, D. Vion, & D. Esteve. Circuit QED with a Nonlinear Resonator: ac-Stark Shift and Dephasing. *Physical Review Letters.* **106**(16):167002, (2011).

[124] M. Foss-Feig, P. Niroula, J. T. Young, M. Hafezi, A. V. Gorshkov, R. M. Wilson, & M. F. Maghrebi. Emergent equilibrium in many-body optical bistability. *Physical Review A.* **95** (4):043826, (2017).

[125] K. G. Lagoudakis, B. Pietka, M. Wouters, R. André, & B. Deveaud-Plédran. Coherent Oscillations in an Exciton-Polariton Josephson Junction. *Physical Review Letters.* **105** (12):120403, (2010).

[126] M. Galbiati, L. Ferrier, D. D. Solnyshkov, D. Tanese, E. Wertz, A. Amo, M. Abbarchi,

P. Senellart, I. Sagnes, A. Lemaître, E. Galopin, G. Malpuech, & J. Bloch. Polariton Condensation in Photonic Molecules. *Physical Review Letters.* **108**(12):126403, (2012).

[127] M. Abbarchi, A. Amo, V. G. Sala, D. D. Solnyshkov, H. Flayac, L. Ferrier, I. Sagnes, E. Galopin, A. Lemaître, G. Malpuech, & J. Bloch. Macroscopic quantum self-trapping and Josephson oscillations of exciton polaritons. *Nature Physics.* **9**(5):275–279, (2013).

[128] S. R. K. Rodriguez, A. Amo, I. Sagnes, L. Le Gratiet, E. Galopin, A. Lemaître, & J. Bloch. Interaction-induced hopping phase in driven-dissipative coupled photonic microcavities. *Nature Communications.* **7**(1):11887, (2016).

[129] N. Carlon Zambon, S. R. K. Rodriguez, A. Lemaître, A. Harouri, L. Le Gratiet, I. Sagnes, P. St-Jean, S. Ravets, A. Amo, & J. Bloch. Parametric instability in coupled nonlinear microcavities. *Physical Review A.* **102**(2):023526, (2020).

[130] M. Fitzpatrick, N. M. Sundaresan, A. C. Li, J. Koch, & A. A. Houck. Observation of a Dissipative Phase Transition in a One-Dimensional Circuit QED Lattice. *Physical Review X.* **7**(1):011016, (2017).

[131] A. A. Houck, H. E. Türeci, & J. Koch. On-chip quantum simulation with superconducting circuits. *Nature Physics.* **8**(4):292–299, (2012).

[132] C. Eichler, Y. Salathe, J. Mlynek, S. Schmidt, & A. Wallraff. Quantum-Limited Amplification and Entanglement in Coupled Nonlinear Resonators. *Physical Review Letters.* **113**(11):110502, (2014).

[133] P. Hamel, S. Haddadi, F. Raineri, P. Monnier, G. Beaudoin, I. Sagnes, A. Levenson, & A. M. Yacomotti. Spontaneous mirror-symmetry breaking in coupled photonic-crystal nanolasers. *Nature Photonics.* **9**(5):311–315, (2015).

[134] B. Garbin, A. Giraldo, K. J. H. Peters, N. Broderick, A. Spakman, F. Raineri, A. Levenson, S. R. K. Rodriguez, B. Krauskopf, & A. M. Yacomotti. Spontaneous Symmetry Breaking in a Coherently Driven Nanophotonic Bose-Hubbard Dimer. *Physical Review Letters.* **128**(5):053901, (2022).

[135] W. Casteels, F. Storme, A. Le Boité, & C. Ciuti. Power laws in the dynamic hysteresis of quantum nonlinear photonic resonators. *Physical Review A.* **93**(3):033824, (2016).

[136] A. Le Boité, G. Orso, & C. Ciuti. Steady-State Phases and Tunneling-Induced Instabilities in the Driven Dissipative Bose-Hubbard Model. *Physical Review Letters.* **110**(23):233601, (2013).

[137] S. Finazzi, A. Le Boité, F. Storme, A. Baksic, & C. Ciuti. Corner-Space Renormalization Method for Driven-Dissipative Two-Dimensional Correlated Systems. *Physical Review Letters.* **115**(8):080604, (2015).

[138] M. Biondi, G. Blatter, H. E. Türeci, & S. Schmidt. Nonequilibrium gas-liquid transition in the driven-dissipative photonic lattice. *Physical Review A.* **96**(4):043809, (2017).

[139] F. Vicentini, F. Minganti, R. Rota, G. Orso, & C. Ciuti. Critical slowing down in driven-dissipative Bose-Hubbard lattices. *Physical Review A.* **97**(1):013853, (2018).

[140] D. Roberts & A. A. Clerk. Competition between Two-Photon Driving, Dissipation, and Interactions in Bosonic Lattice Models: An Exact Solution. *Physical Review Letters.* **130**

(6):063601, (2023).

[141] R. Ceulemans & M. Wouters. Nonequilibrium steady states and critical slowing down in the dissipative Bose-Hubbard model. *Physical Review A*. **108**(1):013314, (2023).

[142] G. Kordas, D. Witthaut, & S. Wimberger. Non-equilibrium dynamics in dissipative Bose-Hubbard chains: Non-equilibrium dynamics in dissipative Bose-Hubbard chains. *Annalen der Physik*. **527**(9-10):619–628, (2015).

[143] P. Barmettler & C. Kollath. Controllable manipulation and detection of local densities and bipartite entanglement in a quantum gas by a dissipative defect. *Physical Review A*. **84**(4):041606, (2011).

[144] M. Kiefer-Emmanouilidis & J. Sirker. Current reversals and metastable states in the infinite Bose-Hubbard chain with local particle loss. *Physical Review A*. **96**(6):063625, (2017).

[145] A. Smerzi, S. Fantoni, S. Giovanazzi, & S. R. Shenoy. Quantum Coherent Atomic Tunneling between Two Trapped Bose-Einstein Condensates. *Physical Review Letters*. **79**(25):4950–4953, (1997).

[146] F. Meier & W. Zwerger. Josephson tunneling between weakly interacting Bose-Einstein condensates. *Physical Review A*. **64**(3):033610, (2001).

[147] M. Seclì, M. Capone, & M. Schirò. Signatures of self-trapping in the driven-dissipative Bose–Hubbard dimer. *New Journal of Physics*. **23**(6):063056, (2021).

[148] V. Makhankov. Dynamics of classical solitons (in non-integrable systems). *Physics Reports*. **35**(1):1–128, (1978).

[149] B. Denardo, W. Wright, S. Putterman, & A. Larraza. Observation of a kink soliton on the surface of a liquid. *Physical Review Letters*. **64**(13):1518–1521, (1990).

[150] Y. S. Kivshar. Nonlinear dynamics near the zero-dispersion point in optical fibers. *Physical Review A*. **43**(3):1677–1679, (1991).

[151] S. Burtsev & R. Camassa. Nonadiabatic dynamics of dark solitons. *Journal of the Optical Society of America B*. **14**(7):1782, (1997).

[152] T. Dauxois & M. Peyrard. *Physics of solitons*. Cambridge University Press, Cambridge, UK ; New York, (2006). ISBN 978-0-521-85421-4.

[153] R. Heidemann, S. Zhdanov, R. Sütterlin, H. M. Thomas, & G. E. Morfill. Dissipative Dark Soliton in a Complex Plasma. *Physical Review Letters*. **102**(13):135002, (2009).

[154] Y. V. Kartashov, B. A. Malomed, & L. Torner. Solitons in nonlinear lattices. *Reviews of Modern Physics*. **83**(1):247–305, (2011).

[155] S. Burger, K. Bongs, S. Dettmer, W. Ertmer, K. Sengstock, A. Sanpera, G. V. Shlyapnikov, & M. Lewenstein. Dark Solitons in Bose-Einstein Condensates. *Physical Review Letters*. **83**(25):5198–5201, (1999).

[156] J. Denschlag, J. E. Simsarian, D. L. Feder, C. W. Clark, L. A. Collins, J. Cubizolles, L. Deng, E. W. Hagley, K. Helmerson, W. P. Reinhardt, S. L. Rolston, B. I. Schneider, & W. D. Phillips. Generating Solitons by Phase Engineering of a Bose-Einstein Condensate. *Science*. **287**(5450):97–101, (2000).

[157] C. Becker, S. Stellmer, P. Soltan-Panahi, S. Dörscher, M. Baumert, E. M. Richter, J. Kronjäger, K. Bongs, & K. Sengstock. Oscillations and interactions of dark and dark–bright solitons in Bose–Einstein condensates. *Nature Physics.* **4**(6):496–501, (2008).

[158] S. Stellmer, C. Becker, P. Soltan-Panahi, E. M. Richter, S. Dörscher, M. Baumert, J. Kronjäger, K. Bongs, & K. Sengstock. Collisions of Dark Solitons in Elongated Bose-Einstein Condensates. *Physical Review Letters.* **101**(12):120406, (2008).

[159] C. J. Myatt, E. A. Burt, R. W. Ghrist, E. A. Cornell, & C. E. Wieman. Production of Two Overlapping Bose-Einstein Condensates by Sympathetic Cooling. *Physical Review Letters.* **78**(4), (1997).

[160] D. S. Hall, M. R. Matthews, J. R. Ensher, C. E. Wieman, & E. A. Cornell. Dynamics of Component Separation in a Binary Mixture of Bose-Einstein Condensates. *Physical Review Letters.* **81**(8), (1998).

[161] G. Modugno, M. Modugno, F. Riboli, G. Roati, & M. Inguscio. Two Atomic Species Superfluid. *Physical Review Letters.* **89**(19):190404, (2002).

[162] G. Thalhammer, G. Barontini, L. De Sarlo, J. Catani, F. Minardi, & M. Inguscio. Double Species Bose-Einstein Condensate with Tunable Interspecies Interactions. *Physical Review Letters.* **100**(21):210402, (2008).

[163] M. Abad & A. Recati. A study of coherently coupled two-component Bose-Einstein condensates. *The European Physical Journal D.* **67**(7):148, (2013).

[164] T. K. Paraïso, M. Wouters, Y. Léger, F. Morier-Genoud, & B. Deveaud-Plédran. Multistability of a coherent spin ensemble in a semiconductor microcavity. *Nature Materials.* **9**(8): 655–660, (2010).

[165] L. M. Duan, E. Demler, & M. D. Lukin. Controlling Spin Exchange Interactions of Ultracold Atoms in Optical Lattices. *Physical Review Letters.* **91**(9):090402, (2003).

[166] O. Mandel, M. Greiner, A. Widera, T. Rom, T. W. Hänsch, & I. Bloch. Coherent Transport of Neutral Atoms in Spin-Dependent Optical Lattice Potentials. *Physical Review Letters.* **91**(1):010407, (2003).

[167] T. Gericke, P. Würtz, D. Reitz, T. Langen, & H. Ott. High-resolution scanning electron microscopy of an ultracold quantum gas. *Nature Physics.* **4**(12):949–953, (2008).

[168] J. Kasprzak, M. Richard, S. Kundermann, A. Baas, P. Jeambrun, J. M. J. Keeling, F. M. Marchetti, M. H. Szymańska, R. André, J. L. Staehli, V. Savona, P. B. Littlewood, B. Deveaud, & L. S. Dang. Bose–Einstein condensation of exciton polaritons. *Nature.* **443** (7110):409–414, (2006).

[169] R. Balili, V. Hartwell, D. Snoke, L. Pfeiffer, & K. West. Bose-Einstein Condensation of Microcavity Polaritons in a Trap. *Science.* **316**(5827):1007–1010, (2007).

[170] H. Alnatah, Q. Yao, J. Beaumariage, S. Mukherjee, M. C. Tam, Z. Wasilewski, K. West, K. Baldwin, L. N. Pfeiffer, & D. W. Snoke. Coherence measurements of polaritons in thermal equilibrium reveal a power law for two-dimensional condensates. *Science Advances.* **10** (18):eadk6960, (2024).

[171] A. Baas, J. P. Karr, H. Eleuch, & E. Giacobino. Optical bistability in semiconductor

microcavities. *Physical Review A.* **69**(2):023809, (2004).

[172] A. Amo, J. Lefrère, S. Pigeon, C. Adrados, C. Ciuti, I. Carusotto, R. Houdré, E. Giacobino, & A. Bramati. Superfluidity of polaritons in semiconductor microcavities. *Nature Physics.* **5**(11):805–810, (2009).

[173] J. Bloch, I. Carusotto, & M. Wouters. Non-equilibrium Bose–Einstein condensation in photonic systems. *Nature Reviews Physics.* **4**(7):470–488, (2022).

[174] A. Sinatra, C. Lobo, & Y. Castin. The truncated Wigner method for Bose condensed gases: limits of validity and applications. *Journal of Physics B: Atomic, Molecular and Optical Physics.* **35**(17):3599–3631, (2002).

[175] P. Deuar, A. Ferrier, M. Matuszewski, G. Orso, & M. H. Szymańska. Fully Quantum Scalable Description of Driven-Dissipative Lattice Models. *PRX Quantum.* **2**(1):010319, (2021).

[176] P. C. Hohenberg. Existence of Long-Range Order in One and Two Dimensions. *Physical Review.* **158**(2):383–386, (1967).

[177] Z. Hadzibabic, P. Krüger, M. Cheneau, B. Battelier, & J. Dalibard. Berezinskii–Kosterlitz–Thouless crossover in a trapped atomic gas. *Nature.* **441**(7097):1118–1121, (2006).

[178] G. Dagvadorj, J. Fellows, S. Matyjaśkiewicz, F. Marchetti, I. Carusotto, & M. Szymańska. Nonequilibrium Phase Transition in a Two-Dimensional Driven Open Quantum System. *Physical Review X.* **5**(4):041028, (2015).

[179] O. Penrose & L. Onsager. Bose-Einstein Condensation and Liquid Helium. *Physical Review.* **104**(3):576–584, (1956).

[180] A. M. Kamchatnov. Expansion of Bose-Einstein condensates confined in quasi-one-dimensional or quasi-two-dimensional traps. *Journal of Experimental and Theoretical Physics.* **98**(5):908–917, (2004).

[181] J. Akram & A. Pelster. Sculpting quasi-one-dimensional Bose-Einstein condensate to generate calibrated matter waves. *Physical Review A.* **93**(2):023606, (2016).

[182] T. Tsuzuki. Nonlinear waves in the Pitaevskii-Gross equation. *Journal of Low Temperature Physics.* **4**(4):441–457, (1971).

[183] A. Negretti, C. Henkel, & K. Mølmer. Quantum fluctuations in the image of a Bose gas. *Physical Review A.* **78**(2):023630, (2008).

[184] T. Busch & J. R. Anglin. Motion of Dark Solitons in Trapped Bose-Einstein Condensates. *Physical Review Letters.* **84**(11):2298–2301, (2000).

[185] B. P. Anderson, P. C. Haljan, C. A. Regal, D. L. Feder, L. A. Collins, C. W. Clark, & E. A. Cornell. Watching Dark Solitons Decay into Vortex Rings in a Bose-Einstein Condensate. *Physical Review Letters.* **86**(14):2926–2929, (2001).

[186] Z. Dutton, M. Budde, C. Slowe, & L. V. Hau. Observation of Quantum Shock Waves Created with Ultra- Compressed Slow Light Pulses in a Bose-Einstein Condensate. *Science.* **293**(5530):663–668, (2001).

[187] A. Weller, J. P. Ronzheimer, C. Gross, J. Esteve, M. K. Oberthaler, D. J. Frantzeskakis, G. Theocharis, & P. G. Kevrekidis. Experimental Observation of Oscillating and Interacting Matter Wave Dark Solitons. *Physical Review Letters.* **101**(13):130401, (2008).

[188] J. Dziarmaga. Quantum dark soliton: Nonperturbative diffusion of phase and position. *Physical Review A.* **70**(6):063616, (2004).

[189] Y. S. Kivshar, W. Królikowski, & O. A. Chubykalo. Dark solitons in discrete lattices. *Physical Review E.* **50**(6):5020–5032, (1994).

[190] U. Al Khawaja, S. Al-Marzoug, & H. Bahlouli. Peierls–Nabarro potential profile of discrete nonlinear Schrödinger equation. *Communications in Nonlinear Science and Numerical Simulation.* **46**:74–80, (2017).

[191] M. Johansson & Y. S. Kivshar. Discreteness-Induced Oscillatory Instabilities of Dark Solitons. *Physical Review Letters.* **82**(1):85–88, (1999).

[192] D. M. Gangardt & A. Kamenev. Quantum Decay of Dark Solitons. *Physical Review Letters.* **104**(19):190402, (2010).

[193] Y. Ozaki, K. Nagao, I. Danshita, & K. Kasamatsu. Semiclassical dynamics of a dark soliton in a one-dimensional bosonic superfluid in an optical lattice. *Physical Review Research.* **2** (3):033272, (2020).

[194] D. A. Zezyulin, V. V. Konotop, G. Barontini, & H. Ott. Macroscopic Zeno Effect and Stationary Flows in Nonlinear Waveguides with Localized Dissipation. *Physical Review Letters.* **109**(2):020405, (2012).

[195] A. E. Muryshev, H. B. Van Linden Van Den Heuvell, & G. V. Shlyapnikov. Stability of standing matter waves in a trap. *Physical Review A.* **60**(4):R2665–R2668, (1999).

[196] J. Brand & W. P. Reinhardt. Solitonic vortices and the fundamental modes of the "snake instability": Possibility of observation in the gaseous Bose-Einstein condensate. *Physical Review A.* **65**(4):043612, (2002).

[197] C. Baals, A. G. Moreno, J. Jiang, J. Benary, & H. Ott. Stability analysis and attractor dynamics of three-dimensional dark solitons with localized dissipation. *Physical Review A.* **103**(4):043304, (2021).

[198] W. Van Alphen, H. Takeuchi, & J. Tempere. Crossover between snake instability and Josephson instability of dark solitons in superfluid Fermi gases. *Physical Review A.* **100** (2):023628, (2019).

[199] A. Gaidoukov & J. R. Anglin. Bogoliubov–de Gennes theory of the snake instability of gray solitons in higher dimensions. *Physical Review A.* **103**(1):013319, (2021).

[200] A. H. Stroud & D. Secrest. *Gaussian quadrature formulas.* Englewood Cliffs, N.J., Prentice-Hall, (1966).

[201] J. Bezanson, A. Edelman, S. Karpinski, & V. B. Shah. Julia: A Fresh Approach to Numerical Computing. *SIAM Review.* **59**(1):65–98, (2017).

[202] C. Rackauckas & Q. Nie. DifferentialEquations.jl – A Performant and Feature-Rich Ecosystem for Solving Differential Equations in Julia. *Journal of Open Research Software.* **5** (1):15, (2017).